



Title	Colloidal Synthesis of Coherent InP/ZnS Core/Shell Nanocrystals for Optoelectronic Applications
Author(s)	根本, 一宏
Citation	北海道大学. 博士(理学) 甲第15236号
Issue Date	2022-12-26
DOI	10.14943/doctoral.k15236
Doc URL	http://hdl.handle.net/2115/91024
Type	theses (doctoral)
File Information	NEMOTO_Kazuhiro.pdf



[Instructions for use](#)

**Colloidal Synthesis of Coherent InP/ZnS Core/Shell
Nanocrystals for Optoelectronic Applications**

オプトエレクトロニクス素子創製へ向けた
格子整合性 InP/ZnS コア・シェルナノ粒子の湿式合成

Kazuhiro Nemoto

根本 一宏

Graduate School of Chemical Sciences and Engineering

Hokkaido University

2022

Content

Chapter 1: Introduction	8
1.1 Preface	8
1.2 Colloidal Quantum Dots Overview	8
1.3 Quantum size effect	9
1.3.1 Exciton confinement (weak confinement) of $r_B < R$	11
1.3.2 Individual electron and hole confinement (strong confinement) of $r_B > R$	12
1.4 Synthesis theory of QD	13
1.3.1 Hot injection method	18
1.3.2 Heat up method	23
1.4 Application to optoelectronics	25
1.5 Display using QLED.....	26
1.6 Photodetector	28
1.6.1 Photoconductors	29
1.6.2 Photodiodes	30
1.6.3 Phototransistor.....	30
1.7 Solar cell.....	31
1.8 Toxicity of QD.....	31
1.9 Alternative material candidates.....	32
1.10 InP QD	33
1.11 Improved optical properties with core/shell structure	35
1.12 Relation between the relative positions of the electron energy levels in the semiconductor bandgap of each core and shell	36
1.12.1 Type I structure.....	36
1.12.2 Type II structure	36
1.12.3 Reverse type I structure.....	37
1.13 Lattice matching between core and shell	38
1.14 Coherent core shell structure	39
1.15 Research motivation.....	41

<i>Reference</i>	43
Chapter 2: Coherent InP/ZnS core / shell quantum dots with narrow-band green emissions	54
2.1 <i>Introduction</i>	54
2.2 <i>Experimental</i>	58
2.3 <i>Results and discussion</i>	62
2.4 <i>Conclusions</i>	83
<i>References</i>	84
Chapter 3: Low-Temperature PL Measurements of Coherent InP/ZnS Core-Shell QDs	90
3.1 <i>Introduction</i>	90
3.2 <i>Experimental</i>	90
3.3 <i>Results and discussion</i>	91
3.4 <i>Conclusions</i>	95
<i>References</i>	96
Chapter 4: Impact of Coherent Core/Shell Architecture on Fast Response in InP-based Quantum Dot Photodiodes	98
4.1 <i>Introduction</i>	98
4.2 <i>Experimental</i>	100
4.3 <i>Results and discussion</i>	105
4.4 <i>Conclusions</i>	120
<i>References</i>	121
Chapter 5: Summary and Future Prospects	126
<i>Summary</i>	126
<i>Future Prospects</i>	128

Abstract

Colloidal quantum dots (Colloidal Quantum Dot, QD) refer to 1 ~ 10 nm semiconductor nanoparticles synthesized in the liquid phase. Since the size of the band gap can be controlled by the size of the particle based on the quantum confinement effect manifested in the QD, the light emission and the optical absorption spectrum can be modulated in a wide band. Furthermore, since the organic ligand is soluble in the solution when it is bound to the QD surface, there is an advantage that the device can be produced inexpensively by the coating method. Therefore, research and development toward the creation of optoelectronic devices such as solar cells, phototransistors, photodiodes (PD), lasers, and light emitting diodes using QDs as an active layer is actively being conducted.

In general, surface defect density increases with nanoparticulation. Since defects act as non-radiative deactivation channels and reduce the optical properties of QDs, the development of methods to suppress defect generation is key. The most established method at present is the core/shell method. According to the methodology, a Type-I structure with band energy alignment in which the band end of the shell encompasses the band end of the core increases the rate of radiative recombination of photoexcited carriers, resulting in superior optical properties. In the conventional Type-I structure fabrication, it is important to select the material that constitutes the shell. In the InP studied in this paper, a ZnSe/ZnS double shell structure fulfills the requirement. Concretely, since the lattice matching is not obtained at the interface between the core and the shell due to the difference in the lattice constant between the ZnS and InP, ZnSe having an intermediate value between the lattice constants of InP and ZnS is interpolated. In the core/shell/shell structure in which ZnSe is assembled by shouldering the inner shell, lattice mismatch generated at the interfaces of InP and ZnSe and ZnSe and ZnS is relaxed by strain, and defect generation is suppressed. From the viewpoint

of matching the lattice constants between the core and the shell, it is common practice to alloy the core and/or the shell, but the spectral performance is inferior to the former.

The purpose of this paper is to discuss the synthesis method, structural analysis, optical properties, and the mechanism by which these properties appear for QDs with a coherent core/shell structure, which has been successfully synthesized for the first time in InP systems, and to describe the effect of this structure on device performance through the fabrication and device evaluation of photovoltaic photodiodes equipped with a coherent core/shell QD in the active layer.

In Chapter 1, fundamental physical properties and synthesis methods of compound semiconductor QDs were described. In particular, as for the InP QD developed in this study, recent research examples are introduced, and the process leading to the conception of this research subject and the research purpose are clarified by examining the synthesis of the core/shell structure and the correlation between this structure and optical properties.

In Chapter 2, we optimized the synthesis and ZnS shell formation conditions for narrowing the size distribution of InP QDs, determined the critical thickness of ZnS films for maintaining coherent InP/ZnS core/shell structures, and analyzed the correlation between coherent nanostructures and optical properties in detail. The coherent core/shell structure exists as a so-called single crystal having the same lattice constant of 0.56 nm over the entire core/shell QD as a result of isotropically compressing the core crystal and conversely expanding the shell crystal when the InP serving as the core is controlled to have a particle size smaller than 2.95 nm and the film thickness of ZnS being the shell is 1.08 nm or less, and is stable in room temperature and air. In spite of the fact that the core and the shell are composed of different materials, the lattice-matched interface is formed, so that the optical characteristics are excellent. For example, the fluorescence quantum yield (PLQY) of

photoluminescence was 70%, and the full width at half maximum (FWHM) of PL spectrum was 35 nm, showing excellent performance such as compatibility of optical characteristics which are not comparable in alloy systems.

In Chapter 3, we performed low-temperature photoluminescence measurements to discuss the mechanism of the unique optical properties observed in the coherent core/shell structure. Coherent core/shell QD and non-coherent core/shell QD coated with ZnS shells of different thicknesses were prepared as samples for InP core QD of the same lot, and PL measurement was carried out in the temperature range of 4 -298 K using a cryostat. The results of the temperature dependence of the PL-FWHM reveal that the observed increase in PL-FWHM in the non-coherent core/shell QD is not due to phonon-electron interaction but to the physical shape of the shell.

In Chapter 4, a PD device having a coherent core/shell QD in an active layer was fabricated. Ligands such as palmitic acid bonded to the QD surface have a long alkyl chain, so steric hindrance is strong, and the distance between the QDs becomes long when the QDs are thinned by spin coating. As a result, the carrier mobility in the thin film became low, and the device performance deteriorated. To solve this problem, ligand exchange was performed to a hydrophilic ligand with a short alkyl chain. As a result, the film-forming property of the QD on the zinc oxide thin film which serves as the electron transport layer is improved, and at the same time, the distance between the QDs in the active layer is shortened. The PD element structure was energy aligned so that the energy diagrams of ZnO and QD were Type-II type from the viewpoint of carrier separation of excitons generated by optical absorption. These structural mechanisms worked effectively, and we succeeded in fabricating the first PD device in the InP system. Furthermore, the PD element showed excellent optical response characteristics. First, the time required for the rise of the signal waveform was 4 msec and the

time required for the fall was 9 msec. These response times were the fastest among Cd-free QD PDs reported so far.

Chapter 5 summarizes the conclusions and provides an overview and perspective on the effectiveness and potential of the coherent core/shell InP/ZnS QDs presented in this study as phosphors.

In short, the author has realized a coherent core/shell QD structure for the first time in an InP system by using InP, a typical III-V semiconductor, as a core and ZnS as a shell, and has investigated the conditions for the structure formation. The findings obtained in this study show that the coherent core/shell structure, which was conventionally thought to be possible only in a part of II-VI semiconductors, is also possible in other semiconductors including III-V semiconductors, thereby expanding the versatility of this structure, and contributing to future application development.

Chapter 1: Introduction

Preface

The subject of this research is "Colloidal Synthesis of Coherent InP/ZnS Core/Shell Nanocrystals for Optoelectronic Applications" In this section, we describe the fundamental characteristics and synthesis theory of QDs, and then describe the research subjects of InP QDs.

1.1 Colloidal Quantum Dots Overview

Nanometer-sized particles (about 2 ~ 10 nm) composed of about $10^3 \sim 10^5$ atoms synthesized and suspended in the solution phase are called colloidal quantum dots (QDs). By the high temperature organometallic synthesis method reported in 1993, it became possible to synthesize semiconductor nanoparticles with good crystallinity whose particle size was controlled.¹ Since then, the elucidation of the structure and physical properties of semiconductor nanoparticles has dramatically improved. Since QDs can easily produce solids directly from the solution phase and can adjust emission and absorption spectra in a wide range by quantum size effect, there is a growing interest in materials. With applications ranging from solar cells ^{2,3},LED^{4,5},photodetection ⁶⁻¹¹,lasers ¹²,bioimaging ¹³ QDs contribute to the development of new technologies.

1.2 Quantum size effect

The electronic states of atoms and molecules take discrete levels, but when atoms cluster together to form larger particles, they eventually form a continuous band of energy states. In descending order of size, a cluster of about $10 \sim 10^2$ atoms has a crystalline nature different from that of a molecule.

The number of orbitals increases and the energy between the orbitals gradually decreases when the size of the nanoparticle composed of about $10^3 \sim 10^5$ particles with a particle size of $2 \sim 10$ nm is reached (Figure 1.1). The particles in this region have electronic properties intermediate between those of bulk semiconductors and isolated molecules. Further, as the crystal size increases, a valence band in which bonding orbitals are continuously gathered and a conduction band in which antibonding orbitals are continuously gathered are formed. The energy band gap (E_g) decreases as the size increases, and finally converges to the value of the bulk semiconductor. In particular, E_g strongly depends on the size if the nanoparticle radius is less than or equal to the exciton Bohr radius. Therefore, QD can control the emission and absorption wavelength only by the size even in the same material. Since the energy state changes in this way depending on the size, it is also called quantum size effect (quantum confinement effect).

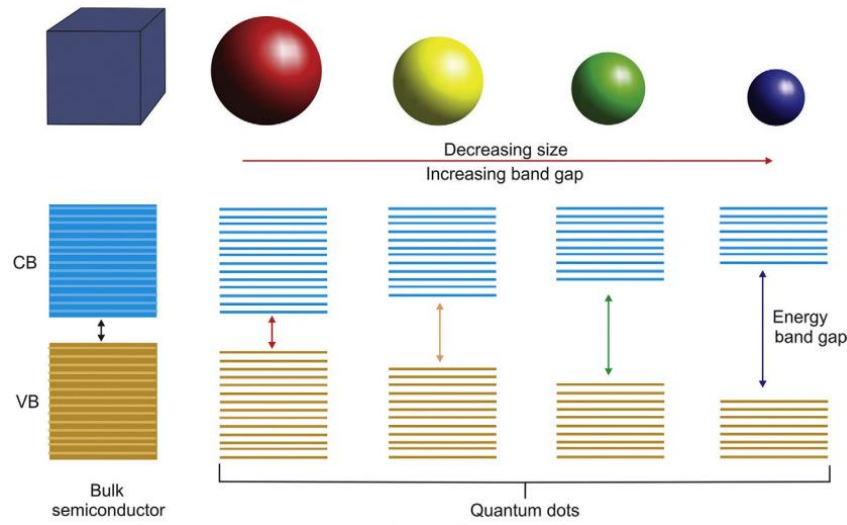


Figure 1.1 The relation between the size of QDs and the band gap: In bulk semiconductors, a zonal conduction band and a valence band are formed. As the size gradually decreases, each orbit becomes a discrete level and the band gap increases.¹⁴

Next, excitons are described to understand the relation between size change and optical properties in more detail. In the case of bulk semiconductors, electrons in the valence band migrate to the conduction band when they absorb energy higher than the energy gap (photoexcitation). On the other hand, holes are formed in the valence band. The electrons and holes are bound to each other by the electrostatic Coulomb force. These bound electrons and holes are called excitons. This exciton can be treated like a negatively charged electron and a positively charged nucleus of a hydrogen atom. The electrons and nuclei of hydrogen atoms are bound by the size of the Bohr radius. For excitons, electrons and holes are bound by the Coulomb force, as for hydrogen atoms, and their magnitude is the exciton Bohr radius r_B . The relation between r_B and the exciton binding energy E_B is as follows.

$$E_B \cdot r_B = \frac{e^2}{2\epsilon} \quad (1)$$

ϵ is the dielectric constant of the semiconductor. When the Coulomb force is strong and E_B is large, the value of r_B becomes small. Therefore, the magnitude of r_B varies depending on the semiconductor material. For example, the exciton Bohr radius r_B of CdSe, a Cd based QD, is 4.6 nm, and the InP used in this study is 9.6 nm.

The stability of excitons in bound states varies with particle size. When the particle size is large, excitons can exist stably. On the other hand, when the particle size is decreased down to the nanoscale, the excitons are spatially confined and the possible energy states are reduced. Eventually, the energy state becomes discrete, and the lowest energy of the exciton shifts toward higher energies (quantum confinement effect). The energy shift depends on the material. For example, because the Bohr exciton radius of InP is larger than that of CdSe, InP is more confined even though it has the same particle size as CdSe. Therefore, the quantum confinement effect is roughly divided into two models, in which the exciton motion differs greatly depending on the size of the Bohr radius r_B and the radius (R) of the nanoparticle.¹⁵

1.2.1 Exciton confinement (weak confinement) of $r_B < R$

If R is greater than r_B , the exciton can exist stably in the particle. The exciton character center-of-gravity motion is confined as in bulk crystals. The minimum exciton energy E_n is as follows.

$$E_n(R) = E_g - \frac{\hbar^2}{2Mr_B^2} + \frac{\hbar^2}{2M} \left(\frac{\pi}{R}\right)^2 \quad (2)$$

E_g is the band gap of the bulk semiconductor, M is the centroid effective mass of the exciton, $M = m_e^* + m_h^*$, and m_e^* and m_h^* are the electron effective mass and the hole effective mass, respectively. The second and third terms on the right side represent the exciton binding

energy and the centroid kinetic energy of the exciton, respectively.

1.2.2 Individual electron and hole confinement (strong confinement) of $r_B > R$

For $r_B > R$, the exciton is larger than in the fine particles, so the electrons and holes are confined in separate potentials and are subjected to Coulomb attraction. The lowest exciton energy E_n is as follows.¹⁶

$$E_n(R) = E_g + \frac{\hbar^2}{2\mu} \left(\frac{\pi}{R}\right)^2 - 1.786 \frac{e^2}{\epsilon R} - 0.248 E_B \quad (3)$$

$$E_B = 13.6 \frac{\mu}{\epsilon m_0} \quad (4)$$

μ is the reduced effective mass, $\mu = 1/(1/m_e + 1/m_h)$, E_B is the exciton binding energy, and m_0 is the electron mass. The right-hand third and fourth terms are the Coulomb terms and the slightly modified binding energy terms. The kinetic energy term of the second term on the right side varies greatly with the particle size. The shift of the lowest exciton energy is larger in the electron and hole individual confinement than in the exciton confinement. This is because the reduced effective mass μ is smaller than the centroid effective mass M of the exciton. Therefore, the QD of $r_B > R$ shows a remarkable change in emission or absorption characteristics depending on the size.

Eq.(3) is also referred to as the effective mass approximation model, and gives the luminescence relation to the size of the QD. Since this model calculates the effective mass in bulk, it is not applicable as the particle size decreases, but it is possible to grasp the relation between size and emission.

Thus, since QD can change optical properties only by particle size, it has the potential to provide a new approach to material design. One of the attractive points is that this QD size

can be prepared only by the parameters under synthesis.

1.3 Synthesis theory of QD

Thermodynamics shows that chemical reactions in solutions are governed by equilibrium constants that are strongly dependent on temperature. The rate of chemical reaction between precursors is proportional to the product of the concentrations of the reacting precursors. Therefore, atmosphere control, temperature control, and solute concentration are particularly important in the growth of quantum dots by chemical reactions.

The first growth is the nucleation of compounds by chemical reactions of multiple precursors, followed by the growth of small quantum dots. Reaction precursors, which are used as raw materials for quantum dots in solution, undergo pyrolysis or chemical reactions, and are dissolved into the solvent as monomers. When the concentration of monomers locally increases and exceeds a certain threshold (critical concentration), crystal nuclei are formed, which is called nucleation.

LaMer first outlined that in a typical precipitation reaction in a closed system, nucleation is thermodynamically possible when the free monomer concentration $[M]$ is above a critical concentration $[M_C]$.¹⁷ At this point, the solution becomes supersaturated. The supersaturated state S is defined by $S = [M]/[M_\infty]$, where $[M_\infty]$ is the equilibrium solute concentration (solubility) in an infinite flat surface. During nucleation, the monomer is rapidly consumed, resulting in a smaller $[M]$. The monomer concentration $[M]$ eventually falls below $[M_C]$ and nucleation stops. For newly formed nuclei of radius r , $[M]$ is much higher than the equilibrium monomer concentration $[M_a]$ (the monomer concentration required to prevent particle dissolution), even though nucleation has ceased. Therefore, the formed crystal nucleus of radius r is thermodynamically stable and does not decompose into atoms or ions, although the

concentration becomes locally heterogeneous in the solvent. Therefore, the nuclei with radius r grow with the addition of the monomer.

Since nucleation requires the formation of a new phase, it must cross the thermodynamic potential barrier. The energy that drives nucleation, the Gibbs free energy of the whole system, is given by the sum of the surface and bulk terms.

$$\Delta G_T = \Delta G_B + \Delta G_S \quad (5)$$

For spherical nuclei (radius: r), the surface contribution (ΔG_S) increases the free energy of the system according to $\Delta G_S = 4\pi r^2 \gamma$, where γ is the surface energy. On the other hand, the bulk contribution (ΔG_B) decreases the free energy by $\Delta G_B = (4\pi r^3/3) \Delta G_V$. ΔG_V is the Gibbs free energy per unit volume. Here, R , T , and V_M are the gas constant, temperature, and molar volume of the monomer, respectively, assuming that $\Delta G_V = - (RT/V_M) \ln S$, the total free energy as a function of the nucleus radius is expressed as follows.

$$\Delta G_T = -\frac{4\pi r^3 RT (\ln S)}{3V_M} + 4\pi r^2 \gamma \quad (6)$$

Figure 1.2 plots the surface (ΔG_S , dotted line), bulk (ΔG_B , dashed), and total free energy (ΔG_T , solid line) under certain standard reaction conditions. For small nuclei with a large surface to volume ratio, the surface term dominates the free energy. However, as the nucleus becomes larger, the bulk free energy term becomes dominant, and ΔG_T rises to its maximum (the red part of the curve) and then decreases. This maximum thermodynamic potential, ΔG_N , represents the energy required to form a stable nucleus for a given supersaturation, surface energy, and temperature. The radius corresponding to this ΔG_N is

known as the critical radius r_{crit} . r_{crit} with $d\Delta G_T/dr = 0$ can be expressed as:

$$r_{crit} = \frac{2\gamma V_M}{RT(\ln S)} \quad (7)$$

In addition, the thermodynamic potential, ΔG_N , at the critical radius, r_{crit} , is given by:

$$\Delta G_N = \frac{16\pi\gamma^3 V_M^2}{3R^2 T^2 (\ln S)^2} \quad (8)$$

Because the system tries to lower the free energy, the nuclei with $r > r_{crit}$ can lower ΔG_T upon growth by monomer addition, and the nuclei with $r < r_{crit}$ can lower ΔG_T by partial or total dissolution. Thus, the critical radius r_{crit} represents the size that separates the stable and metastable nuclei. The top right inset of Figure 1.2 shows the gradual change in ΔG_T that occurs when a nucleus grows from a single monomer to a critical size. In this figure, n represents the number of atoms (monomer units) contained in the nucleus, and the change in free energy generated in the system when monomers are formed into dimers and trimers is accurately displayed. Such a continuous addition of monomers increases the total free energy of the nucleus, which changes from metastable to stable when it reaches a critical size of p monomer units.

It is found that the barrier for the incorporation of one monomer unit is the smallest n which is the largest and becomes zero in the order of $n \rightarrow p$. This means that at the beginning of nucleation, the reaction solution contains a very high concentration of monomers and a small number of dimers, trimers, etc.

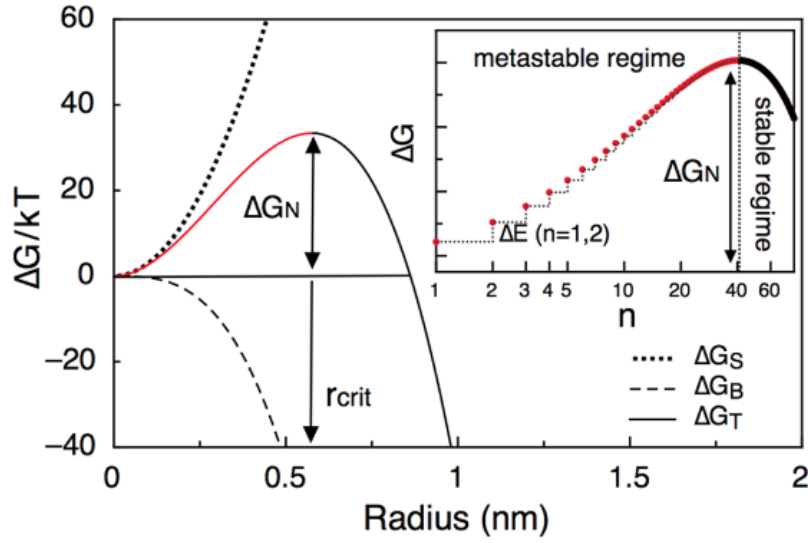


Figure 1.2. The relation of particle size to (ΔG_S), bulk (ΔG_B), and total (ΔG_T) free energies.¹⁸ The red lines represent metastable nuclei at the thermodynamic potential ΔG_N . It changes to a stable nucleus around the critical radius r_{crit} . The inserted graph represents ΔG with the x-axis as the monomer unit.

As the reaction proceeds, stable nuclei exceeding the critical size are formed, and the nuclei continue to grow. $[M]$ still exceeds $[M_\infty]$ (solubility) and monomers are consumed through the reaction, but $[M]$ eventually falls below $[M_a]$ (monomer concentration required to prevent dissolution of particles) and shifts to the coarsening process, Ostwald ripening. In this second stage of growth, small nuclei dissolve because of their high surface energy and deposit into larger nuclei. Therefore, the average particle size increases with the disappearance of small nuclei. Furthermore, Ostwald growth is generally characterized by an expanded size distribution.¹⁹ Such growth after nucleation is expressed by the following equation.²⁰

$$\frac{dr}{dt} = \frac{2\sigma DC_\infty}{d_m^2 kT} \frac{1}{r} \left(\frac{1}{r^*} - \frac{1}{r} \right) \quad (9)$$

where r^* is the radius at which growth stops because the crystal is in equilibrium with the

solution, D is the diffusion coefficient of the monomer in the solution, and C_∞ and σ are the vapor pressure and surface tension of the flat crystal surface respectively. For $r^* > r$, the growth rate is negative and melting is preferred for smaller crystals than for feeding new monomers. This means that r^* has the same meaning as the critical size r_{crit} which characterizes the position of the energy barrier during nucleation. As represented by equation (7), the critical size r_{crit} depends on the monomer concentration. As the reaction proceeds, the monomer concentration $[M]$ decreases and the r_{crit} increases.

The general crystal radius dependence of the growth rate is shown in Figure 1.3. Interestingly, there is the maximum growth rate at radius $2r^*$ ($2r_{crit}$). If the radius r of a QD is greater than $2r^*$ ($r > 2r^*$), the size distribution narrows with time because small QDs grow faster and large QDs grow slower. This region is called the size-focusing region. On the other hand, when the radius of QD is $r^* < r < 2r^*$, the size distribution becomes wider with time because small QDs grow slowly and large QDs grow fast. The region in which this size distribution extends is called the broadening regime; instead, the growth rate of small QDs becomes negative and decomposes in the presence of small QDs with $r^* > r$ (the state of $[M] < [M_a]$). The monomer binds to a large QD, which reduces the number of QDs in the whole system. This region is called the Ostwald ripening regime.

When considered as a practical synthetic system, r^* is sufficiently small because of the high monomer concentration $[M]$ at the initial synthetic stage. So the composition starts with the size-focusing regime. As growth progresses and the monomer concentration $[M]$ decreases, r^* increases. The synthesis proceeds to the broadening regime, the Ostwald ripening regime. Therefore, the nucleation process strongly affects the size distribution of the final sample.¹⁷ Ideally, the nucleation process should be terminated before entering the size growth region. Therefore, the sharpness of this nucleation process (rapid nucleation in time) is very

important.¹⁷ Conversely, if the nucleation process takes a long time, the first nucleated QD is already overgrown and has a wide size distribution. In such cases, the effect of size-focusing on narrowing the average size of the QD may not be sufficient. It is important to note that all QDs grow with an overall size-focusing. The solution of the problem on this size distribution is tried by the improvement of the synthesis method. In the next session, we will describe the synthesis methods for size control of these QDs and the effects of organic ligands.

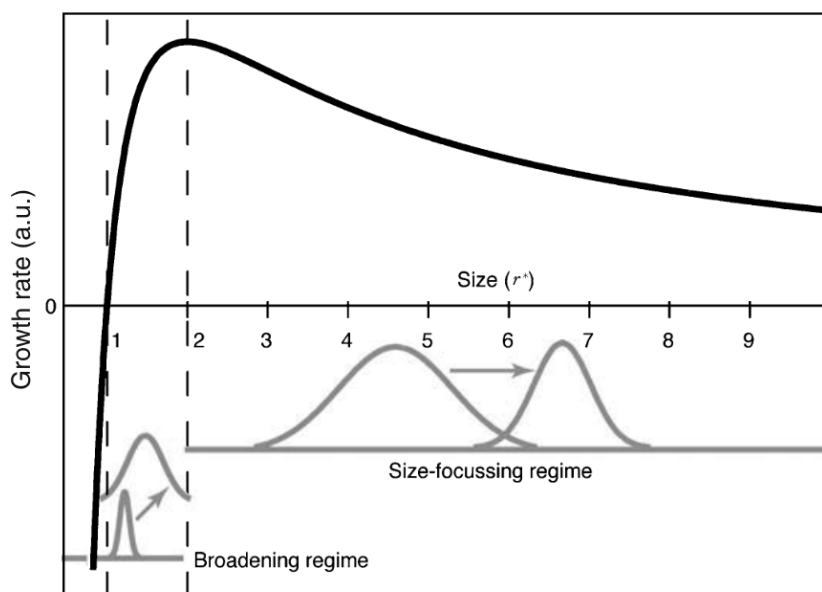


Figure 1.3. Relation between critical size r^* and growth rate dr/dt .²⁰ The area with $r^* > 2$ is called the size-focusing regime, and the area with $1 < r^* < 2$ is called the broadening regime. Two size distributions and their time evolution are shown as examples. In the two regions, the particles grow with time, but the size distribution tends to be different. The size-focusing regime has a smaller size distribution, and the broadening regime has a larger size distribution.

1.3.1 Hot injection method

In early 1980, the relation between the size of QDs and their absorption spectra was explained.¹⁵ However, because the synthesized QD sizes were uneven, understanding of the

quantum effects inherent in nanoparticles was slow. The approach for synthesizing monodisperse QDs is mainly based on the work of LaMer.¹⁷ In 1993, Alivisatos and Bawendi et al. succeeded in synthesizing CdS, CdSe, and CdTe QDs whose sizes were arranged by introducing the "hot injection" method based on the research of LaMer.^{1,21} By this synthesis method, the elucidation of electronic structure and optical property of semiconductor nanoparticle will advance. To date, the most common method for synthesizing QDs is hot injection. Figure 1.4 shows the outline of the hot injection method.

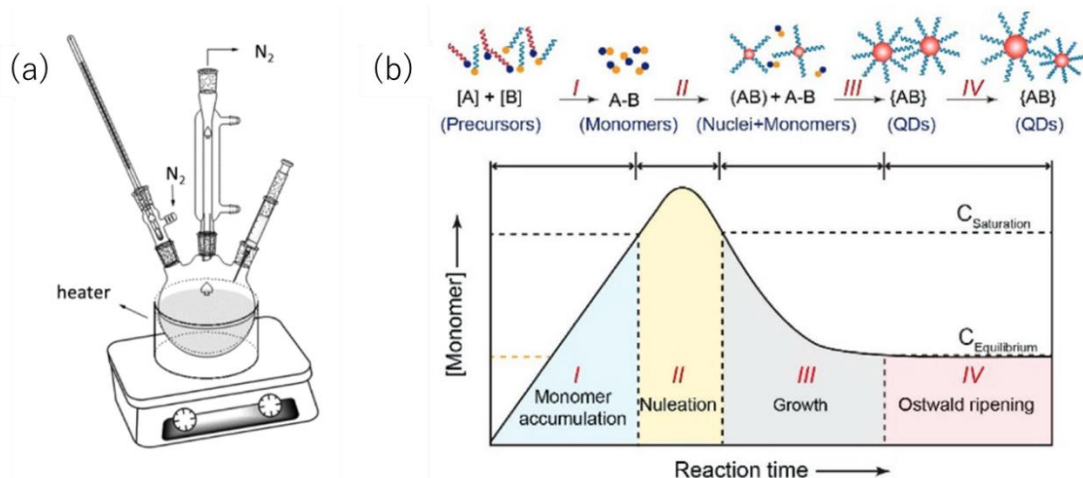


Figure 1.4. Hot injection method overview. (a) A three-neck flask is used for the synthesis;. One branch is for thermometer and the other for syringe injection. A cooling channel is set in the center. The flask is filled with inert gas. ²² (b) LaMer plot corresponding to the relation between reaction time and monomer concentration in QD synthesis. Monomer accumulation (I), nucleation (II), growth (III), and Ostwald ripening (IV). The LaMer plot shows the change in monomer concentration as a function of reaction time. When the monomer concentration exceeds the saturation limit ($C_{Saturation}$) at the monomer accumulation stage (Stage I), the self-organization of the monomer initiates nucleation (Stage II). The nucleation process is then terminated when the A-B monomer is rapidly consumed and the monomer concentration drops below the $C_{Saturation}$. Thereafter, A-B monomers are deposited on the AB nuclei and crystal growth begins (stage III). When the A-B monomer concentration reaches the equilibrium concentration ($C_{Equilibrium}$), thermodynamically driven Ostwald ripening dominates the interparticle reaction, leading to the dissolution of small AB nanocrystals and the redeposition of dissolved species on the large crystal surface (Stage IV). Because Ostwald ripening generally results in an expanded size distribution, QDs synthesis must be stopped in time to avoid harmful interparticle reactions.⁴

The heater with temperature controller is set below the 3 neck flask as in Figure 1.4(a). In one of the three ports, a temperature sensor is set to measure the temperature of the solvent. Set the rubber plug for injection of the reaction reagent using the syringe in the other of the three ports. One port in the center is connected to the Schlenkline of vacuum and gas piping in which vacuum and nitrogen and argon substitution sealing can be selected by the cock. An anoxic atmosphere is necessary to prevent the oxidation of solutes and quantum dots.

Figure 1.4(b) gives an overview of the reaction process. The growth of QDs by the liquid phase process proceeds with the chemical reaction of the precursors in the solvent. In the hot injection method, 2 or more precursors are combined, and the nucleation is rapidly performed at a high temperature of about 150 ~ 300 °C.²³ [A] precursor and solvent are placed in a three-neck flask, and the mixture is heated to about 300 °C. The precursor then releases the monomer by pyrolysis (Stage I, Figure 1.4(b), Figure 1.5). Another [B] precursor is rapidly injected into a mixture of high temperature and high monomer concentration. At this time, a chemical reaction between the precursors causes a rapid supersaturation of the monomer. Nucleation by self-assembly of monomers occurs in short bursts (Stage II, Figure 1.4(b), Figure 1.5). This nucleation takes only a few seconds to complete and produces uniformly sized nuclei. A sharp drop in the monomer concentration and a sharp drop in the reaction temperature suppresses further nucleation, resulting in the deposition of monomers in the nucleated nuclei and the promotion of nuclear growth (Stage III, Figure 1.4(b), Figure 1.5). In this nucleation process, the set temperature of the temperature controller is lowered (about 50 °C) to control the nucleation process. The size distribution of the last generated CQD undergoes Ostwald ripening (Stage IV, Figure 1.4(b), Figure 1.5). In this process, small CQDs dissolve due to the high surface energy and deposit on large QDs. Since nucleation and growth are separated in the hot injection method, it is possible to obtain QDs of arbitrary size

depending on the growth time. In cadmium (Cd) -based QDs, monodisperse QDs with a size distribution less than 5% have been successfully obtained.²⁴ Furthermore, this method is used for IV-VI (For example, PbS²³), III-V (For example, InP²⁵), perovskite (For example, all-inorganic perovskites CsPbX₃, X = Cl, Br, I²⁶) QD, etc. and has high versatility. Therefore, it is the best method for synthesizing unknown QD materials.

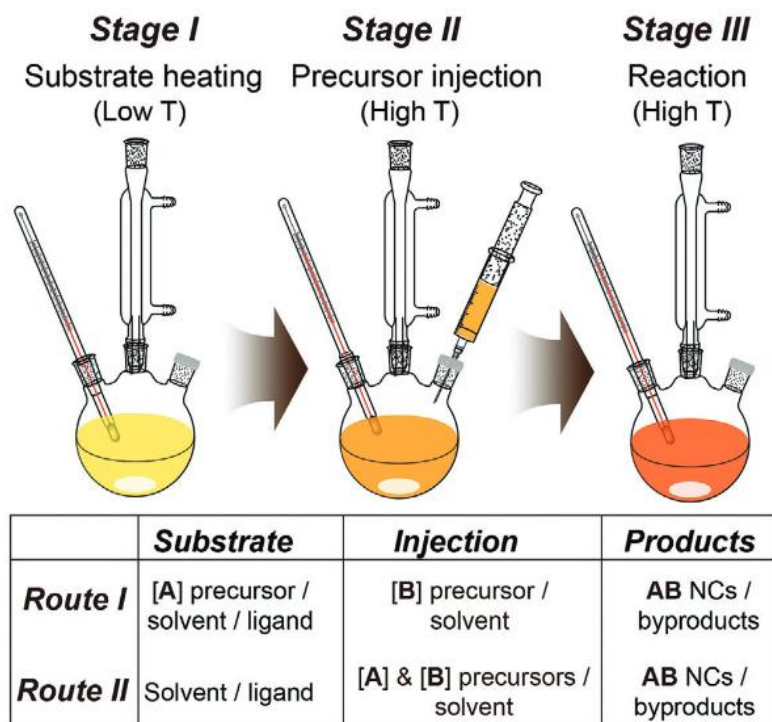


Figure 1.5. Schematic diagram of QD synthesis by hot injection. [A] precursor and solvent are previously placed in a flask (route I). After heating the mixture, [B] precursor is rapidly injected into the high-temperature [A] precursor. Alternatively, both [A] and [B] precursors are injected into the hot solvent (route II).

On the other hand, synthesis employing a well-established hot injection method has the following insurmountable drawbacks.

- (1) Uniform Mixing of Reagent Injection: Hot injection synthesis requires rapid and uniform mixing of reagents at high temperatures to achieve controlled nucleation events. Mixing takes longer when the injection amount is large. This makes the synthesis dependent on the injection scale and method, making the results difficult to predict.
- (2) Reaction cooling time: After the nucleation process ends, the reaction temperature must be lowered to slow down the growth of QDs. The cooling time is quite dependent and the reaction results are distorted.
- (3) Practicality: A large amount of injection does not maintain the temperature of the hot solvent. Therefore, it is not practical to inject a large amount, and the feasibility is low.
- (4) Reproducibility: The time taken to inject the reagent depends on the amount and method and the user. This makes a small difference in the initial reaction rate, which interferes with reproducibility. When these factors are combined, the reaction conditions vary greatly, and it is very difficult to reproduce the synthesis of high quality NC in a small amount on a large scale. In the hot injection method, the synthesis is carried out at a high temperature and supersaturated state, so unintended reaction may occur.

1.3.2 Heat up method

While hot injection is often used as a synthesis of QDs, another approach is a heat-based approach (Heat-Up method, non-injection method, and one-pot method). In reactions employing this methodology, all solvents, ligands, and precursors are mixed into the reaction vessel prior to heating. The mixed solution is then heated to induce the nucleation and growth of the QDs. This method does not require injection of precursors after heating and is

therefore independent of scale and injection time. Therefore, this method avoids all the drawbacks of the hot injection method and achieves excellent reproducibility. The control of the QD size is also possible in the heat up method.²⁷

Figure 1.6 shows a schematic of the relation between the key steps of QD formation in a typical heat-up synthesis and the temperature of the reaction vessel. The precursor is defined here as the source of the monomer. Solvents, ligands and all precursors are placed in a flask and mixed before heating. At this low temperature, most of the mixed solution is composed of precursors rather than monomers. These precursors can be the first reagents used or secondary complexes formed in reaction with ligands in solution. When the mixture is heated, these precursors have an increased thermodynamic drive to form monomers. The heat-up method ultimately causes the nucleation of nascent microcrystals, and continuous heating is required to grow these nuclei. The basic particle formation mechanism of the heat up method is basically the same as that of the hot injection method. Unlike the hot injection method, the formation of monomers occurs simultaneously with the nucleation of nanocrystals. Therefore, it is important that the nucleation is fast enough to produce a large number of nano-sized nuclei in a relatively short time because of the size distribution. In addition, since the heat up method requires continuous heating, a high degree of control is required to separate the nucleation and growth stages. Control of this chemical reaction is a particularly important consideration in multi-element QDs and requires matching the reactivity of each component during the heating step. Therefore, it is necessary to appropriately select the combination of the precursor in order to synthesize the high-quality QD. It is also necessary to have a variety of reagents. This complexity may hamper its widespread use.

In recent years, as the field of QD synthesis has advanced and understanding of individual systems has deepened, heat-up methods have become more common. Heat-up, in which a

single mixture is gradually heated to produce a QD, is a simple and reliable means of providing high reproducibility because it is scale and user independent. Future development of the heat-up process must proceed with the aforementioned precursor chemistry, reagent form, and thermal management in mind.

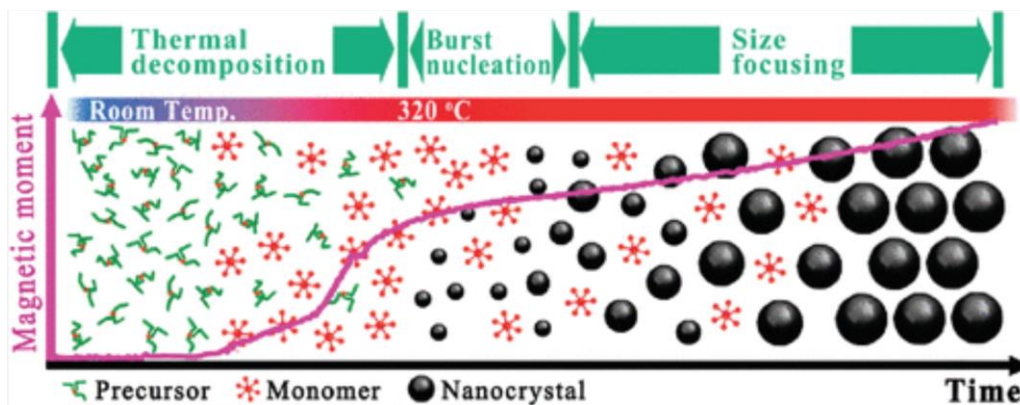


Figure 1.6. Schematic diagram of the heat up method ²⁸

1.4 Application to optoelectronics

QDs can emit light of any color from the same nanocrystalline semiconductor as its size changes. This means that the size of the QD can be highly controlled and adjusted during the synthesis process to emit light of any color. This is because the energy required to excite electrons from the valence band to the conduction band (band gap) varies with size. Therefore, a large QD emits light at a long wavelength, such as red, and a small QD emits light at a short wavelength, such as green. The same is true for light absorption: large QDs absorb longer wavelengths, and small QDs absorb shorter wavelengths. In this way, QDs are most suitable for optoelectronic applications because the optical properties can be varied depending on the size to suit a particular application. Potential applications for QDs range from solar cells, ³ transistors,⁷ diodes, ⁸ lasers,¹² light emitting diodes (LED), ²⁹ biomedical applications, ^{30,31} wastewater treatment, ³⁰ spin coating ³¹. This session will discuss the applications of

optoelectronics and each application.

1.5 Display using QLED

The next generation display technology is expected to realize the near future society in which image information and the real world are fused such as AR (Augmented Reality) and VR (Virtual Reality) representative. The μ -LED and compact laser technologies that support them require a device size of 50 μ m, a response speed of nanoseconds, and an electroluminescence (EL) spectrum width (EL-FWHM) of 40 nm or less to improve color purity (Table 1.1). However, no conventional material can satisfactorily meet these requirements. For example, in comparison with the EL-FWHM, the β -SiAlON green emission phosphor for liquid crystal display (LCD) is 45 nm and the TADF red emission phosphor for organic EL (OLED) is 42 nm, and the EL-FWHM is not 40 nm or less. Recently, LEDs (QLED) using QDs that achieve these requirements have attracted attention. QLED displays have brighter and purer colors, are power efficient, and are incredibly vibrant (FWHM: 30 nm or less).³² QLEDs also emit light by themselves, unlike traditional displays, making them suitable for miniaturization. QLED with such excellent performance is achieved by Cd based QD. Figure 1.7 shows the recent trend of external quantum efficiency (EQE) of QLED using Cd-based QD. The EQE of Cd-based QLED has rapidly improved since 2012, and the practical application target of 20% was achieved in 2018.³² As of 2022, some Cd-based QLEDs have already been put into practical use and are sold as QD displays. 1.3 million displays using QD technology were shipped worldwide from 2015. QD display shipments were expected to grow to 18.7 million units in 2018 (Figure 1.8). It is projected that 51% of monitors will adopt QD by 2026. In the future, QD is expected to become an essential technology for next-generation displays.¹³

Table 1.1. Performance requirements of next-generation LEDs

		LED Comparison		
		LED	OLED	QLED
Performance required for next-generation	One element size: 50 μ m	Δ	\circ	\bigcirc
	EL-FWHM: 40 nm or less	\times	Δ	\bigcirc
	Response Rate: nsec Order	\times	\times	\bigcirc

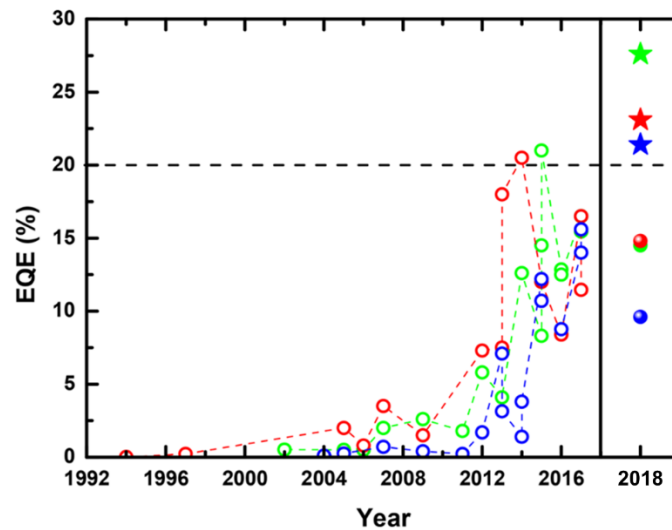


Figure 1.7. EQE trend of Cd-based QLED issued in blue, green, and red.^{30,32-45,45-64} Blue, green, and red in the graph correspond to emission. In 2018, the tandem structure QLED exceeded EQE 20%.³²

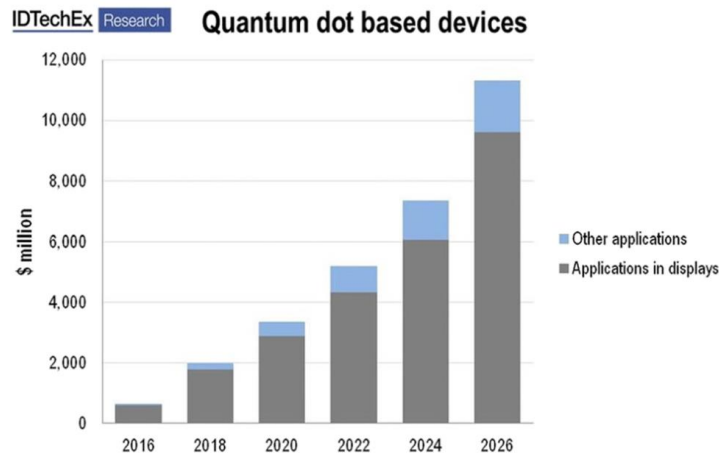


Figure 1.8. Relation between QD devices and components (\$million) over 2016 – 2026

1.6 Photodetector

Photodetectors are very important in many important applications such as imaging, optical communications, and chemical/biological sensing.^{65,66} The principle of operation is to convert an incident optical signal (Ultraviolet, visible, infrared, etc.) into an electrical signal. Semiconductor materials absorb incident light and play a role in the generation of excitons in electron-hole pairs during photoexcitation. Thereafter, in order to separate electrons and holes to generate a current, it is necessary to apply a voltage or separate them by means of a device structure. As bulk semiconductor materials, germanium (Ge)⁶⁷, silicon (Si)^{68,69}, gallium nitride (GaN)^{70–72}, conjugated polymers^{73,74}, and perovskite films^{75–77} have been studied in depth and successfully applied to photodetectors. However, these materials still present costly challenges due to rigorous manufacturing processes and material instability concerns. In order to cope with these problems, QD photodetectors which can be manufactured by a liquid phase process have attracted attention. Depending on the light absorption range corresponding to the band gap, QD-based photodetectors can be broadly classified into three types. The first type is an ultraviolet (UV) photodetector, and some typical materials can be cited as ZnO QDs and ZnSe QDs. Visible (Vis) photodetectors are fabricated based on CdS QDs, CdSe

QDs, or perovskite QDs. The active layer of the infrared photodetector is mainly composed of narrow band gap quantum dots (PbS QD, HgTe QD, etc.). Although the optical absorption range depends on the essentially different bandgap of the QD material, the quantum size effect allows more flexible control of the spectral range. Device structures of QD photodetectors can be classified into three main types: photoconductors, phototransistors, and photodiodes (Figure 1.9).

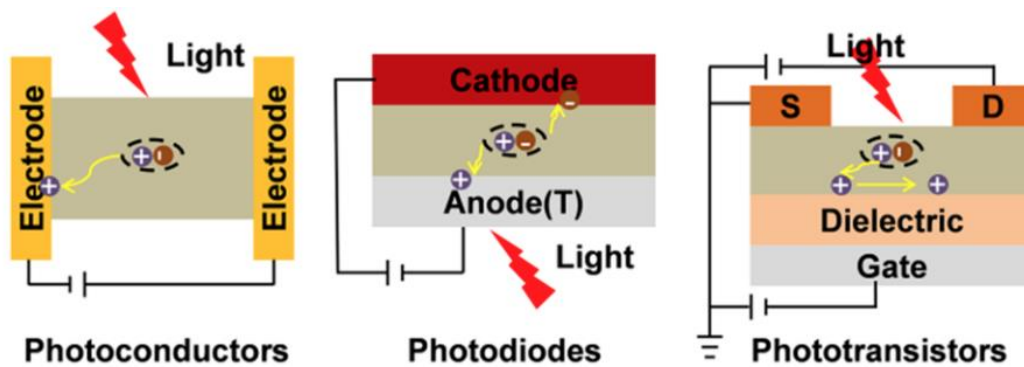


Figure 1.9. Typical device configurations of photodetectors.⁷⁸

1.6.1 Photoconductors

Photoconductors (PC), also known as photoresistors or light-dependent resistors, is based on photoconductive phenomena (Figure 1.9). In the dark, it exhibits greater resistance, followed by more conductivity under appropriate illumination. The typical structure of a device is a semiconductor layer sandwiched between two homogeneous electrodes.⁷⁹ Photogenerated charge carriers are separated by an external voltage and collected at each electrode. One type of charge carrier is usually trapped and has a long lifetime. The other charge carrier can be recirculated until it recombines with the opposite charge. Because of this carrier recirculation, high responsiveness can be achieved. On the other hand, the lifetime of a captured carrier determines the response time and the responsivity simultaneously, so

there is a trade-off between them. As such, PCs typically have relatively high operating voltages, slow response rates, and large dark currents.

1.6.2 Photodiodes

A photodiode (PD) has a device structure very similar to that of a solar cell (SC) and has a (Figure 1.9). Excitons formed by light absorption are efficiently dissociated using the band offsets of the hole transport layer and the electron transport layer. Since the device is driven by the potential difference, light can be detected without applying a voltage from the outside. The electrode is an asymmetric electrode, and at least one electrode uses a transparent substrate. The operation mechanism of the photodiode is as follows: (1) The QD active layer absorbs light energy to generate excitons. (2) The exciton diffuses into the low energy state. (3) Excitons dissociate into free charge carriers (electrons and holes) by internal potential from the device structure or by reverse bias from the outside. (4) Electrons and holes move through the semiconductor layer to the cathode and anode, respectively (5) Free charge is collected at the external electrode, and finally photocurrent is generated. Unlike the SC, the photodiode is a device in which output as a photocurrent signal is more important than power transmission to a load. Compared with PC, dark current is small and response speed is fast.

1.6.3 Phototransistor

Phototransistors (PT) incorporate gate and dielectric layers into photodiodes to reduce noise signals, amplify electrical signals, and ultimately improve responsiveness (Figure 1.9). The dark current is smaller and the response speed is faster than that of the photoconductive element. Compared with PD, dark current is small and response is high. On the other hand, since the amplification process is incorporated, PT is characterized by the need for a high external voltage and a slow response speed compared with PD.

1.7 Solar cell

The power generation principle of the solar cell using QD is almost the same as the dye-sensitized solar cell. The conversion of solar energy to electricity is one of the most developed areas of QD applications. Photovoltaics produced by liquid phase processes can use low-temperature synthesis procedures and roll-to-roll or spray coating production techniques to significantly minimize manufacturing costs.^{2,80} The record high conversion efficiency reported in 2013 was 6%.⁸¹ One year later, a certified conversion efficiency of 8.55% was achieved with PbS quantum dots, and the best samples featured efficiencies of up to 9.2%.^{82,83} This rapid growth in the power conversion efficiency of QD-based solar cells over the past 10 years, along with the development of manufacturing technologies, foresees further expansion of colloidal QDs into the field of renewable energy.

1.8 Toxicity of QD

As explained in 1.7 sessions, most of the high-performance devices contain cadmium (Or lead, Pb). The issue of toxicity due to Cd/Pb elements poses a serious threat to human health and the environment and is a major clinical and therapeutic obstacle. As an example, genotoxic responses of CdTe QDs in human breast cancer cells have been observed, which may lead to long-term adverse effects on biological systems ⁸⁴Due to these toxicities, commercial use of Cd and Pb is severely restricted in Europe in accordance with the Restriction of Hazardous Substances (RoHS) Directive. For example, the maximum allowable concentrations of Cd and Pb are 0.01 wt% and 0.1 wt%, respectively. The maximum allowable concentration is defined as "weight of Cd or Pb/minimum unit of mechanically inseparable parts". Therefore, there is an urgent need to develop alternatives to less toxic materials.

1.9 Alternative material candidates

Figure 1.10 shows the emission ranges of Cd and Pb-based QDs (top) and alternative QDs without heavy metals (bottom). So far, Cd-based QDs have been used to cover the ultraviolet and visible range, while Pb-based QDs have been used for infrared applications. Cd- and Pb-free alternatives include InP, CuInS₂, and Si QDs for the visible and near-infrared regions, and InAs QDs are further extended to the mid-infrared region. For ultraviolet and blue light, PLQY (up to 83%), PL-FWHM (12~20 nm), and EQE (7.83%) were achieved for ZnSe QDs.⁸⁵

PLQY (100%) and PL-FWHM (35 nm) were achieved for the InP QD corresponding to the visible light range from blue to red⁸⁶ EQE achieved 16.3%⁸⁷ at 545 nm of green emission and 21.4%⁸⁶ at 630 nm of red emission, which is equivalent to Cd-based QLED.

CuInS₂, Si QD, and InAsQD show PL QYs of 80%⁸⁸, 60%⁸⁹, 75%⁹⁰ respectively. However, these QDs have PL-FWHM > 80 nm. Applications to QLEDs^{91,92}, solar cells⁹³ and photodetectors⁹⁴ are in progress. On the other hand, the wide PL-FWHM is a big barrier for QLED applications.

Currently, InP is a prime candidate for alternative materials in terms of PLQY, PL-FWHM and EQE.

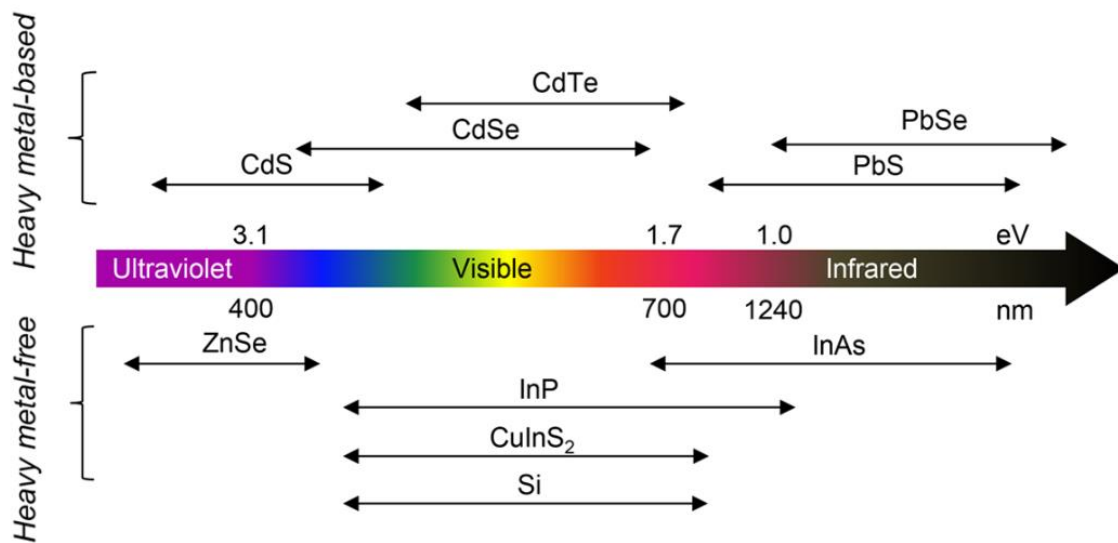


Figure 1.10. List of QDs covering the ultraviolet, visible, and infrared regions ⁹⁵The upper side of the rubber is a QD containing Cd and Pb, and the lower side is an alternative material containing no heavy metals.

1.10 InP QD

InP quantum dots (QDs) are typical III-V semiconductor nanocrystals characterized by large exciton Bohr radii and high carrier mobility. Advantages of InP QDs include a high absorption coefficient, wide color adjustability, and low toxicity. It is therefore ideal for applications in practical settings and provides a promising alternative to traditional Cd/Pb-based QDs. InP is a highly covalent III-V semiconductor. The carrier mobility of III-V semiconductors is superior to that of highly ionic II-VI and IV-VI semiconductors (CdSe, PbS, etc.). However, the optical properties of QDs are superior to those of III-V and IV-VI semiconductors. Although research on InP crystals has been conducted since the 1980 s, ⁹⁶ research on QD is much later than that on Cd-based QD. The reason for this is that InP crystals are formed by covalent bonds. Covalent bond formation usually requires high temperatures, long reaction times, and reactive precursors ⁹⁷. Therefore, size control is

difficult because InP QD synthesis proceeds slowly. As discussed in Session 1.3, the preparation of monodisperse QDs relies heavily on the concept of a "size-focusing regime" for nucleation and nucleation processes ²¹. How to control the nucleation and growth processes to control the size distribution is a permanent challenge in InPQD synthesis.

Advances in InPQD synthesis over the last 20 years are shown in Figure 1.11. A major turning point was the synthesis of InPQD by the heat-up method reported in 2008 ⁹⁸. Previously, InP synthesis took about a day, but in this report the synthesis was completed in a few hours. The final optical properties achieved were PLQY 68% and PL-PWHM 40 nm, which made it possible to synthesize InP QDs with excellent size distribution in a short time. Subsequently, a PLQY of 95% ⁹⁹ for green emission (wavelength: 528 nm) and 100% ⁸⁶ for red emission (wavelength: 630 nm) have been achieved for InP-based QDs by appropriate selection of synthesis protocols and precursor materials in combination with surface passivation. With these attractive optical and electronic properties, InP QDs are a potential material for commercialization in next-generation applications.

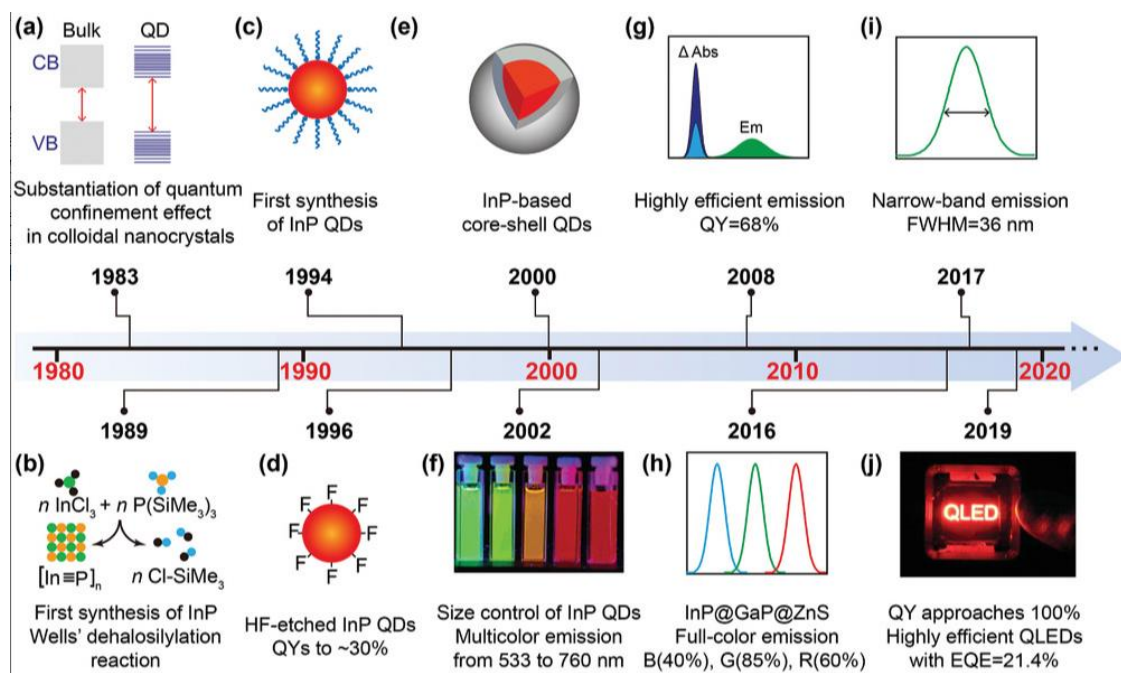


Figure 1.11. InPQD synthesis and optical properties ⁴

1.11 Improved optical properties with core/shell structure

The nanometer crystal size provides a very high specific surface area. The defects on the surface trap the carriers and cause non-radiative recombination. For example, PLQY of InP without any surface treatment is about 1% by the effect of surface defect. Therefore, it is necessary to suppress the effect of this surface defect in order to improve PLQY. One approach is to modify the surface atoms with organic stabilizing ligands. In InPQD, up to 49% of PLQY can be obtained by modifying the surface with zinc oleate (or cadmium oleate).¹⁰⁰ However, a significant portion of these organically passivated QDs typically exhibit surface-associated trap states that function as non-radiative de-excitation channels for photogenerated charge carriers. This is because it is difficult to completely cover the QD surface due to the effect of steric hindrance of organic ligands. Therefore, another approach to further improve the fluorescence quantum yield (QY) is required.

Another important strategy for improving the surface immobilization of the NC is a core/shell structure QD in which the surface of the core QD is coated with another semiconductor material. The shell immobilizes the surface of the core QD, dramatically improving PLQY and stability against oxidation. All InP-based QDs with PLQY > 50% have a core/shell structure.

Two important points in designing a core-shell structure are "Relations between the relative positions of the electron energy levels in the semiconductor bandgap of each core and shell" and "the magnitude of the lattice mismatch between the core and the shell.". The former affects the role of the shell and the latter affects the growth of the shell.

1.12 Relation between the relative positions of the electron energy levels in the semiconductor bandgap of each core and shell

Figure 1.12 shows an overview of the band placement of bulk materials used primarily in QD synthesis. For example, when the core is selected as InP and the shell is selected as ZnS, the band gap of InP is wrapped in the band gap of ZnS. The relation between the relative positions of cores and shells can be classified into 3 types (Figure 1.13).

1.12.1 Type I structure

The band gap of the shell material is larger than that of the core, both electrons and holes are confined to the core, and the shell passivates the surface of the core. Therefore, PLQY is dramatically improved. It is an important structure when it is applied to QLED, etc., because the light emission characteristic is the best among three types. InP-based QD with PLQY 100% takes type I⁸⁶. Commonly used shell materials are ZnSe¹⁰¹, ZnSeS¹⁰², ZnS⁹⁸, GaP¹⁰³.

1.12.2 Type II structure

Depending on the shell, either a hole or an electron is confined but in the core. PLQY and stability can be improved in Type II as well as Type I, but Type II PLQY tends to be lower than Type I¹⁰⁴.

A type II feature is that one of the electrons or holes can move according to the positional relation between the energy levels of the core and the shell. One carrier is trapped in the core and the other in the shell. Type II emission results from the radiative recombination of electron and hole pairs across the core-shell interface. Thus, the type II QD emits light with less energy than the band gap of the core material. The separation of excitons can be applied to applications such as solar cells.

1.12.3 Reverse type I structure

In reverse type I, a shell material with a narrow band gap grows on a core with a wide band gap. Electrons and holes generated by light absorption move the core to the shell and recombine according to the band gap of the shell. Therefore, the light absorption wavelength can be controlled by the core and the light emission wavelength by the shell.

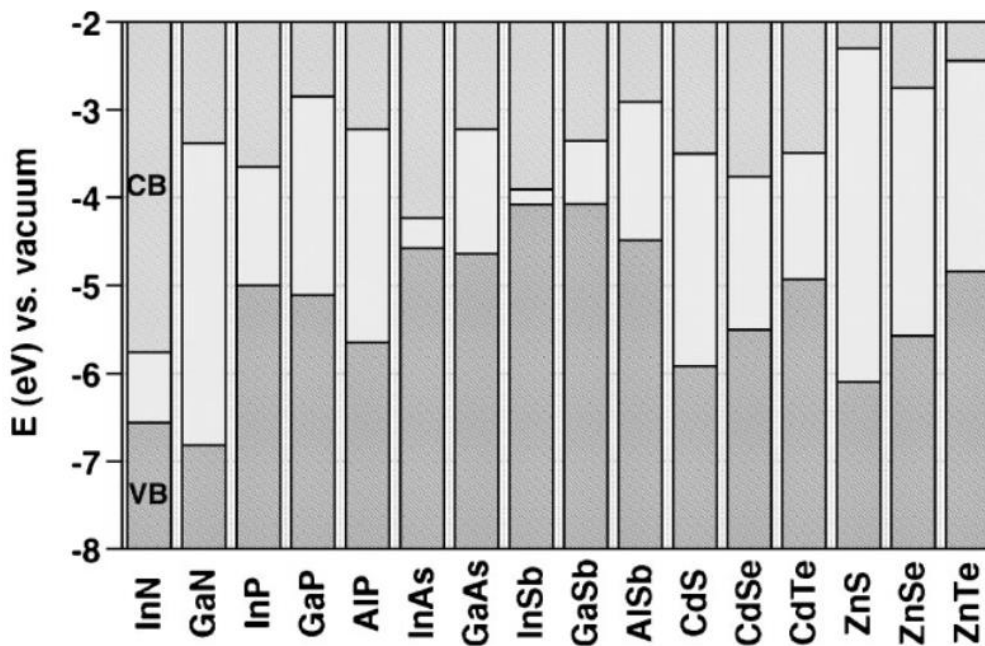


Figure 1.12. Electron energy levels (VB: valence band, CB: conduction band) of III – V and II – VI semiconductors^{105,106}.

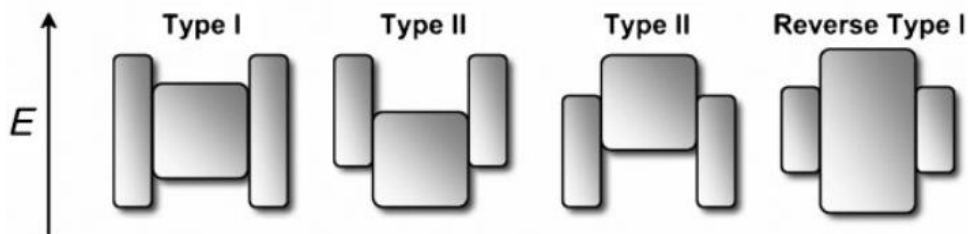


Figure 1.13. Schematic diagram of energy levels in core/shell QDs¹⁰⁶. Squares represent cores and rectangles represent shells. The upper and lower ends correspond to the positions of the ends of the conduction and valence bands.

1.13 Lattice matching between core and shell

In order to synthesize a core/shell structure QD composite with excellent optical properties, it is necessary to minimize the difference (lattice mismatch) between the lattice constants of the core and the shell. The growth of the shell is due to epitaxial growth, and large lattice mismatch results in the formation of strain and defect states at the core/shell interface or in the shell. These defects can act as traps for photogenerated charge carriers and reduce fluorescence QY.¹⁰⁷ Table 1.2 lists the material parameters for semiconductors. In the case of InP (lattice constant: 5.8 Å), choosing ZnS (lattice constant: 5.4 Å) as the shell material results in a large lattice mismatch of 7.7%, although it has a type I structure. In ZnS single substance, the lattice matching is not obtained at the interface between core and shell from the difference of lattice constant with InP. Then, the lattice matching is relaxed by using ZnSe (lattice constant: 5.6 Å) with the intermediate value of lattice constants of InP and ZnS as an intermediate layer. In the core/shell/shell structure in which the inner shell is introduced by ZnSe, the lattice mismatch generated at each interface of InP and ZnSe and ZnSe and ZnS is relaxed by strain, and the defect generation is suppressed. Therefore, the InP/ZnSe/ZnS QD is the most common structure among InP-base QDs because it clears both the type-I structure and the lattice mismatch.

Table 1.2. Physical properties parameters of bulk semiconductors ¹⁰⁶.

Material	Structure [300K]	Type	E_{gap} [eV]	Lattice parameter [Å]	Density [kg m ⁻³]
ZnS	Zinc blende	II–VI	3.61	5.41	4090
ZnSe	Zinc blende	II–VI	2.69	5.668	5266
ZnTe	Zinc blende	II–VI	2.39	6.104	5636
CdS	Wurtzite	II–VI	2.49	4.136/6.714	4820
CdSe	Wurtzite	II–VI	1.74	4.3/7.01	5810
CdTe	Zinc blende	II–VI	1.43	6.482	5870
GaN	Wurtzite	III–V	3.44	3.188/5.185	6095
GaP	Zinc-blende	III–V	2.27	5.45	4138
GaAs	Zinc blende	III–V	1.42	5.653	5318
GaSb	Zinc blende	III–V	0.75	6.096	5614
InN	Wurtzite	III–V	0.8	3.545/5.703	6810
InP	Zinc blende	III–V	1.35	5.869	4787
InAs	Zinc blende	III–V	0.35	6.058	5667
InSb	Zinc blende	III–V	0.23	6.479	5774
PbS	Rocksalt	IV–VI	0.41	5.936	7597
PbSe	Rocksalt	IV–VI	0.28	6.117	8260
PbTe	Rocksalt	IV–VI	0.31	6.462	8219

1.14 Coherent core shell structure

While core/shell/shell structures such as InP/SnSe/ZnS can be used to mitigate core and shell distortion, Nie et al. proposed the interesting idea of using material distortion to construct QDs with coherent core/shell structures.¹⁰⁸CdTe QD (lattice constant: 0.648 nm) was used as the core material, and shells of different types of semiconductors such as ZnS, ZnSe and CdSe were combined as the shell material. These core/shell QDs change the intrinsic interatomic distance of each crystal for coherence as the shell layer grows epitaxially, the spherical core crystal is elastically compressed and the shell crystal is stretched by lattice distortion (Figure 1.14). The shell should have a lattice constant similar to that of the core. When another semiconductor material is epitaxially grown on an ordinary bulk semiconductor substrate, the bulk semiconductor substrate is thick enough to have no lattice constant. The

lattice constant of the thin film semiconductor is distorted to match the substrate. Therefore, this coherent core shell structure is a phenomenon peculiar to nanoparticles.

In addition, they discussed that stress-induced changes in lattice parameters are thermodynamically advantageous compared to the formation of defect trap sites at the core/shell interface and can release strain energy under limited conditions. As expected, the coherent CdTe-based core/shell QD allows a PL spectrum with PLQY of 60% and PL-FWHM of less than 50 nm.¹⁰⁸ This proposed concept was extended by replacing CdTe with CdSe¹⁰⁹.

In the case of QD, the lattice mismatch between the core and the shell does not cause the strain defect, and the possibility of depositing the shell material was shown even in the combination of semiconductors which was difficult in the bulk semiconductor by this idea.

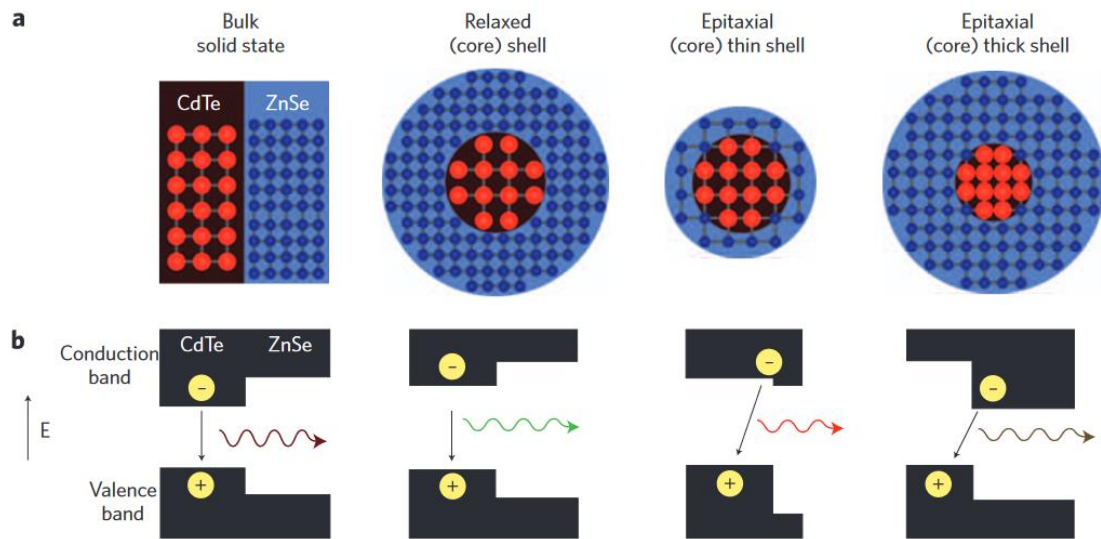


Figure 1.14. Schematic diagram of band energy change due to lattice distortion of QD¹⁰⁸. (a) Conventional Nanocrystals and Strain of (CdTe) ZnSe, (b) The energy levels of the valence and conduction bands corresponding to the structure of a. In the bulk semiconductor, the thin film semiconductor is epitaxially grown in accordance with the lattice constant of the substrate. In the case of nanoparticles, the strain caused by heteroepitaxial growth compresses the core and elongates the shell.

1.15 Research motivation

InP colloidal quantum dots (QDs) have great potential as Cd- and Pb-free alternatives due to their advantages of high carrier mobility, high absorption coefficient, wide color tunability, and low toxicity. In order to improve the optical properties of InP QDs, it is necessary to suppress the function of many surface defects as non-radiative deactivation channels. The core/shell structure QD, as one of the suppression methods, immobilizes the surface by coating different semiconductors on the InP QD, which greatly improves the PL quantum yield (PLQY). The important points in selecting the shell are "Relation between the relative positions of the electron energy levels in the semiconductor bandgap between the core and the shell" and "lattice matching between core and shell". The Type-I structure,

in which the shell bandgap has an energy-level positional relation encompassing the core bandgap, increases the radiative recombination rate of photoexcited carriers, resulting in superior optical properties. For example, the most famous InP/ZnSe/ZnS core/shell/shell structure in the InP QD system satisfies this requirement. ZnSe (lattice constant: 5.6 Å) functions as an intermediate layer to mitigate the large lattice mismatch of 7.8% between InP (lattice constant: 5.8 Å) and ZnS (lattice constant: 5.4 Å). A large lattice mismatch may generate defects at the core/shell interface. Therefore, to obtain excellent optical properties, it is necessary to suppress defects at the core/shell interface and maintain the Type-I structure. Therefore, the shell proposes a coherent core/shell structure with a lattice constant similar to that of the core. It is expected that the spherical core crystal is elastically compressed, the shell crystal is stretched by lattice strain, and defects at the core/shell interface are suppressed.

This paper reports a QD with coherent core/shell structure successfully synthesized for the first time in InP system. The synthetic method, structural analysis, optical properties and the mechanism by which these properties are expressed are discussed. The purpose of the present invention is to describe the effect of a photovoltaic photodiode having a coherent core/shell QD in the active layer on device performance through fabrication and device evaluation.

Reference

- (1) Murray, C. B.; Norris, D. J.; Bawendi, M. G. Synthesis and Characterization of Nearly Monodisperse CdE (E = Sulfur, Selenium, Tellurium) Semiconductor Nanocrystallites. *J. Am. Chem. Soc.* **1993**, *115* (19), 8706–8715. <https://doi.org/10.1021/ja00072a025>.
- (2) Kramer, I. J.; Minor, J. C.; Moreno-Bautista, G.; Rollny, L.; Kanjanaboos, P.; Kopilovic, D.; Thon, S. M.; Carey, G. H.; Chou, K. W.; Zhitomirsky, D.; Amassian, A.; Sargent, E. H. Efficient Spray-Coated Colloidal Quantum Dot Solar Cells. *Adv. Mater.* **2015**, *27* (1), 116–121. <https://doi.org/10.1002/adma.201403281>.
- (3) Halder, G.; Ghosh, D.; Ali, Md. Y.; Sahasrabudhe, A.; Bhattacharyya, S. Interface Engineering in Quantum-Dot-Sensitized Solar Cells. *Langmuir* **2018**, *34* (35), 10197–10216. <https://doi.org/10.1021/acs.langmuir.8b00293>.
- (4) Chen, B.; Li, D.; Wang, F. InP Quantum Dots: Synthesis and Lighting Applications. *Small* **2020**, *16* (32), 2002454. <https://doi.org/10.1002/sml.202002454>.
- (5) Kim, S.; Im, S. H.; Kim, S.-W. Performance of Light-Emitting-Diode Based on Quantum Dots. *Nanoscale* **2013**, *5* (12), 5205. <https://doi.org/10.1039/c3nr00496a>.
- (6) Ren, A.; Yuan, L.; Xu, H.; Wu, J.; Wang, Z. Recent Progress of III–V Quantum Dot Infrared Photodetectors on Silicon. *J. Mater. Chem. C* **2019**, *7* (46), 14441–14453. <https://doi.org/10.1039/C9TC05738B>.
- (7) Fang, J.; Zhou, Z.; Xiao, M.; Lou, Z.; Wei, Z.; Shen, G. Recent Advances in Low - dimensional Semiconductor Nanomaterials and Their Applications in High - performance Photodetectors. *InfoMat* **2020**, *2* (2), 291–317. <https://doi.org/10.1002/inf2.12067>.
- (8) Li, C.; Huang, W.; Gao, L.; Wang, H.; Hu, L.; Chen, T.; Zhang, H. Recent Advances in Solution-Processed Photodetectors Based on Inorganic and Hybrid Photo-Active Materials. *Nanoscale* **2020**, *12* (4), 2201–2227. <https://doi.org/10.1039/C9NR07799E>.
- (9) Yang, C.; Wang, G.; Liu, M.; Yao, F.; Li, H. Mechanism, Material, Design, and Implementation Principle of Two-Dimensional Material Photodetectors. *Nanomaterials* **2021**, *11* (10), 2688. <https://doi.org/10.3390/nano11102688>.
- (10) Yin, X.; Zhang, C.; Guo, Y.; Yang, Y.; Xing, Y.; Que, W. PbS QD-Based Photodetectors: Future-Oriented near-Infrared Detection Technology. *J. Mater. Chem. C* **2021**, *9* (2), 417–438. <https://doi.org/10.1039/D0TC04612D>.
- (11) Guo, R.; Zhang, M.; Ding, J.; Liu, A.; Huang, F.; Sheng, M. Advances in Colloidal Quantum Dot-Based Photodetectors. *J. Mater. Chem. C* **2022**, *10* (19), 7404–7422. <https://doi.org/10.1039/D2TC00219A>.
- (12) Jung, H.; Ahn, N.; Klimov, V. I. Prospects and Challenges of Colloidal Quantum Dot Laser Diodes. *Nat. Photon.* **2021**, *15* (9), 643–655. <https://doi.org/10.1038/s41566-021-00827-6>.
- (13) Mohamed, W. A. A.; Abd El-Gawad, H.; Mekkey, S.; Galal, H.; Handal, H.; Mousa, H.; Labib, A. Quantum Dots Synthetization and Future Prospect Applications. *Nanotechnology Reviews* **2021**, *10* (1),

- 1926–1940. <https://doi.org/10.1515/ntrev-2021-0118>.
- (14) Kumar, D. S. Chapter 3 - Quantum Nanostructures (QDs): An Overview; p 30.
- (15) Efros, A. L.; Efros, Al. L. Interband Absorption of Light in a Semiconductor Sphere. *Sov. Phys.-Semicond.* **1982**, *16* (7), 772–775.
- (16) Trwoga, P. F.; Kenyon, A. J.; Pitt, C. W. Modeling the Contribution of Quantum Confinement to Luminescence from Silicon Nanoclusters. *Journal of Applied Physics* **1998**, *83* (7), 3789–3794. <https://doi.org/10.1063/1.366608>.
- (17) LaMer, V. K.; Dinegar, R. H. Theory, Production and Mechanism of Formation of Monodispersed Hydrosols. *J. Am. Chem. Soc.* **1950**, *72* (11), 4847–4854. <https://doi.org/10.1021/ja01167a001>.
- (18) van Embden, J.; Chesman, A. S. R.; Jasieniak, J. J. The Heat-Up Synthesis of Colloidal Nanocrystals. *Chemistry of Materials* **2015**, *27* (7), 2246–2285. <https://doi.org/10.1021/cm5028964>.
- (19) Peng, X.; Wickham, J.; Alivisatos, A. P. Synthesis and Characterization of Nearly Monodisperse CdE (E = Sulfur, Selenium, Tellurium) Semiconductor Nanocrystallites. *J. Am. Chem. Soc.* **1998**, *120* (21), 5343–5344. <https://doi.org/10.1021/ja9805425>.
- (20) *Semiconductor Nanocrystal Quantum Dots: Synthesis, Assembly, Spectroscopy, and Applications*; Rogach, A. L., Ed.; Springer: Wien ; New York, 2008.
- (21) Peng, X.; Wickham, J.; Alivisatos, A. P. Kinetics of II-VI and III-V Colloidal Semiconductor Nanocrystal Growth: “Focusing” of Size Distributions. *J. Am. Chem. Soc.* **1998**, *120* (21), 5343–5344. <https://doi.org/10.1021/ja9805425>.
- (22) Pu, Y.; Cai, F.; Wang, D.; Wang, J.-X.; Chen, J.-F. Colloidal Synthesis of Semiconductor Quantum Dots toward Large-Scale Production: A Review. *Ind. Eng. Chem. Res.* **2018**, *57* (6), 1790–1802. <https://doi.org/10.1021/acs.iecr.7b04836>.
- (23) Hines, M. A.; Scholes, G. D. Colloidal PbS Nanocrystals with Size-Tunable Near-Infrared Emission: Observation of Post-Synthesis Self-Narrowing of the Particle Size Distribution. *Adv. Mater.* **2003**, *15* (21), 1844–1849. <https://doi.org/10.1002/adma.200305395>.
- (24) Yu, J.; Shendre, S.; Koh, W.; Liu, B.; Li, M.; Hou, S.; Hettiarachchi, C.; Delikanli, S.; Hernández-Martínez, P.; Birowosuto, M. D.; Wang, H.; Sum, T.; Demir, H. V.; Dang, C. Electrically Control Amplified Spontaneous Emission in Colloidal Quantum Dots. *Sci. Adv.* **2019**, *5* (10), eaav3140. <https://doi.org/10.1126/sciadv.aav3140>.
- (25) Micic, O. I.; Curtis, C. J.; Jones, K. M.; Sprague, J. R.; Nozik, A. J. Synthesis and Characterization of InP Quantum Dots. *J. Phys. Chem.* **1994**, *98* (19), 4966–4969. <https://doi.org/10.1021/j100070a004>.
- (26) Protesescu, L.; Yakunin, S.; Bodnarchuk, M. I.; Krieg, F.; Caputo, R.; Hendon, C. H.; Yang, R. X.; Walsh, A.; Kovalenko, M. V. Nanocrystals of Cesium Lead Halide Perovskites (CsPbX₃, X = Cl, Br, and I): Novel Optoelectronic Materials Showing Bright Emission with Wide Color Gamut. *Nano Lett.* **2015**, *15* (6), 3692–3696. <https://doi.org/10.1021/nl5048779>.
- (27) Cao, Y. C.; Wang, J. One-Pot Synthesis of High-Quality Zinc-Blende CdS Nanocrystals. *J. Am. Chem.*

- Soc.* **2004**, *126*(44), 14336–14337. <https://doi.org/10.1021/ja0459678>.
- (28) Kwon, S. G.; Piao, Y.; Park, J.; Angappane, S.; Jo, Y.; Hwang, N.-M.; Park, J.-G.; Hyeon, T. Kinetics of Monodisperse Iron Oxide Nanocrystal Formation by “Heating-Up” Process. *J. Am. Chem. Soc.* **2007**, *129*(41), 12571–12584. <https://doi.org/10.1021/ja074633q>.
- (29) Yang, X.; Zhao, D.; Leck, K. S.; Tan, S. T.; Tang, Y. X.; Zhao, J.; Demir, H. V.; Sun, X. W. Full Visible Range Covering InP/ZnS Nanocrystals with High Photometric Performance and Their Application to White Quantum Dot Light-Emitting Diodes. *Advanced Materials* **2012**, *24*(30), 4180–4185. <https://doi.org/10.1002/adma.201104990>.
- (30) Coe-Sullivan, S.; Steckel, J. S.; Woo, W.-K.; Bawendi, M. G.; Bulović, V. Large-Area Ordered Quantum-Dot Monolayers via Phase Separation During Spin-Casting. *Adv. Funct. Mater.* **2005**, *15*(7), 1117–1124. <https://doi.org/10.1002/adfm.200400468>.
- (31) Ramírez, H. Y.; Flórez, J.; Camacho, Á. S. Efficient Control of Coulomb Enhanced Second Harmonic Generation from Excitonic Transitions in Quantum Dot Ensembles. *Phys. Chem. Chem. Phys.* **2015**, *17*(37), 23938–23946. <https://doi.org/10.1039/C5CP03349G>.
- (32) Zhang, H.; Chen, S.; Sun, X. W. Efficient Red/Green/Blue Tandem Quantum-Dot Light-Emitting Diodes with External Quantum Efficiency Exceeding 21%. *ACS Nano* **2018**, *12*(1), 697–704. <https://doi.org/10.1021/acsnano.7b07867>.
- (33) Zou, Y.; Ban, M.; Cui, W.; Huang, Q.; Wu, C.; Liu, J.; Wu, H.; Song, T.; Sun, B. A General Solvent Selection Strategy for Solution Processed Quantum Dots Targeting High Performance Light-Emitting Diode. *Advanced Functional Materials* **2017**, *27*(1), 1603325. <https://doi.org/10.1002/adfm.201603325>.
- (34) Shi, Y.-L.; Liang, F.; Hu, Y.; Wang, X.-D.; Wang, Z.-K.; Liao, L.-S. High-Efficiency Quantum Dot Light-Emitting Diodes Employing Lithium Salt Doped Poly(9-Vinylcarbazole) as a Hole-Transporting Layer. *J. Mater. Chem. C* **2017**, *5*(22), 5372–5377. <https://doi.org/10.1039/C7TC00449D>.
- (35) Shen, H.; Lin, Q.; Cao, W.; Yang, C.; Shewmon, N. T.; Wang, H.; Niu, J.; Li, L. S.; Xue, J. Efficient and Long-Lifetime Full-Color Light-Emitting Diodes Using High Luminescence Quantum Yield Thick-Shell Quantum Dots. *Nanoscale* **2017**, *9*(36), 13583–13591. <https://doi.org/10.1039/C7NR04953F>.
- (36) Li, Z.; Hu, Y.; Shen, H.; Lin, Q.; Wang, L.; Wang, H.; Zhao, W.; Li, L. S. Efficient and Long-Life Green Light-Emitting Diodes Comprising Tridentate Thiol Capped Quantum Dots: Efficient and Long-Life Green Light-Emitting Diodes... *Laser & Photonics Reviews* **2017**, *11*(1), 1600227. <https://doi.org/10.1002/lpor.201600227>.
- (37) Kang, Y.; Song, Z.; Jiang, X.; Yin, X.; Fang, L.; Gao, J.; Su, Y.; Zhao, F. Quantum Dots for Wide Color Gamut Displays from Photoluminescence to Electroluminescence. *Nanoscale Res Lett* **2017**, *12*(1), 154. <https://doi.org/10.1186/s11671-017-1907-1>.
- (38) Im, Y.; Byun, S. Y.; Kim, J. H.; Lee, D. R.; Oh, C. S.; Yook, K. S.; Lee, J. Y. Recent Progress in High-Efficiency Blue-Light-Emitting Materials for Organic Light-Emitting Diodes. *Adv. Funct. Mater.* **2017**,

- 27(13), 1603007. <https://doi.org/10.1002/adfm.201603007>.
- (39) Ding, K.; Chen, H.; Fan, L.; Wang, B.; Huang, Z.; Zhuang, S.; Hu, B.; Wang, L. Polyethylenimine Insulativity-Dominant Charge-Injection Balance for Highly Efficient Inverted Quantum Dot Light-Emitting Diodes. *ACS Appl. Mater. Interfaces* **2017**, *9* (23), 20231–20238. <https://doi.org/10.1021/acsami.7b04662>.
- (40) Wang, L.; Chen, T.; Lin, Q.; Shen, H.; Wang, A.; Wang, H.; Li, C.; Li, L. S. High-Performance Azure Blue Quantum Dot Light-Emitting Diodes via Doping PVK in Emitting Layer. *Organic Electronics* **2016**, *37*, 280–286. <https://doi.org/10.1016/j.orgel.2016.06.032>.
- (41) Peng, H.; Jiang, Y.; Chen, S. Efficient Vacuum-Free-Processed Quantum Dot Light-Emitting Diodes with Printable Liquid Metal Cathodes. *Nanoscale* **2016**, *8* (41), 17765–17773. <https://doi.org/10.1039/C6NR05181B>.
- (42) Kim, H.-M.; Geng, D.; Kim, J.; Hwang, E.; Jang, J. Metal-Oxide Stacked Electron Transport Layer for Highly Efficient Inverted Quantum-Dot Light Emitting Diodes. *ACS Appl. Mater. Interfaces* **2016**, *8* (42), 28727–28736. <https://doi.org/10.1021/acsami.6b10314>.
- (43) Yang, Y.; Zheng, Y.; Cao, W.; Titov, A.; Hyvonen, J.; Manders, J. R.; Xue, J.; Holloway, P. H.; Qian, L. High-Efficiency Light-Emitting Devices Based on Quantum Dots with Tailored Nanostructures. *Nature Photon* **2015**, *9*(4), 259–266. <https://doi.org/10.1038/nphoton.2015.36>.
- (44) Shen, H.; Cao, W.; Shewmon, N. T.; Yang, C.; Li, L. S.; Xue, J. High-Efficiency, Low Turn-on Voltage Blue-Violet Quantum-Dot-Based Light-Emitting Diodes. *Nano Lett.* **2015**, *15* (2), 1211–1216. <https://doi.org/10.1021/nl504328f>.
- (45) Manders, J. R.; Qian, L.; Titov, A.; Hyvonen, J.; Tokarz-Scott, J.; Acharya, K. P.; Yang, Y.; Cao, W.; Zheng, Y.; Xue, J.; Holloway, P. H. High Efficiency and Ultra-Wide Color Gamut Quantum Dot LEDs for next Generation Displays: Quantum Dot LEDs for next Generation Displays. *Jnl Soc Info Display* **2015**, *23* (11), 523–528. <https://doi.org/10.1002/jsid.393>.
- (46) Kim, H.-M.; Kim, J.; Lee, J.; Jang, J. Inverted Quantum-Dot Light Emitting Diode Using Solution Processed p -Type WO_x Doped PEDOT:PSS and Li Doped ZnO Charge Generation Layer. *ACS Appl. Mater. Interfaces* **2015**, *7* (44), 24592–24600. <https://doi.org/10.1021/acsami.5b06505>.
- (47) Yang, X.; Mutlugun, E.; Dang, C.; Dev, K.; Gao, Y.; Tan, S. T.; Sun, X. W.; Demir, H. V. Highly Flexible, Electrically Driven, Top-Emitting, Quantum Dot Light-Emitting Stickers. *ACS Nano* **2014**, *8*(8), 8224–8231. <https://doi.org/10.1021/nn502588k>.
- (48) Shen, H.; Bai, X.; Wang, A.; Wang, H.; Qian, L.; Yang, Y.; Titov, A.; Hyvonen, J.; Zheng, Y.; Li, L. S. High-Efficient Deep-Blue Light-Emitting Diodes by Using High Quality $\text{Zn}_{1-x}\text{Cd}_x\text{S}/\text{ZnS}$ Core/Shell Quantum Dots. *Adv. Funct. Mater.* **2014**, *24* (16), 2367–2373. <https://doi.org/10.1002/adfm.201302964>.
- (49) Lee, K.-H.; Lee, J.-H.; Kang, H.-D.; Park, B.; Kwon, Y.; Ko, H.; Lee, C.; Lee, J.; Yang, H. Over 40 Cd/A Efficient Green Quantum Dot Electroluminescent Device Comprising Uniquely Large-Sized Quantum

- Dots. *ACS Nano* **2014**, *8* (5), 4893–4901. <https://doi.org/10.1021/nn500852g>.
- (50) Dai, X.; Zhang, Z.; Jin, Y.; Niu, Y.; Cao, H.; Liang, X.; Chen, L.; Wang, J.; Peng, X. Solution-Processed, High-Performance Light-Emitting Diodes Based on Quantum Dots. *Nature* **2014**, *515* (7525), 96–99. <https://doi.org/10.1038/nature13829>.
- (51) Shen, H.; Lin, Q.; Wang, H.; Qian, L.; Yang, Y.; Titov, A.; Hyvonen, J.; Zheng, Y.; Li, L. S. Efficient and Bright Colloidal Quantum Dot Light-Emitting Diodes via Controlling the Shell Thickness of Quantum Dots. *ACS Appl. Mater. Interfaces* **2013**, *5* (22), 12011–12016. <https://doi.org/10.1021/am4038068>.
- (52) Mashford, B. S.; Stevenson, M.; Popovic, Z.; Hamilton, C.; Zhou, Z.; Breen, C.; Steckel, J.; Bulovic, V.; Bawendi, M.; Coe-Sullivan, S.; Kazlas, P. T. High-Efficiency Quantum-Dot Light-Emitting Devices with Enhanced Charge Injection. *Nature Photon* **2013**, *7* (5), 407–412. <https://doi.org/10.1038/nphoton.2013.70>.
- (53) Lee, K.-H.; Lee, J.-H.; Song, W.-S.; Ko, H.; Lee, C.; Lee, J.-H.; Yang, H. Highly Efficient, Color-Pure, Color-Stable Blue Quantum Dot Light-Emitting Devices. *ACS Nano* **2013**, *7* (8), 7295–7302. <https://doi.org/10.1021/nn402870e>.
- (54) Leck, K. S.; Divayana, Y.; Zhao, D.; Yang, X.; Abiyasa, A. P.; Mutlugun, E.; Gao, Y.; Liu, S.; Tan, S. T.; Sun, X. W.; Demir, H. V. Quantum Dot Light-Emitting Diode with Quantum Dots Inside the Hole Transporting Layers. *ACS Appl. Mater. Interfaces* **2013**, *5* (14), 6535–6540. <https://doi.org/10.1021/am400903c>.
- (55) Bae, W. K.; Park, Y.-S.; Lim, J.; Lee, D.; Padilha, L. A.; McDaniel, H.; Robel, I.; Lee, C.; Pietryga, J. M.; Klimov, V. I. Controlling the Influence of Auger Recombination on the Performance of Quantum-Dot Light-Emitting Diodes. *Nat Commun* **2013**, *4* (1), 2661. <https://doi.org/10.1038/ncomms3661>.
- (56) Kwak, J.; Bae, W. K.; Lee, D.; Park, I.; Lim, J.; Park, M.; Cho, H.; Woo, H.; Yoon, D. Y.; Char, K.; Lee, S.; Lee, C. Bright and Efficient Full-Color Colloidal Quantum Dot Light-Emitting Diodes Using an Inverted Device Structure. *Nano Lett.* **2012**, *12* (5), 2362–2366. <https://doi.org/10.1021/nl3003254>.
- (57) Qian, L.; Zheng, Y.; Xue, J.; Holloway, P. H. Stable and Efficient Quantum-Dot Light-Emitting Diodes Based on Solution-Processed Multilayer Structures. *Nature Photon* **2011**, *5* (9), 543–548. <https://doi.org/10.1038/nphoton.2011.171>.
- (58) Cho, K.-S.; Lee, E. K.; Joo, W.-J.; Jang, E.; Kim, T.-H.; Lee, S. J.; Kwon, S.-J.; Han, J. Y.; Kim, B.-K.; Choi, B. L.; Kim, J. M. High-Performance Crosslinked Colloidal Quantum-Dot Light-Emitting Diodes. *Nature Photon* **2009**, *3* (6), 341–345. <https://doi.org/10.1038/nphoton.2009.92>.
- (59) Anikeeva, P. O.; Halpert, J. E.; Bawendi, M. G.; Bulović, V. Quantum Dot Light-Emitting Devices with Electroluminescence Tunable over the Entire Visible Spectrum. *Nano Lett.* **2009**, *9* (7), 2532–2536. <https://doi.org/10.1021/nl9002969>.
- (60) Zhao, J.; Bardecker, J. A.; Munro, A. M.; Liu, M. S.; Niu, Y.; Ding, I.-K.; Luo, J.; Chen, B.; Jen, A. K.-Y.; Ginger, D. S. Efficient CdSe/CdS Quantum Dot Light-Emitting Diodes Using a Thermally Polymerized Hole Transport Layer. *Nano Lett.* **2006**, *6* (3), 463–467. <https://doi.org/10.1021/nl052417e>.

- (61) Steckel, J. S.; Zimmer, J. P.; Coe-Sullivan, S.; Stott, N. E.; Bulović, V.; Bawendi, M. G. Blue Luminescence from (CdS)ZnS Core-Shell Nanocrystals. *Angew. Chem. Int. Ed.* **2004**, *43* (16), 2154–2158. <https://doi.org/10.1002/anie.200453728>.
- (62) Coe, S.; Woo, W.-K.; Bawendi, M.; Bulović, V. Electroluminescence from Single Monolayers of Nanocrystals in Molecular Organic Devices. *Nature* **2002**, *420* (6917), 800–803. <https://doi.org/10.1038/nature01217>.
- (63) Schlamp, M. C.; Peng, X.; Alivisatos, A. P. Improved Efficiencies in Light Emitting Diodes Made with CdSe(CdS) Core/Shell Type Nanocrystals and a Semiconducting Polymer. *Journal of Applied Physics* **1997**, *82* (11), 5837–5842. <https://doi.org/10.1063/1.366452>.
- (64) Colvin, V. L.; Schlamp, M. C.; Alivisatos, A. P. Light-Emitting Diodes Made from Cadmium Selenide Nanocrystals and a Semiconducting Polymer. *Nature* **1994**, *370* (6488), 354–357. <https://doi.org/10.1038/370354a0>.
- (65) Rogalski, A.; Antoszewski, J.; Faraone, L. Third-Generation Infrared Photodetector Arrays. *Journal of Applied Physics* **2009**, *105* (9), 091101. <https://doi.org/10.1063/1.3099572>.
- (66) Haugan, H. J.; Elhamri, S.; Szmulowicz, F.; Ullrich, B.; Brown, G. J.; Mitchel, W. C. Study of Residual Background Carriers in Midinfrared InAs/GaSb Superlattices for Uncooled Detector Operation. *Appl. Phys. Lett.* **2008**, *92* (7), 071102. <https://doi.org/10.1063/1.2884264>.
- (67) Michel, J.; Liu, J.; Kimerling, L. C. High-Performance Ge-on-Si Photodetectors. *Nature Photon* **2010**, *4* (8), 527–534. <https://doi.org/10.1038/nphoton.2010.157>.
- (68) Dai, Y.; Wang, X.; Peng, W.; Xu, C.; Wu, C.; Dong, K.; Liu, R.; Wang, Z. L. Self - Powered Si/CdS Flexible Photodetector with Broadband Response from 325 to 1550 Nm Based on Pyro - phototronic Effect: An Approach for Photosensing below Bandgap Energy. *Adv. Mater.* **2018**, *30* (9), 1705893. <https://doi.org/10.1002/adma.201705893>.
- (69) Zhang, H.; Zhang, X.; Liu, C.; Lee, S.-T.; Jie, J. High-Responsivity, High-Detectivity, Ultrafast Topological Insulator Bi₂Se₃/Silicon Heterostructure Broadband Photodetectors. *ACS Nano* **2016**, *10* (5), 5113–5122. <https://doi.org/10.1021/acsnano.6b00272>.
- (70) Ozel, T.; Sari, E.; Nizamoglu, S.; Demir, H. V. Violet to Deep-Ultraviolet InGaN/GaN and GaN/AlGaN Quantum Structures for UV Electroabsorption Modulators. *Journal of Applied Physics* **2007**, *102* (11), 113101. <https://doi.org/10.1063/1.2817954>.
- (71) Asif Khan, M.; Shatalov, M.; Maruska, H. P.; Wang, H. M.; Kuokstis, E. III-Nitride UV Devices. *Jpn. J. Appl. Phys.* **2005**, *44* (10), 7191–7206. <https://doi.org/10.1143/JJAP.44.7191>.
- (72) Zhuo, R.; Wang, Y.; Wu, D.; Lou, Z.; Shi, Z.; Xu, T.; Xu, J.; Tian, Y.; Li, X. High-Performance Self-Powered Deep Ultraviolet Photodetector Based on MoS₂/GaN p-n Heterojunction. *J. Mater. Chem. C* **2018**, *6* (2), 299–303. <https://doi.org/10.1039/C7TC04754A>.
- (73) Xu, W.; Guo, Y.; Zhang, X.; Zheng, L.; Zhu, T.; Zhao, D.; Hu, W.; Gong, X. Room - Temperature - Operated Ultrasensitive Broadband Photodetectors by Perovskite Incorporated with Conjugated

- Polymer and Single - Wall Carbon Nanotubes. *Adv. Funct. Mater.* **2018**, *28* (7), 1705541. <https://doi.org/10.1002/adfm.201705541>.
- (74) Hendriks, K. H.; Li, W.; Wienk, M. M.; Janssen, R. A. J. Small-Bandgap Semiconducting Polymers with High Near-Infrared Photoresponse. *J. Am. Chem. Soc.* **2014**, *136* (34), 12130–12136. <https://doi.org/10.1021/ja506265h>.
- (75) Bai, F.; Qi, J.; Li, F.; Fang, Y.; Han, W.; Wu, H.; Zhang, Y. A High-Performance Self-Powered Photodetector Based on Monolayer MoS₂/Perovskite Heterostructures. *Adv. Mater. Interfaces* **2018**, *5* (6), 1701275. <https://doi.org/10.1002/admi.201701275>.
- (76) Fang, Y.; Huang, J. Resolving Weak Light of Sub-Picowatt per Square Centimeter by Hybrid Perovskite Photodetectors Enabled by Noise Reduction. *Adv. Mater.* **2015**, *27* (17), 2804–2810. <https://doi.org/10.1002/adma.201500099>.
- (77) Hu, X.; Zhang, X.; Liang, L.; Bao, J.; Li, S.; Yang, W.; Xie, Y. High-Performance Flexible Broadband Photodetector Based on Organolead Halide Perovskite. *Adv. Funct. Mater.* **2014**, *24* (46), 7373–7380. <https://doi.org/10.1002/adfm.201402020>.
- (78) Li, Q.; Guo, Y.; Liu, Y. Exploration of Near-Infrared Organic Photodetectors. *Chem. Mater.* **2019**, *31* (17), 6359–6379. <https://doi.org/10.1021/acs.chemmater.9b00966>.
- (79) Xu, K.; Zhou, W.; Ning, Z. Integrated Structure and Device Engineering for High Performance and Scalable Quantum Dot Infrared Photodetectors. *Small* **2020**, *16* (47), 2003397. <https://doi.org/10.1002/sml.202003397>.
- (80) Kagan, C. R.; Lifshitz, E.; Sargent, E. H.; Talapin, D. V. Building Devices from Colloidal Quantum Dots. *Science* **2016**, *353* (6302), aac5523. <https://doi.org/10.1126/science.aac5523>.
- (81) Tang, J.; Kemp, K. W.; Hoogland, S.; Jeong, K. S.; Liu, H.; Levina, L.; Furukawa, M.; Wang, X.; Debnath, R.; Cha, D.; Chou, K. W.; Fischer, A.; Amassian, A.; Asbury, J. B.; Sargent, E. H. Colloidal-Quantum-Dot Photovoltaics Using Atomic-Ligand Passivation. *Nature Mater* **2011**, *10* (10), 765–771. <https://doi.org/10.1038/nmat3118>.
- (82) Chuang, C.-H. M.; Brown, P. R.; Bulović, V.; Bawendi, M. G. Improved Performance and Stability in Quantum Dot Solar Cells through Band Alignment Engineering. *Nature Mater* **2014**, *13* (8), 796–801. <https://doi.org/10.1038/nmat3984>.
- (83) Carey, G. H.; Levina, L.; Comin, R.; Voznyy, O.; Sargent, E. H. Record Charge Carrier Diffusion Length in Colloidal Quantum Dot Solids via Mutual Dot-To-Dot Surface Passivation. *Adv. Mater.* **2015**, *27* (21), 3325–3330. <https://doi.org/10.1002/adma.201405782>.
- (84) Choi, A. O.; Brown, S. E.; Szyf, M.; Maysinger, D. Quantum Dot-Induced Epigenetic and Genotoxic Changes in Human Breast Cancer Cells. *J Mol Med.* **2008**, *86* (3), 291–302. <https://doi.org/10.1007/s00109-007-0274-2>.
- (85) Wang, A.; Shen, H.; Zang, S.; Lin, Q.; Wang, H.; Qian, L.; Niu, J.; Li, L. S. Bright, Efficient, and Color-Stable Violet ZnSe-Based Quantum Dot Light-Emitting Diodes. **2015**, *9*.

- (86) Won, Y.-H.; Cho, O.; Kim, T.; Chung, D.-Y.; Kim, T.; Chung, H.; Jang, H.; Lee, J.; Kim, D.; Jang, E. Highly Efficient and Stable InP/ZnSe/ZnS Quantum Dot Light-Emitting Diodes. *Nature* **2019**, *575* (7784), 634–638. <https://doi.org/10.1038/s41586-019-1771-5>.
- (87) Chao, W.-C.; Chiang, T.-H.; Liu, Y.-C.; Huang, Z.-X.; Liao, C.-C.; Chu, C.-H.; Wang, C.-H.; Tseng, H.-W.; Hung, W.-Y.; Chou, P.-T. High Efficiency Green InP Quantum Dot Light-Emitting Diodes by Balancing Electron and Hole Mobility. *Commun Mater* **2021**, *2* (1), 96. <https://doi.org/10.1038/s43246-021-00203-5>.
- (88) Voigt, D.; Bredol, M.; Gonabadi, A. A General Strategy for CuInS₂ Based Quantum Dots with Adjustable Surface Chemistry. *Optical Materials* **2021**, *115*, 110994. <https://doi.org/10.1016/j.optmat.2021.110994>.
- (89) Jurbergs, D.; Rogojina, E.; Mangolini, L.; Kortshagen, U. Silicon Nanocrystals with Ensemble Quantum Yields Exceeding 60%. *Appl. Phys. Lett.* **2006**, *88* (23), 233116. <https://doi.org/10.1063/1.2210788>.
- (90) Wijaya, H.; Darwan, D.; Zhao, X.; Ong, E. W. Y.; Lim, K. R. G.; Wang, T.; Lim, L. J.; Khoo, K. H.; Tan, Z. Efficient Near - Infrared Light - Emitting Diodes Based on In(Zn)As–In(Zn)P–GaP–ZnS Quantum Dots. *Adv. Funct. Mater.* **2020**, *30* (4), 1906483. <https://doi.org/10.1002/adfm.201906483>.
- (91) Bai, Z.; Ji, W.; Han, D.; Chen, L.; Chen, B.; Shen, H.; Zou, B.; Zhong, H. Hydroxyl-Terminated CuInS₂ Based Quantum Dots: Toward Efficient and Bright Light Emitting Diodes. *Chem. Mater.* **2016**, *28* (4), 1085–1091. <https://doi.org/10.1021/acs.chemmater.5b04480>.
- (92) Yamada, H.; Saitoh, N.; Ghosh, B.; Masuda, Y.; Yoshizawa, N.; Shirahata, N. Improved Brightness and Color Tunability of Solution-Processed Silicon Quantum Dot Light-Emitting Diodes. *J. Phys. Chem. C* **2020**, *124* (42), 23333–23342. <https://doi.org/10.1021/acs.jpcc.0c06672>.
- (93) Chiang, Y.-H.; Lin, K.-Y.; Chen, Y.-H.; Waki, K.; Abate, M. A.; Jiang, J.-C.; Chang, J.-Y. Aqueous Solution-Processed off-Stoichiometric Cu–In–S QDs and Their Application in Quantum Dot-Sensitized Solar Cells. *J. Mater. Chem. A* **2018**, *6* (20), 9629–9641. <https://doi.org/10.1039/C8TA01064A>.
- (94) Leemans, J.; Pejović, V.; Georgitzikis, E.; Minjauw, M.; Siddik, A. B.; Deng, Y.; Kuang, Y.; Roelkens, G.; Detavernier, C.; Lieberman, I.; Malinowski, P. E.; Cheyns, D.; Hens, Z. Colloidal III–V Quantum Dot Photodiodes for Short - Wave Infrared Photodetection. *Advanced Science* **2022**, *9* (17), 2200844. <https://doi.org/10.1002/advs.202200844>.
- (95) Pietryga, J. M.; Park, Y.-S.; Lim, J.; Fidler, A. F.; Bae, W. K.; Brovelli, S.; Klimov, V. I. Spectroscopic and Device Aspects of Nanocrystal Quantum Dots. *Chem. Rev.* **2016**, *116* (18), 10513–10622. <https://doi.org/10.1021/acs.chemrev.6b00169>.
- (96) Healy, M. D.; Laibinis, P. E.; Stupik, P. D.; Barron, A. R. The Reaction of Indium(III) Chloride with Tris(trimethylsilyl)Phosphine: A Novel Route to Indium Phosphide. *J. Chem. Soc., Chem. No. 6*, 359–360. <https://doi.org/10.1039/c39890000359>.
- (97) R. Heath, J. Covalency in Semiconductor Quantum Dots. *Chem. Soc. Rev.* **1998**, *27* (1), 65. <https://doi.org/10.1039/a827065z>.

- (98) Li, L.; Reiss, P. One-Pot Synthesis of Highly Luminescent InP/ZnS Nanocrystals without Precursor Injection. *Journal of the American Chemical Society* **2008**, *130* (35), 11588–11589. <https://doi.org/10.1021/ja803687e>.
- (99) Kim, Y.; Ham, S.; Jang, H.; Min, J. H.; Chung, H.; Lee, J.; Kim, D.; Jang, E. Bright and Uniform Green Light Emitting InP/ZnSe/ZnS Quantum Dots for Wide Color Gamut Displays. *ACS Appl. Nano Mater.* **2019**, *2* (3), 1496–1504. <https://doi.org/10.1021/acsanm.8b02063>.
- (100) Stein, J. L.; Mader, E. A.; Cossairt, B. M. Luminescent InP Quantum Dots with Tunable Emission by Post-Synthetic Modification with Lewis Acids. *The Journal of Physical Chemistry Letters* **2016**, *7* (7), 1315–1320. <https://doi.org/10.1021/acs.jpcllett.6b00177>.
- (101) Ippen, C.; Greco, T.; Wedel, A. InP/ZnSe/ZnS: A Novel Multishell System for InP Quantum Dots for Improved Luminescence Efficiency and Its Application in a Light-Emitting Device. *Journal of Information Display* **2012**, *13* (2), 91–95. <https://doi.org/10.1080/15980316.2012.683537>.
- (102) Lim, J.; Bae, W. K.; Lee, D.; Nam, M. K.; Jung, J.; Lee, C.; Char, K.; Lee, S. InP@ZnSeS, Core@Composition Gradient Shell Quantum Dots with Enhanced Stability. *Chemistry of Materials* **2011**, *23* (20), 4459–4463. <https://doi.org/10.1021/cm201550w>.
- (103) Kim, S.; Kim, T.; Kang, M.; Kwak, S. K.; Yoo, T. W.; Park, L. S.; Yang, I.; Hwang, S.; Lee, J. E.; Kim, S. K.; Kim, S.-W. Highly Luminescent InP/GaP/ZnS Nanocrystals and Their Application to White Light-Emitting Diodes. *J. Am. Chem. Soc.* **2012**, *134* (8), 3804–3809. <https://doi.org/10.1021/ja210211z>.
- (104) Kim, S.; Fisher, B.; Eisler, H.-J.; Bawendi, M. Type-II Quantum Dots: CdTe/CdSe(Core/Shell) and CdSe/ZnTe(Core/Shell) Heterostructures. *J. Am. Chem. Soc.* **2003**, *125* (38), 11466–11467. <https://doi.org/10.1021/ja0361749>.
- (105) Wei, S.-H.; Zunger, A. Calculated Natural Band Offsets of All II–VI and III–V Semiconductors: Chemical Trends and the Role of Cation *d* Orbitals. *Appl. Phys. Lett.* **1998**, *72* (16), 2011–2013. <https://doi.org/10.1063/1.121249>.
- (106) Reiss, P.; Protière, M.; Li, L. Core/Shell Semiconductor Nanocrystals. *Small* **2009**, *5* (2), 154–168. <https://doi.org/10.1002/sml.200800841>.
- (107) Chen, X.; Lou, Y.; Samia, A. C.; Burda, C. Coherency Strain Effects on the Optical Response of Core/Shell Heteronanostructures. *Nano Lett.* **2003**, *3* (6), 799–803. <https://doi.org/10.1021/nl034243b>.
- (108) Smith, A. M.; Mohs, A. M.; Nie, S. Tuning the Optical and Electronic Properties of Colloidal Nanocrystals by Lattice Strain. *Nature Nanotech* **2009**, *4* (1), 56–63. <https://doi.org/10.1038/nnano.2008.360>.
- (109) Gong, K.; Kelley, D. F. Lattice Strain Limit for Uniform Shell Deposition in Zincblende CdSe/CdS Quantum Dots. *J. Phys. Chem. Lett.* **2015**, *6* (9), 1559–1562. <https://doi.org/10.1021/acs.jpcllett.5b00566>.
- (110) Narayanaswamy, A.; Feiner, L. F.; Meijerink, A.; van der Zaag, P. J. The Effect of Temperature

- and Dot Size on the Spectral Properties of Colloidal InP/ZnS Core–Shell Quantum Dots. *ACS Nano* **2009**, *3* (9), 2539–2546. <https://doi.org/10.1021/nn9004507>.
- (111) Valerini, D.; Cretí, A.; Lomascolo, M.; Manna, L.; Cingolani, R.; Anni, M. Temperature Dependence of the Photoluminescence Properties of Colloidal CdSe / ZnS Core/Shell Quantum Dots Embedded in a Polystyrene Matrix. *Phys. Rev. B* **2005**, *71* (23), 235409. <https://doi.org/10.1103/PhysRevB.71.235409>.
- (112) Chon, B.; Bang, J.; Park, J.; Jeong, C.; Choi, J. H.; Lee, J.-B.; Joo, T.; Kim, S. Unique Temperature Dependence and Blinking Behavior of CdTe/CdSe (Core/Shell) Type-II Quantum Dots. *J. Phys. Chem. C* **2011**, *115* (2), 436–442. <https://doi.org/10.1021/jp109229u>.
- (113) Shirahata, N.; Nakamura, J.; Inoue, J.; Ghosh, B.; Nemoto, K.; Nemoto, Y.; Takeguchi, M.; Masuda, Y.; Tanaka, M.; Ozin, G. A. Emerging Atomic Energy Levels in Zero-Dimensional Silicon Quantum Dots. *Nano Lett.* **2020**, *20* (3), 1491–1498. <https://doi.org/10.1021/acs.nanolett.9b03157>.
- (114) Ji, C.; Zhang, Y.; Zhang, T.; Liu, W.; Zhang, X.; Shen, H.; Wang, Y.; Gao, W.; Wang, Y.; Zhao, J.; Yu, W. W. Temperature-Dependent Photoluminescence of Ag₂Se Quantum Dots. *J. Phys. Chem. C* **2015**, *119* (24), 13841–13846. <https://doi.org/10.1021/acs.jpcc.5b01030>.
- (115) Varshni, Y. P. TEMPERATURE DEPENDENCE OF THE ENERGY GAP IN SEMICONDUCTORS. *Physica (Amsterdam)* **1967**, *34* (1), 149–154. [https://doi.org/doi.org/10.1016/0031-8914\(67\)90062-6](https://doi.org/doi.org/10.1016/0031-8914(67)90062-6).
- (116) Ghosh, B.; Takeguchi, M.; Nakamura, J.; Nemoto, Y.; Hamaoka, T.; Chandra, S.; Shirahata, N. Origin of the Photoluminescence Quantum Yields Enhanced by Alkane-Termination of Freestanding Silicon Nanocrystals: Temperature-Dependence of Optical Properties. *Sci Rep* **2016**, *6* (1), 36951. <https://doi.org/10.1038/srep36951>.
- (117) O'Donnell, K. P.; Chen, X. Temperature Dependence of Semiconductor Band Gaps. *Appl. Phys. Lett.* **1991**, *58* (25), 2924–2926. <https://doi.org/10.1063/1.104723>.
- (118) Seong, M. J.; Mičić, O. I.; Nozik, A. J.; Mascarenhas, A.; Cheong, H. M. Size-Dependent Raman Study of InP Quantum Dots. *Appl. Phys. Lett.* **2003**, *82* (2), 185–187. <https://doi.org/10.1063/1.1535272>.
- (119) Narayanaswamy, A.; Feiner, L. F.; van der Zaag, P. J. Temperature Dependence of the Photoluminescence of InP/ZnS Quantum Dots. *J. Phys. Chem. C* **2008**, *112* (17), 6775–6780. <https://doi.org/10.1021/jp800339m>.
- (120) Cheng, O. H.-C.; Qiao, T.; Sheldon, M.; Son, D. H. Size- and Temperature-Dependent Photoluminescence Spectra of Strongly Confined CsPbBr₃ Quantum Dots. *Nanoscale* **2020**, *12* (24), 13113–13118. <https://doi.org/10.1039/D0NR02711A>.
- (121) Dabbousi, B. O.; Rodriguez-Viejo, J.; Mikulec, F. V.; Heine, J. R.; Mattoussi, H.; Ober, R.; Jensen, K. F.; Bawendi, M. G. (CdSe)ZnS Core–Shell Quantum Dots: Synthesis and Characterization of a Size Series of Highly Luminescent Nanocrystallites. *J. Phys. Chem. B* **1997**, *101* (46), 9463–9475.

<https://doi.org/10.1021/jp971091y>.

- (122) Ji, B.; Panfil, Y. E.; Waiskopf, N.; Remennik, S.; Popov, I.; Banin, U. Strain-Controlled Shell Morphology on Quantum Rods. *Nat Commun* **2019**, *10* (1), 2. <https://doi.org/10.1038/s41467-018-07837-z>.

Chapter 2: Coherent InP/ZnS core / shell quantum dots with narrow-band green emissions

2.1 Introduction

A critical factor to efficiently convert the absorbed optical-energy into other useful forms such as photoluminescence (PL), electricity, or heat is to control the fate of the electron–hole (e–h) carriers or excitons generated in colloidal semiconductor nanocrystals (or quantum dots, QDs) via a sequential absorption of the photons under excited conditions.^{1–7} Eliminating the surface defects, which are responsible for nonradiative exciton recombination centers, is necessary to improve the PL performance.^{8–10} Typically, a core/shell structure of semiconductors is adopted to reduce the number of defects, including electron traps at the interface.¹¹ The core QD (e.g., indium phosphide, InP) is encapsulated by a shell of a different semiconductor whose bandgap encloses that of the core QD. The resultant core/shell heterostructure is referred to as a type-I band alignment. In this configuration, the excitons are spatially confined to the core and interactions with surface states are minimized, hindering their spread over the whole core/shell QD.^{12,13} The strengthened confinement improves the radiative recombination rate, which leads to a high PL quantum yield (PLQY).

Good examples of the type-I architecture are InP/ZnSe/ZnS core/shell/shell QDs, which are typical Cd-free materials. In the bulk state, when ZnS (lattice constant, $a_{\text{ZnS}} = 0.541$ nm) is directly deposited on InP ($a_{\text{InP}} = 0.587$ nm), the difference in the lattice constant between ZnS and InP, which corresponds to a 7.8% lattice mismatch, is sufficient to evoke defect formation at the heterogeneous core/shell interface because mitigating the mismatch by lattice strain is no longer thermodynamically favored. In this solution, the most versatile approach adopts ZnSe ($a_{\text{ZnSe}} = 0.566$ nm) as a shell material, which can build a graded core/shell interface due to the lower lattice mismatch ($\leq 3.5\%$) with InP, suppressing an

emerging defective interface. Consequently, PL performances, including a symmetric and a single-peak spectral feature, a high QY of almost unity, and a narrow spectral bandwidth (denoted by the full width at half maximum, FWHM) on the order of 35–45 nm, are enhanced.^{14–19} On the other hand, the PL spectra of these InP/ZnSe/ZnS core/shell/shell QDs are biased toward emission wavelengths between 650 nm (~1.91 eV) and 530 nm (~2.34 eV). Therefore, one of the key issues for the next generation of display technology is to expand the color gamut. The development of materials that emit light in the shorter wavelength range ($\lambda < 530$ nm, ~2.34 eV) including dark-green visible color is required. One possible reason for this contrast is that the widened bandgap for PL in the blue-green spectral region reduces the offset of the conduction band (and/or valence band) between the InP core and the ZnSe shell. Zhang reported that the lowest conduction band energy level of the ZnSe shell becomes lower than that of the green-emitting InP core QD. This situation induces partial leakage of the photogenerated carriers into the shell, causing carriers to be localized throughout the core/shell QD.²⁰ Consequently, there is a small redshift of the PL spectrum along with the spectral asymmetry due to emission tails. Their experimental results were supported by Jang et al. who calculated the change in the energy bandgap as a function of QD size using a theoretical model based on density functional theory (DFT).²¹ Their theoretical prediction indicated that a diameter of 2.5 nm, which corresponds to the size for green PL, is small enough that the charge carriers generated in InP can transit to the ZnSe shell because there is a low energy barrier at the heterogeneous core/shell interface. A similar observation has also been reported for core/shell QD systems of other semiconductors including CdSe/ZnS.¹¹

Several strategies could be applied to synthesize InP-based QDs that exhibit excellent PL performances in the blue-green spectral range. One strategy is multielement alloying for the core (e.g., $\text{In}_x\text{Zn}_y\text{P}$). This approach can mediate the lattice strain at the heterogeneous

interface, enhancing the PLQY.^{22,23} This strategy has inspired the concept of compositional alloying between Se and S or Mg and Zn for shell materials.^{19,20,24} Char et al. reported InP/ZnSeS/ZnS QD in which the composition-gradient multi-shell can mitigate the interfacial lattice distortion for an efficient green emission in the 500–520 nm (i.e., 2.48–2.38 eV) regime.²⁵ In this case, the PLQY was enhanced up to 70%, but the PL bandwidth was as broad as 50 nm. Pietra et al. controlled the compositional ratios of both the core (i.e., In_xZn_yP) and the shell (i.e., ZnSe_{1-z}S_z) because the lattice constant of the shell coincided with that (e.g., 0.539 nm) of the core QD. As expected, the PLQY was improved up to 60%, but the PL spectra were broad (FWHM = ~60–80 nm).²³ In addition, the selenium toxicity remains unresolved. In a system with a InP/GaP/ZnS core/shell/shell structure, the strain energy, which should be induced at the interface between the inner shell and the core, was alleviated by cation exchange.^{26,27} During the high-temperature synthesis for shell formation, Ga³⁺ ions diffuse into the core and are substituted for the In³⁺ ion for alloying. The resulting alloyed QD, in which the chemical composition is continuously graded to diminish the strain energy at the interface, exhibits a PLQY as high as 80%. However, their PL bands are still broader than 50 nm.²⁷ Thus, identifying a suitable shell material for the passivation of InP QDs, which endows both a high PLQY and a narrow PL band, remains a challenge, particularly in a short wavelength range.

Nie and co-workers proposed an interesting idea of using material strain to build a QD with a coherent core/shell structure.²⁸ In their work, CdTe ($a = 0.648$ nm) served as a core with a shell of a different kind elastically compressed, and the shell crystal is stretched by the lattice strain to have a lattice constant similar to that of the core. They discussed that the stress-induced changes in the lattice constant could be thermodynamically favored relative to the formation of defect trap sites at the core/shell interface to release the strain energy under

limited conditions. As expected, the coherent CdTe-based core/shell QDs allow for PL spectra with 60% PLQYs and bandwidths narrower than 50 nm.²⁸ This proposed concept has been broadened by replacing CdTe with CdSe.²⁹ Until now, it has been reported that InP as a core prevents the formation of a coherent core/shell structure.³⁰ This is due to a higher bulk modulus for InP and of semiconductor such as ZnS, ZnSe, or CdSe. These core/shell QDs tolerated both the epitaxial growth of the shell-layer and spherical core strain, altering the intrinsic interatomic distances of each crystal for the coherency from which the core crystal is ($B_u = 72.3$ GPa) than the strain-tolerated materials such as CdTe ($B_u = 42.4$ GPa) and CdSe ($B_u = 53.1$ GPa),^{28,31} suggesting that InP is less deformable even under isotropic compressive strain by shell encapsulation. However, we obtained the results of a series of structural and optical characterization studies which defy this common understanding. The present paper reports, for the first time, colloidal InP QDs in which their crystalline lattice is isotropically compressed by the growing ZnS shell to create a coherent core/shell structure with a single lattice constant. Optimized conditions for the synthesis provided nearly monodisperse core QDs working as a material's platform to discuss a critical thickness of the ZnS shell for such a coherent core/shell nanostructure. Moreover, the narrow size distribution of core QDs yielded a sharp first excitonic absorption peak with a valley depth of 0.51. The resulting coherent core/shell QDs exhibited excellent optical performances, including a spectral tunability in the deep-green wavelength range, a high PLQY of 70%, and a narrow PL bandwidth of 36 nm.

2.2 Experimental

Reagents and materials

Indium(iii) acetate [$\text{In}(\text{Ac})_3$, 99.99%, Aldrich], zinc acetate [$\text{Zn}(\text{Ac})_2$, 99.99%, Aldrich], zinc oxide (ZnO, 99.999%, Aldrich), 1-octadecene (ODE, 90%, Aldrich), sulfur (99.98%, Aldrich), oleic acid (OA, 90%, Aldrich), trioctylphosphine (TOP, 97%, Aldrich), 1-dodecanethiol (DDT, >98%, Aldrich), tris(trimethylsilyl)-phosphine [$(\text{TMS})_3\text{P}$, 98% Strem Chemicals], palmitic acid (PA, 98%, Tokyo Chemical Industry), and n-octylamine (OAm, 98%, Tokyo Chemical Industry) were used without further purification. The purity of argon gas was 99.999%. Using an oil rotary vacuum pump, the vacuum conditions of less than 60 Pa was used for degassing and argon gas purge.

Preparation of Zn-oleate

ZnO (2 mmol) and OA (8 mmol) were mixed with 10 mL of ODE in a 50 mL three-necked flask. The temperature was measured using a thermocouple inserted directly into the flask from the one branch pipe. The other branch pipe was capped with a silicone rubber septum for the injection of stainless-steel syringe needles. The flask was connected to a Schlenk line. At first, the system was purged five times with argon gas. The mixture was degassed at 120 °C for 2 h under vacuum conditions, and then the mixture was quickly heated in an argon flow to 290 °C and kept for about 1hr until the mixed solution got a transparent for yielding Zn-oleate. The solution was then cooled down to room temperature and stored in an argon-filled vial until the use.

Preparation of (TMS)₃P-TOP

(TMS)₃P (0.12 mmol) in hexane was dissolved in 1 mL of TOP at room temperature inside an argon-filled glovebox where the oxygen and water levels were continuously monitored to maintain both O₂ ≤ 1 ppm and H₂O ≤ 5 ppm. The mixture was gently stirred until becoming a uniform solution. This step was performed in the day before the synthesis of InP QD.

Synthesis of InP QDs

0.45 mmol of In(Ac)₃, 0.075 mmol of Zn(Ac)₂ and PA (0.5 mmol) were mixed with 6.3 mL of ODE in a 50 ml three-necked flask which is fixed to a Schlenk line with a reflux condenser. Degassing of the mixture was performed at 120 °C for 12 h under vacuum conditions. The degree of vacuum was controlled at 30 Pa which was measured using a capacitance manometer (ULVAC, Japan). The flask was filled with argon and cooled down to room temperature. The (TMS)₃P-TOP was quickly injected into the flask in an argon flow, heated to 40 °C under vacuum and kept for 10 min for the evaporation of hexane. Then, the flask was refilled with argon, heated to 300 °C within 7.5 min and kept for 10 min. After then, the flask was cooled down to room temperature, and stored in argon-filled vials.

Synthesis of InP/ZnS core/shell QDs

In a typical synthesis, 1 mL of the InP QD solution, 32 μL of DDT and 1 mL of Zn-oleate (0.2 mmol) were mixed with 2 mL of ODE in another 50 mL three-necked flask. The mixture was degassed at room temperature for 30 min under vacuum. After then, the flask was filled with argon, heated in an argon flow to 230 °C and kept for 20 min. By successively repeating the previous step, the shell of ZnS was thickened. In particular, one more layer of ZnS shell was coated by injection of a mixture of 32 μL of DDT and 1 mL of Zn-oleate at 230 °C,

followed by heating to 240 °C and solution was kept for 20 min. The reaction temperature was from 230 to 300 °C, in 10 °C increments. The span of time was commonly 20 min at every reaction temperature. At most we repeated the procedure of injection 7 times. After completing the formation of shell with predefined thickness, the solution was cooled down to 80 °C, and then acetone was added for centrifugation for 5 min at 10000 rpm. The InP/ZnS QDs precipitated were redispersed in 2 mL of hexane, and then 4 mL of methanol was added as a poor solvent for washing the QDs by centrifugation for 5 min at 6000 rpm. The supernatant was discarded to collect the QDs. The washing with hexane/methanol was repeated 5 times. Finally, the InP/ZnS QDs were redispersed in toluene and stored in argon-filled vials.

Characterization

X-ray powder diffraction patterns were measured on a MiniFlex 600 (Rigaku, Japan). Samples were measured at an angular step of 0.02° (time per step: 1 s per step) using CuK α (wavelength (λ) = 1.5418 Å) radiation. High-resolution transmission electron microscopy (HR-TEM) images were obtained from a JEOL-JEM 2100 microscope, operating at 200 kV, equipped with an energy dispersive X-ray (EDX) elemental analysis system. Some of the samples were studied by X-ray photoelectron spectroscopy (XPS; ULVAC-PHI, PHI Quantera SXM) using AlK α (E = 1486.6 eV) radiation. The X-ray source was operated at 50 W and 15 kV. The core-level signals were obtained at a photoelectron take-off angle of 45° (with respect to the sample surface). The BE scales were referenced to 285.0 eV as determined by the locations of the maximum peaks on the C 1s spectra of hydrocarbon, associated with an adventitious contamination.

Optical absorption and emission properties were measured with toluene solution of the QDs. Optical absorption spectra were recorded using a UV-vis spectrophotometer (JASCO V-650, Japan) with an integrated sphere. Photoluminescence (PL) measurement was carried out using a modular double grating Czerny–Turner monochromator and an iHR 320 emission monochromator (1200 lines per mm of gratings) coupled to a photomultiplier tube (PMT) on a NanoLog Horiba Jovin Yvon spectrofluorometer with a 450 W xenon arc lamp. The spectral resolution of the system is around 0.3 nm. To avoid scattered excitation lights, a cut filter for 395 nm-light was placed in front of the monochromator-PMT setup. The absolute PL quantum yields (QYs) were measured at room temperature using the QY measurement system C9920-02 from Hamamatsu Photonics Co., Ltd. with a 150 W xenon lamp coupled to a monochromator for wavelength discrimination, an integrating sphere as a sample chamber, and a multichannel analyzer for signal detection. Time-resolved fluorescence decay profiles were obtained with a time-correlated single photon counting (TCSPC) lifetime spectroscopy system (NanoLog, Horiba Jovin Yvon, Japan), equipped with pulsed laser diodes ($\lambda_{em} = 375$ nm, average pulse width of 200 ps or less, frequency of 1 MHz) as an excitation light-source. The quality of the fit was assessed based on the R^2 value (~ 1.0) and visual inspection of the residuals.

2.3 Results and discussion

The experimental details for the synthesis of our QDs and their characterization are described in the Experimental session. The synthesis of spherical InP QDs with different diameters was based on a modified version of a previously reported procedure.³² All the precursors (indium acetate [In(Ac)₃], zinc acetate [Zn(Ac)₂], and palmitic acid [PA]) were mixed with 1-octadecene (ODE) at room temperature to avoid alloying (i.e., InZnP).²³ The precursors were heated to 40 °C for the injection of tris(trimethylsilyl)-phosphine [P(TMS)₃] solution with trioctylphosphine (TOP), followed by a reaction at 300 °C to yield an InP QD solution.

Upon coating with a ZnS shell, we modified the previous method.¹⁸ The precursor solution for shell deposition, which was prepared by mixing zinc-oleate stock solution and 1-dodecanethiol (DDT), was added to the InP QD solution at room temperature. Then the QD suspension was heated and kept at 230 °C for 20 min because DDT reacts at 230 °C and releases sulfur.^{33,34} The second injection was carried out by adding the same amount of the Zn-S precursor solution at 230 °C and subsequent heating to 240 °C for 20 min to thicken the shell. The injection of 0.2 mmol Zn-S precursor solution was repeated up to eight times. For each injection cycle, the temperature was raised by 10 °C. After the predetermined number of additions of the Zn-S solution, the products were washed by centrifugation with different solvents to yield a solid as powder samples. All the precursors' solutions were strictly degassed throughout the entire synthesis process. The degassing was one of the critical steps to completely remove organics or byproducts, including acetic acid, to yield excellent optical properties by narrowing the size distribution of core QDs (**Figure 2.1**). In particular, the remaining acetic acid due to incomplete degassing caused a broadening of the first-excitonic absorption peak. When the degree of vacuum for the degassing was optimized at 30 Pa, the

narrowest first-excitonic absorption peak was obtained (**Figure 2.2**). Degas at a vacuum of 10 Pa caused the ODE of the solvent to evaporate and the solution temperature dropped from 120 to below 100 degrees Celsius. This is thought to have resulted in the retention of acetic acid, which causes the blue shift and broadening of the first exciton absorption peak.²²

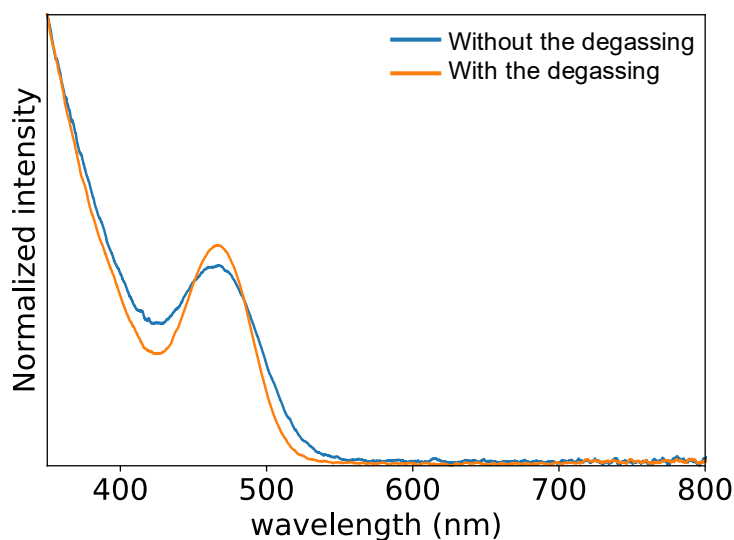


Figure 2.1. Optical absorption spectra of the InP core QD samples. The spectrum color-coded in orange has a sharp first-exciton absorption peak while the other spectrum color-coded in blue has a relatively broad peak. The sharp peak was obtained from the sample which was prepared by injection of $[P(TMS)_3]$ solution, followed by degassing at 30 Pa of vacuum condition. The other sample exhibiting a broad peak was prepared without the degassing of $[P(TMS)_3]$ solution.

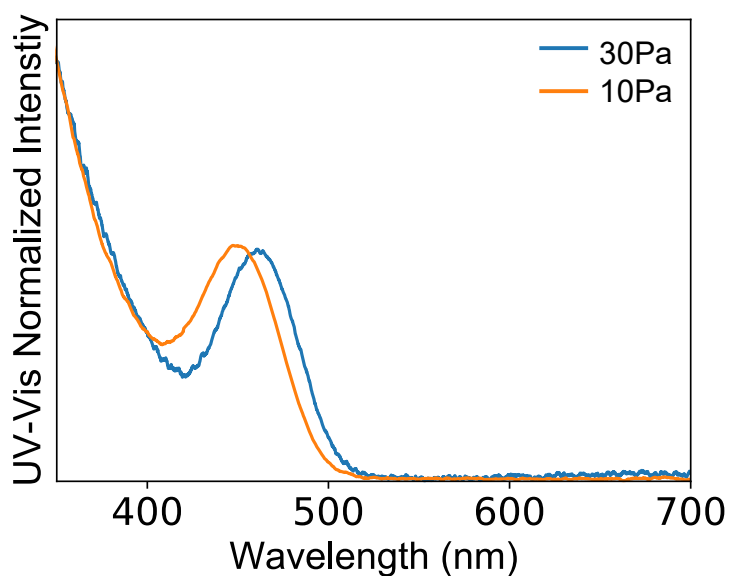


Figure 2.2. Normalized UV-vis spectra of InP core QD samples prepared using the precursor solutions degassed under 10 Pa (color-coded with orange) and 30 Pa (color-coded with blue). The first exciton peak of the sample (blue) is narrower and sharper than that of the sample (orange).

Figure 2.3 shows the typical patterns based on X-ray diffraction (XRD) analysis. Without a shell, the core QDs synthesized had a zinc blende (cubic) InP structure. The mean diameter of the InP core QD was 2.42 nm with a standard deviation of 0.3 nm according to observation using a high-angle annular dark-field scanning transmission electron microscope (HAADF-STEM, **Figure 2.4a**), indicating a narrow size distribution. The measured P/In molar ratio of the core QD was 0.73 according to ICP-OES analysis, which is close to the stoichiometric composition. It is common that the ratio of P/In in the synthesis of InP is often prepared in the range of 0.5 to 1, and ICP results are In-rich.¹⁴ It is known that InP with a narrow particle size distribution can be synthesized in this range.^{32,35} The peak at 20° is considered to be a ligand peak such as palmitic acid, because this peak gradually decreases as the particle size increases with shell growth.

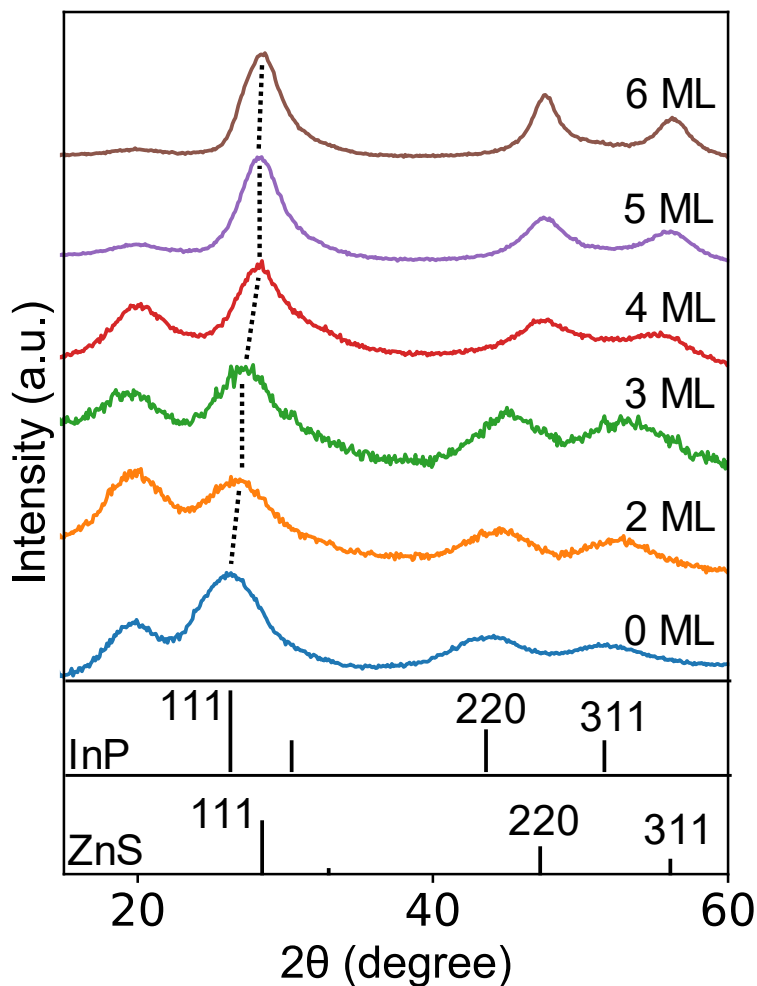


Figure 2.3. X-ray diffraction patterns of the InP core and InP/ZnS core/shell QDs. The broad diffraction peaks at around 20° are attributed to PA ligands bonded to the QD surfaces.

ZnS shells with various thicknesses were deposited onto the core QD by cyclic injection of the Zn-S precursor solution at a predefined temperature. This method is called successful layer absorption and reaction (SILAR), and the shell thickness can be controlled by adjusting the precursor solution concentration, number of injections, reaction time, mild reaction conditions at low temperatures, and pressure.³⁶⁻³⁹ Details of the experiment are described in

the experimental session. Also, shell monolayers on core QDs are generally evaluated by TEM images.^{18,39,40} Shell thickness is calculated from core QD and core/shell QD particle size. Upon adding the corresponding ZnS monolayer (ML), the average thickness of one monolayer of cubic ZnS was 0.27 nm.^{40,41} Each additional layer increased the diameter of the core/shell QD by 0.54 nm, corresponding to the lattice constant of zinc-blend (cubic) bulk ZnS. Thus, it is reasonable that the HAADF-STEM observation identified the average diameters for 3ML, 4ML, 5ML, and 6ML coated samples as 3.96, 4.51, 5.38, and 5.84 nm, respectively (Figure 2.4b,c,d, and Figure 2.5).

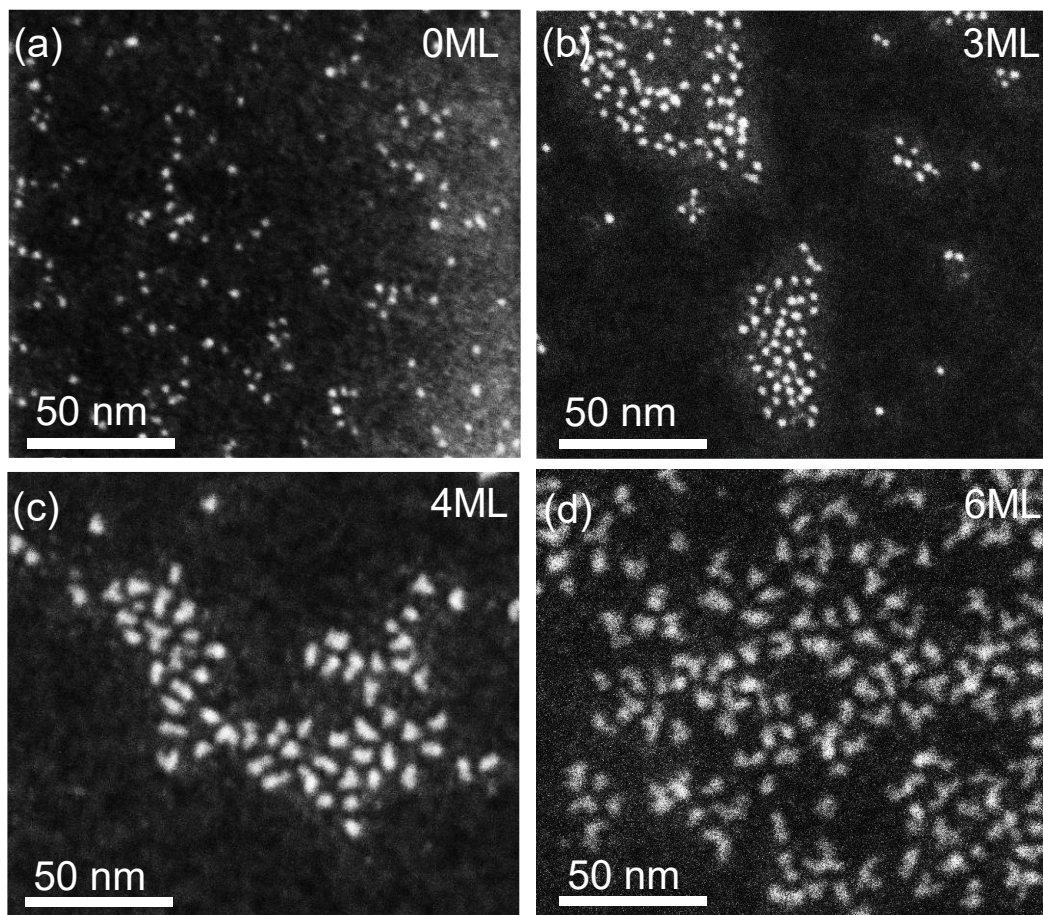


Figure 2.4. HAADF-STEM images of InP(a) and InP coated with ZnS shells of different thickness (b–d).

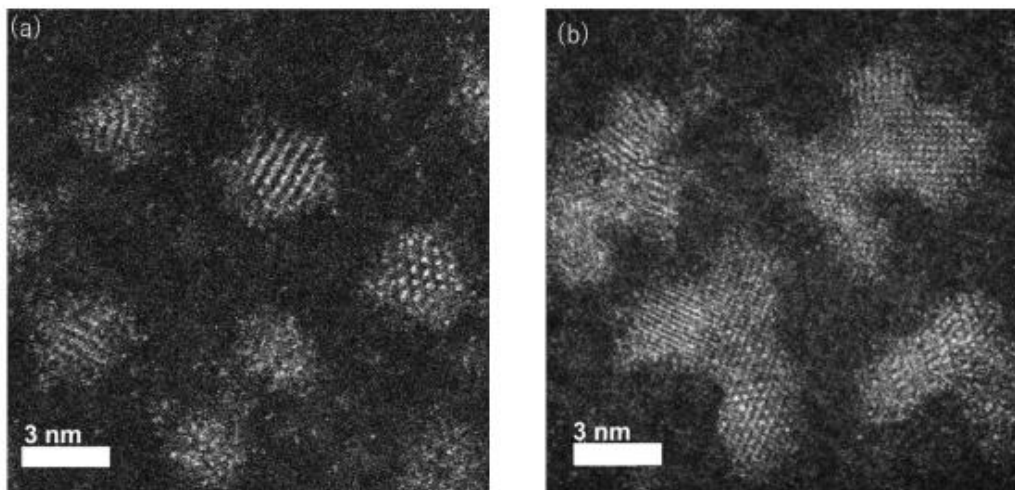


Figure 2.5. The typical HAADF-STEM images of (a) InP/ZnS (3ML) and (b) InP/ZnS (6ML) core/shell QD samples. The photographs (b) indicate that the roughened shape is based on the S-K growth mode.

XRD analysis also supported the increasing trend of the shell thickness. In particular, the relative shift of each XRD peak toward the zinc-blend phase of ZnS with the incremental addition of the Zn-S precursor indicates the growth of the ZnS shell on the core QD. It is particularly noted that the lattice constant of the 3ML-coated sample is 0.563 nm, corresponding to a median value between ZnS and InP. Further deposition of the shell gave a lattice constant nearly close to a ZnS, as evidenced by the XRD analysis for 4ML-, 5ML-, and 6ML-coated samples, consistent with cases of InP/ZnS core/shell QDs reported in the literature.^{42,43} **Figure 2.6a** shows a typical high-resolution (HR) TEM image of the InP/ZnS (3ML) QDs (**Figure 2.4b** and **Figure 2.5a**). A two-dimensional periodic arrangement of the channel structures from one end to the opposite end formed a $\{111\}$ plane with a d-spacing of 0.324 nm, which is equivalent to a lattice constant of 0.563 nm and is consistent with the

result based on the XRD analysis **Figure 2.6b**). On the other hand, $d_{111} = 0.315$ nm measured for the InP/ZnS (6ML) QD (**Figure 2.6c**) was equivalent to the 0.54 nm lattice constant, which corresponds to that of the bulk ZnS.⁴⁴ This is also consistent with XRD analysis (see **Figure 2.6b**).

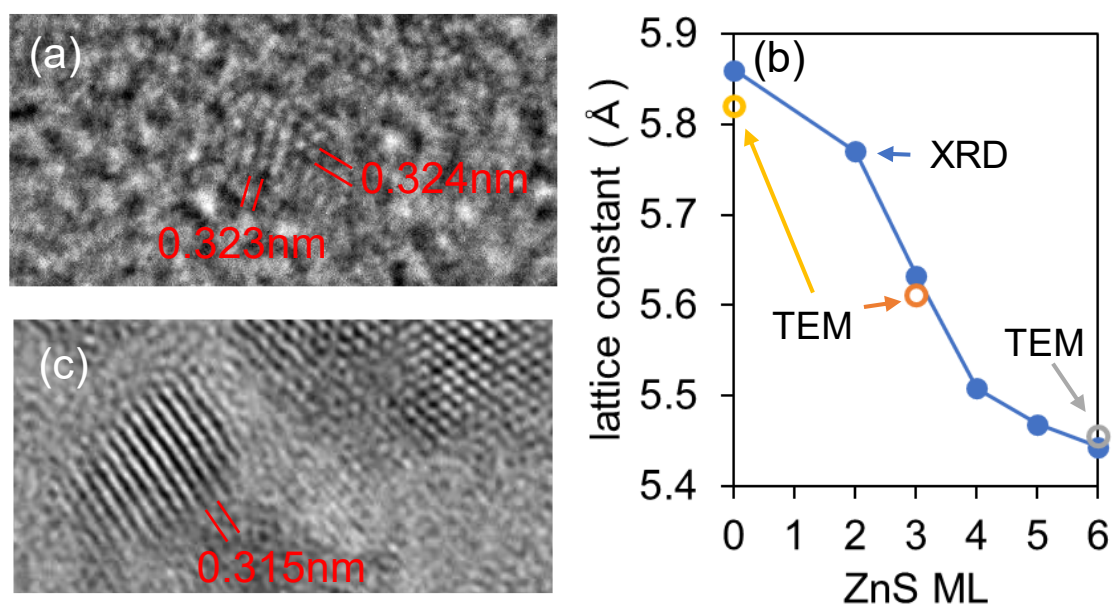


Figure 2.6. Representative HR-TEM images of (a) InP/ZnS (3ML) and (c) InP/ZnS (6ML) QDs. (b) Changes in the lattice parameter of QDs as a function of the shell thickness calculated from Figure 2.3. In the figure, the closed circles were calculated from the diffraction angles while the open circles were calculated from the d-spacing estimated in HR-TEM images. (d) XPS In $3d_{5/2}$ spectra of the InP core QD and InP/ZnS (3ML) QD samples.

There are two possible reasons that the XRD peaks of InP/ZnS (3ML) position at the intermediate angles between InP and ZnS for each plane. First, there is a risk that it could be recognized as the composite diffraction peaks of InP (111), (220) and (331) planes that are superimposed on the peaks of ZnS. To avoid the risk of such a misunderstanding, the InP/ZnS (2ML) sample was measured in the 2θ range of 15–90 degree (Figure 2.7). There are tiny

peaks at around 71.9° and 80.0° corresponding to the (311) and (422) planes of InP. However, there is no peak corresponding to the (331) plane of ZnS, suggesting the disappearance of any Bragg diffractions of ZnS crystal planes in the XRD pattern. As a result, the shift of the diffraction angles observed in the XRD pattern appears due to the compressed crystalline lattice of InP. Therefore, we confirmed that the diffraction peaks are not composite ones but respond to the d-spacing of each plane of InP.

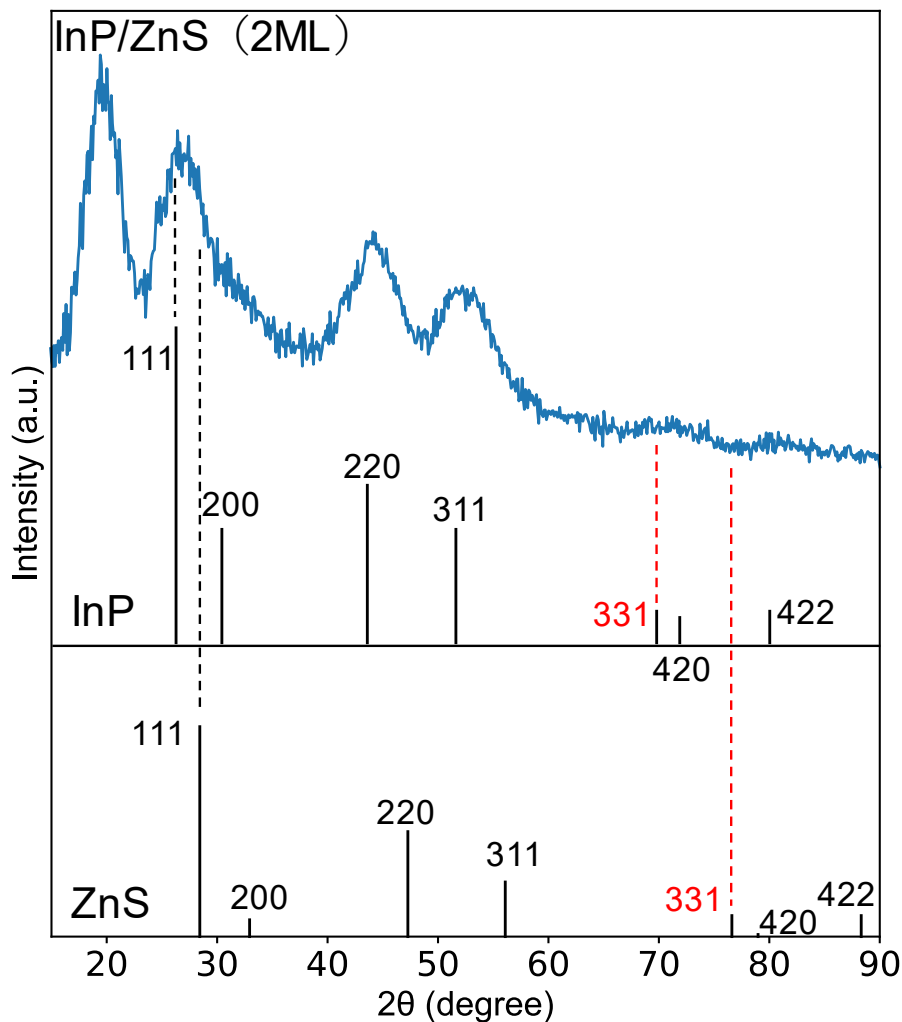


Figure 2.7. XRD pattern of InP/ZnS (2ML). The XRD peaks are very broad due to reduction in diameter of the QDs.

Second, the shift of XRD peaks towards a higher diffraction angle might be rationalized by the formation of the In(Zn)P alloy structure as a core which causes the decrease of the lattice parameter of the InP crystal with the incremental addition of Zn. Several synthetic conditions must be satisfied for alloying. For example, Ramasamy and co-workers reported that the alloying of the In–Zn–P QD structure requires high Zn loadings (feed Zn/In molar ratios, >1).³² Furthermore, they added that the Zn loadings (feed Zn/In molar ratios = 0.5) are too low to generate the alloyed structure using the heat-up method. Most of the Zn^{2+} ions, which are carboxylate species, are known to bind to the surface of InP QD.²² Kirkwood and co-workers reported that the use of hot-injection enables the alloying even at low Zn loadings (feed Zn/In molar ratio, ≤ 1).²² To the best of our knowledge, there is no paper reporting the formation of In(Zn)P alloy QDs when synthesized at low Zn loadings using the heat-up method as well as our approach where the phosphorus precursor was added to the In–P precursor solution at room temperature unlike the hot-injection method. In this context, we next used X-ray photoelectron spectroscopy (XPS) to characterize the chemical states of the core QD on which the 3ML shell was deposited. In **Figure 2.8**, the results of XPS study demonstrate that the In $3d_{5/2}$ and In $3d_{3/2}$ peaks at 444.5 eV and 452.1 eV, which are typical values for bulk crystalline InP,^{43,45} correspond to those of a pure InP QD as a standard synthesized from the In–P precursor solution without $Zn(Ac)_2$. In addition, the In $3d_{5/2}$ peak of the InP/ZnS(3ML) was fitted well with a single Gaussian function (**Figure 2.8**). It has been reported that the crystalline In_2S_3 gives a peak at 445.3 ± 0.1 eV.^{46,47} In our XPS spectrum after 3ML ZnS formation, the $3d_{5/2}$ peak is centered at 444.6 eV and does not have a shoulder at a higher binding energy side. Thus, we concluded the absence of In_2S_3 . The result of curve

fitting with a single Gaussian function reveals the formation of not-alloyed core QDs. If Zn ions diffuse into InP core to form an alloy structure, In $3d_{5/2}$ XPS peak shifts from 444.4 eV to 445.0 eV.^{23,48} But such a shift was not observed after 3ML-shell formation. This In $3d_{5/2}$ peak suggests that it is attributed to a single chemical bonding state of the In-P bond.

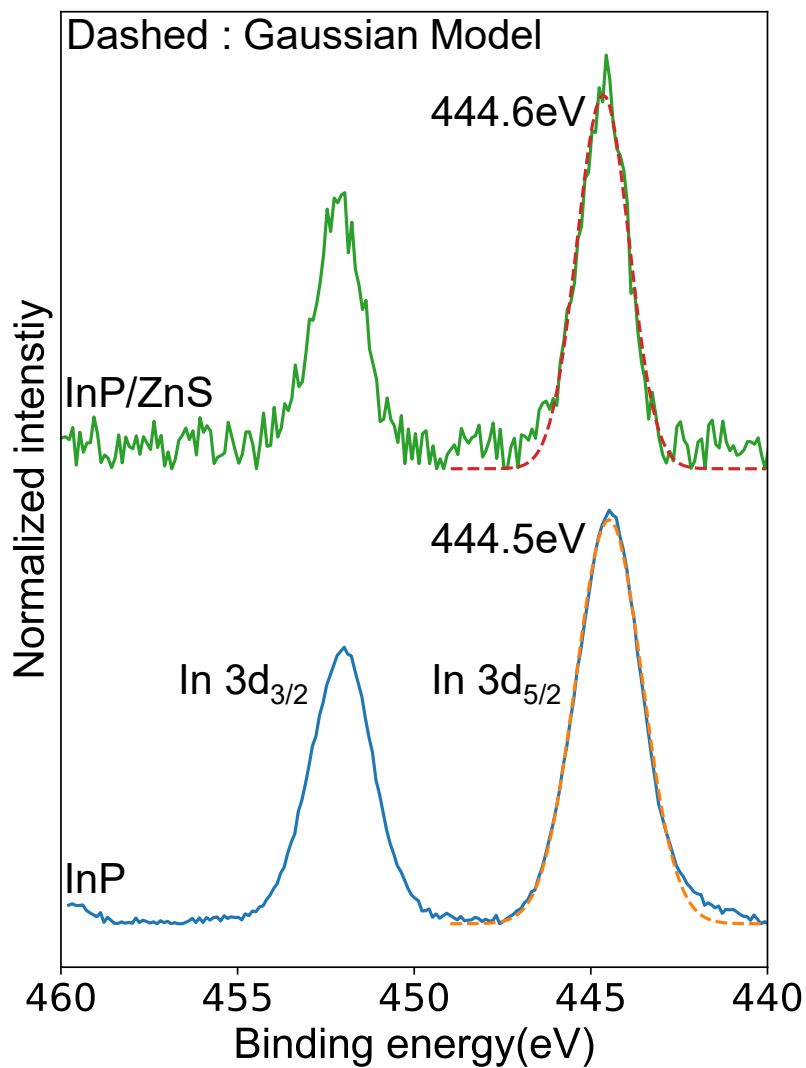


Figure 2.8. In $3d_{5/2}$ XPS signal of the the InP and InP/ZnS (3ML) core/shell QDs with Gaussian fitting.

These results demonstrate that alloying did not occur throughout the whole process for our colloidal synthesis. Thus, the core QD would be under isotropic compression while the shell is under isotropic expansion, and the core/shell QD has a single lattice constant of 0.563 nm as evidenced by HR-TEM study. That is, the core/shell QD has “core/shell lattice coherency”. The appearance of a coherent core/shell QD is also supported by the XRD pattern for the 3ML where the diffraction peaks of core/shell QDs are not broad (or not split into two diffraction lines), as shown in **Figure 2.8**.

Figure 2.9 shows the representative UV-vis and PL spectra of the InP/ZnS (3ML) QD sample. A single peak having a much steeper rise is observed at 465 nm (~ 2.67 eV) in the absorption spectrum. Surprisingly, the estimated value of its valley-depth [VD, defined as $1 - (\text{Abs}_{\text{min}}/\text{Abs}_{\text{max}})$] was 0.51, which is larger than those of the previous InP-based QDs exhibiting the green- (VD = 0.45) and red-emission (VD = 0.5).^{14,49} The appearance of such a sharp first-exciton absorption peak could be interpreted in terms of the effect of the quantum confinement of excitons in the core QDs of a narrower size distribution as is also evidenced by HR-TEM study. In Panel (b), the PL spectrum consists of two peaks: one at 511 nm (~ 2.43 eV) and the other at 660 nm (~ 1.88 eV). The latter is known to originate from the surface trap of indium dangling bonds.⁵⁰

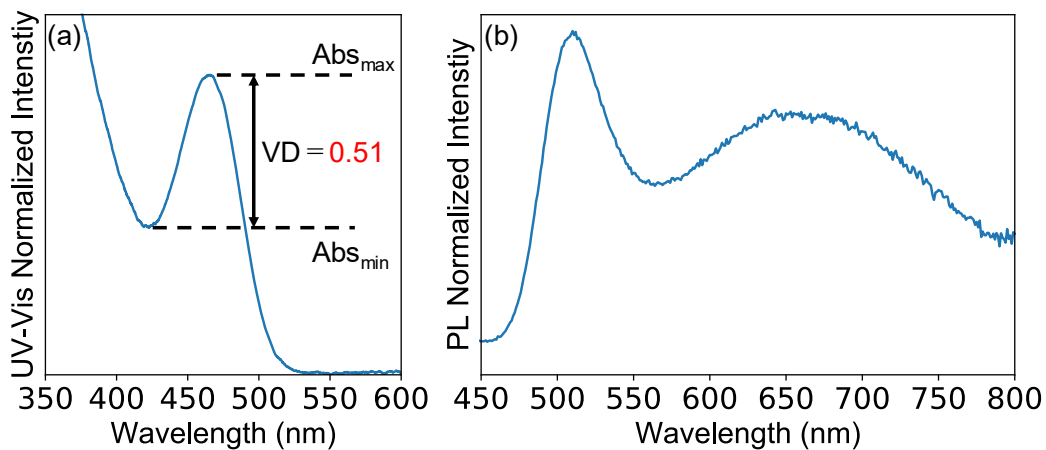


Figure 2.9. (a) Optical absorption and (b) PL spectra of the InP core QD sample.

It is intriguing that the electronic structure of QDs plays a role in the optical properties. **Figure 2.10** and **Figure 2.11** show the optical absorption and PL spectra of InP QDs covered with ZnS shells of different thicknesses. Deposition of ZnS works to reduce the number of dangling bonds and the surface defect emission disappeared, leading to an improved PLQY with incremental deposition of the ZnS shell as shown in **Figure 2.12**. The spread of standard deviations of PLQY and PLFWHM for 2ML samples is due to experimental errors. The mantle heater used for heating causes a large error in the warming time for each experiment. When depositing 2 ML of ZnS thickness, InPQD is raised from room temperature to shell growth temperature of 230 °C, so it is strongly affected by temperature error. After 3 ML, the shell growth temperature has already reached or exceeded, so the effect of temperature error is reduced.

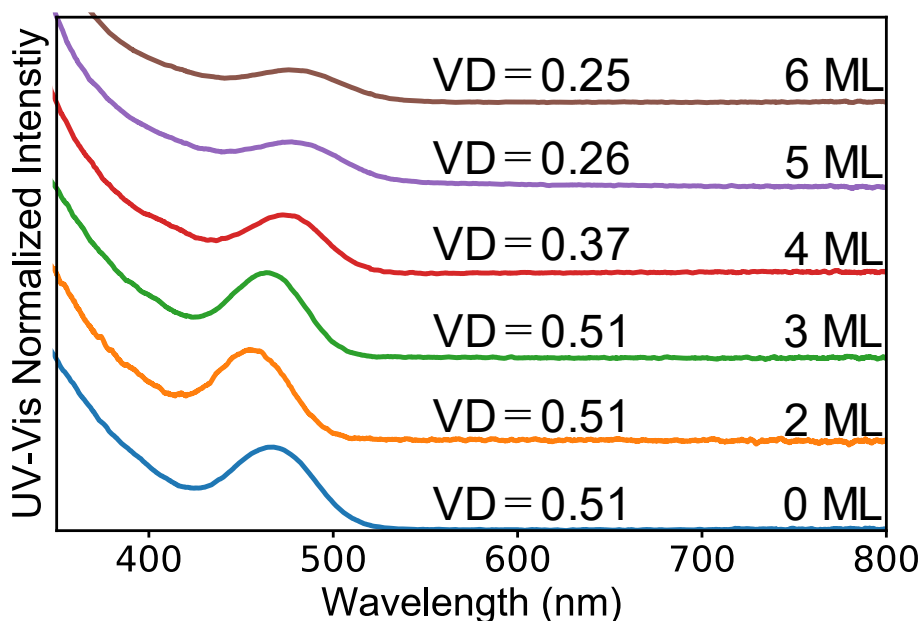


Figure 2.10. Normalized UV-vis of InP QD and InP/ZnS core/shell QDs.

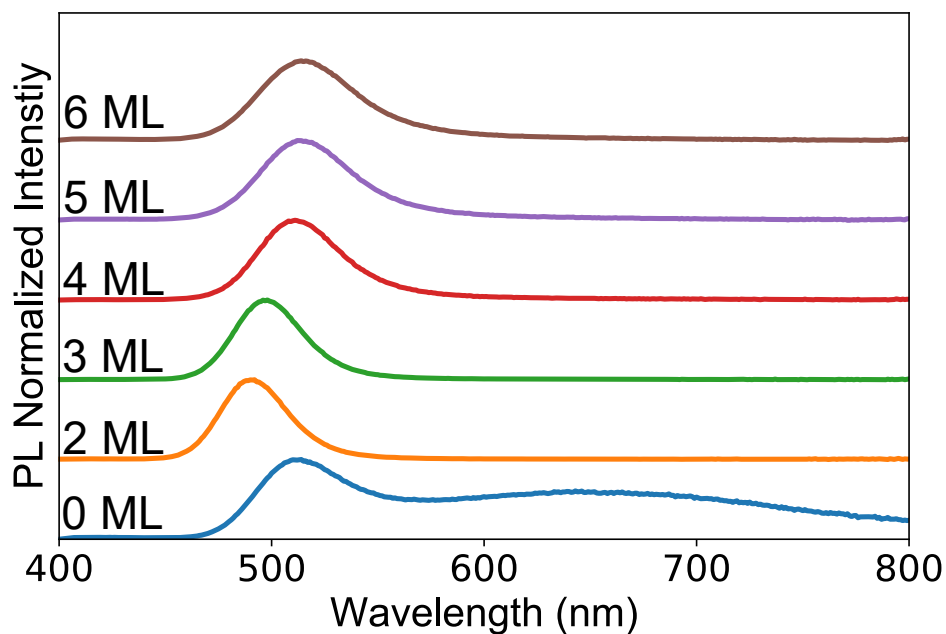


Figure 2.11. Normalized PL spectra of InP QD and InP/ZnS core/shell

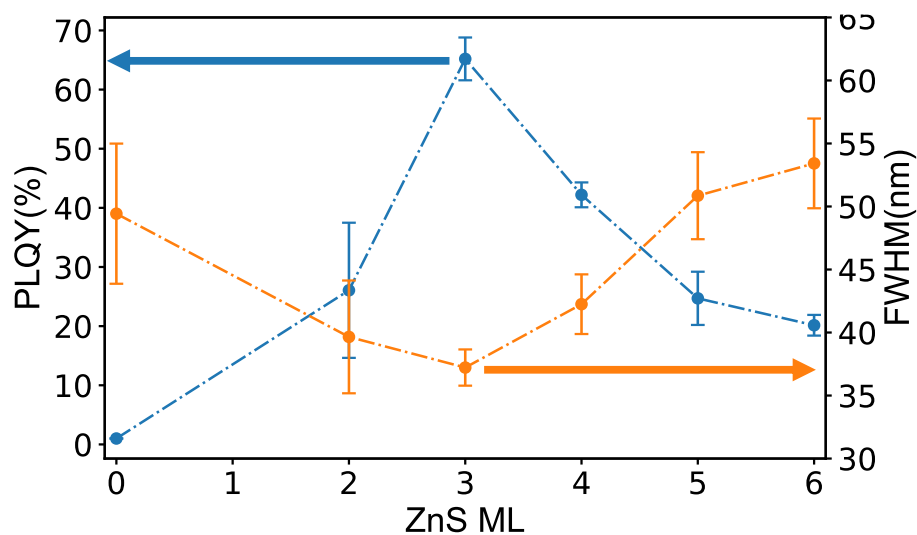


Figure 2.12. Changes in absolute PLQYs (color-coded in blue) and PL-FWHM (color-coded in orange) of InP QD and InP/ZnS core/shell QDs. Error bars represent standard deviations. The number of samples for each is 10, 5, 10, 3, 3, and 3 at 0, 2, 3, 4, 5, and 6 ML.

By deposition of a shell thinner than or equal to 3ML, both absorption and emission spectra shift to the shorter wavelength side. PLE spectra were recorded for the PL peaks, respectively (Figure 2.13). The thin-shelled QDs differ from the thick-shelled QDs in the spectral peak position and shape.

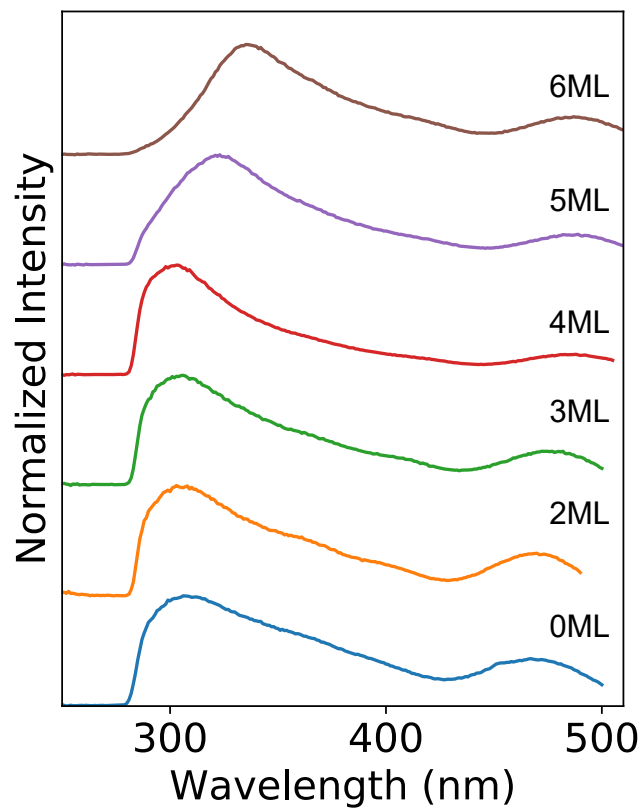


Figure 2.13. PLE spectra of the InP QDs covered with ZnS shells of different thicknesses.

On the assumption that the InP QD is not alloyed, there are two possible mechanisms to explain the spectral blueshift observed for the thinner shells. First, the partial etching of the core QD from its surface with DDT molecules is possible to cause a blueshift of the spectra.⁵¹ Indeed, it is readily predicted that the size reduction owing to sulfur etching of core QD results in a widening of the fundamental bandgap based on the effect of quantum

confinement; however, this mechanism does not work for the explanation of the spectral redshift with the incremental deposition of Zn ions for the thicker shells (i.e., 4ML or more). The results of the XPS study also defy the sulfur etching process because of the absence of In 3d_{5/2} XPS signals that are attributed to an In-S bond resulting from the diffusion of sulfur ions into the core lattice (**Figure 2.8**).⁵² Therefore, we concluded that the sulfur etching did not happen in our case. The second mechanism is convincing to explain the spectral shift. In particular, the increase in the bandgap of InP core QDs results from the compressed lattice. As evidenced by analysis combining XRD, XPS, STEM and HR-TEM, the lattice constant of InP decreases to 0.563 nm when coated with a ZnS shell of 3ML.

Figure 2.12 shows the increase of the PLQY and narrowing PL linewidth with incremental deposition of the ZnS shell by 3ML. The best pair value of 70% PLQY and 36 nm PL-FWHM was obtained for the InP/ZnS (3ML) core/shell QD. To the best of our knowledge, the 70% of PLQY is a record value for the InP/ZnS core/shell QDs. In general, the PLQY is also given by eqn (1) where $k_r = 1/\tau_r$ and $k_{nr} = 1/\tau_{nr}$ (τ is the characteristic PL lifetime) using two parameters of k_r for the radiative and k_{nr} for the nonradiative processes.⁵³ In this context, we measured the time-resolved PL spectra at room temperature for the InP core QD and InP/ZnS (3ML) core/shell QD samples (**Figure 2.14**, and **Table 2.1**).

$$PLQY = \frac{k_r}{k_r + k_{nr}} = \tau_{avg} k_r = \frac{\tau_{avg}}{\tau_r} \quad (1)$$

$$\tau_{avg} = \frac{1}{k_r + k_{nr}} \quad (2)$$

where k_r is the radiative recombination rate, k_{nr} is the nonradiative recombination rate, τ_{avg} is the average value calculated using experimental values of PL lifetime, and τ_r is the radiative

decay time. In **Table 2.1**, the estimated parameters as a result of the fitting along with the fully satisfactory values of statistical deviation R^2 are summarized. The average decay time, which was 6.19 nsec for the core QD, was increased significantly to 7–8 times by encapsulation with 3ML of the ZnS shell. Based on eqn (1) and (2)⁵³ we calculated radiative (k_r) and nonradiative recombination (k_{nr}) rates for the unshelled and shelled QDs. The radiative recombination rate has increased threefold while the nonradiative recombination rate was down more than twenty-six times, suggesting the significant reduction in nonradiative decay channels by 3ML ZnS shell formation.

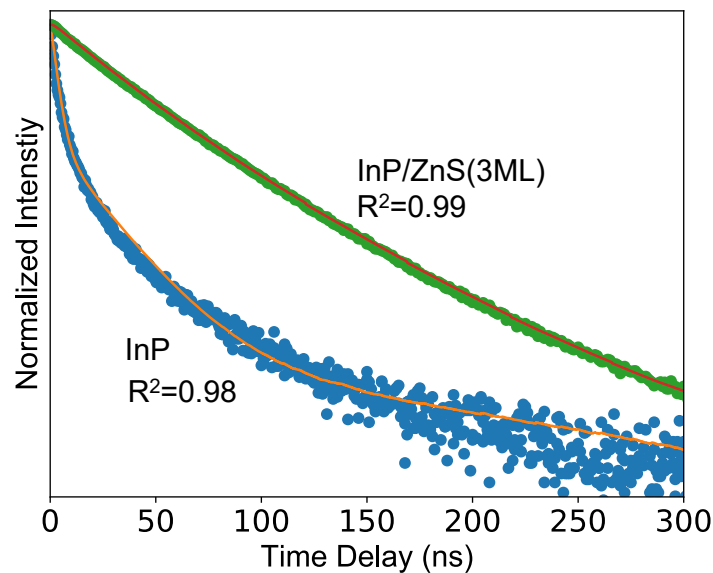


Figure 2.14. PL decay profiles of the InP core QD (blue dots) and the InP/ZnS (3ML) core/shell QD (green dots), respectively. Both PL decay curves were measured for each PL maximum estimated in Figure 2.11.

Table 2.1. Parameters obtained by fitting

sample	$A_1(10^{-2})$	$\tau_1(\text{ns})$	$A_2(10^{-2})$	$\tau_2(\text{ns})$	$\tau_{\text{avg}}(\text{ns})$	PLQY(%)	τ_{red}	$k_r(\text{ns}^{-1})$	$k_{nr}(\text{ns}^{-1})$
InP	6.17	26.4	39.1	3.00	6.19	0.03	206.31	0.005	0.157
InP/ZnS(3ML)	31.4	32.2	30.2	63.8	47.7	0.70	68.13	0.015	0.006

Figure 2.15 shows the typical absorption and PL spectra of the 3ML-ZnS coated sample. The sharpness of the first-exciton peak with VD of 0.51 together with the PL-FWHM of 36 nm indicates a narrow size distribution of the core QD even after the formation of a 3ML-thick shell. The PL spectrum exhibits a band edge emission and has a single Gaussian-like peak without a long emission tail. When a mean diameter of the InP core QD increased to 2.64 nm (standard deviation of 0.3 nm), the PL spectral peak shifted to 523 nm (~ 2.37 eV, see **Figure 2.15b**) based on the quantum confinement effect. An absolute PLQY of 72% suggests that the coherent core-shell structure is retained. The first-exciton peak in the absorption spectrum, having a VD of 0.48, is slightly broader than that of the sample shown in Panel (d). This could be attributed to a longer reaction time for the core synthesis encourages crystal growth based on Ostwald ripening, resulting in a 40 nm (~ 184 meV) of PL-FWHM. The successful tuning of the PL spectra suggests that a deep-green emission range could be covered by the core/shell coherent QD system (**Figure 2.16**). The critical thickness of ZnS to retain the core/shell coherency was 0.81 nm.

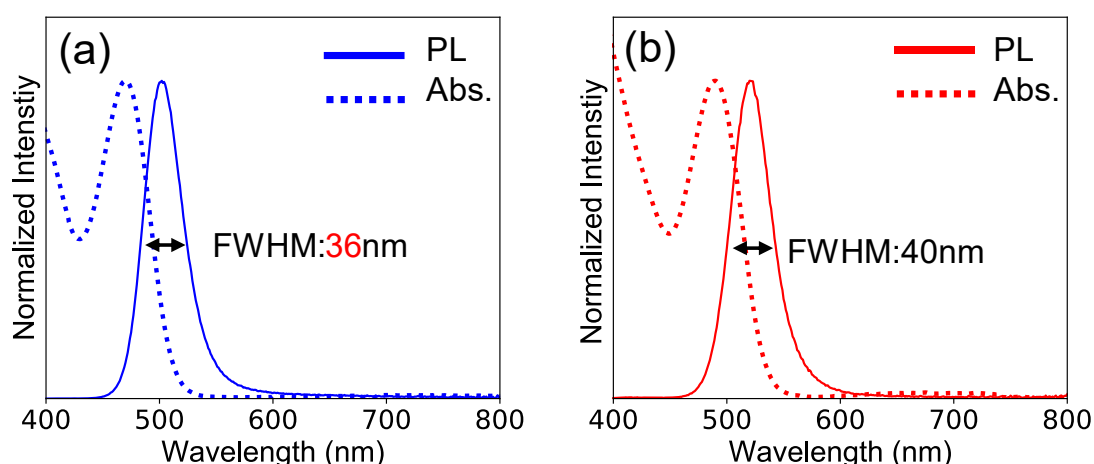


Figure 2.15. UV-vis and PL spectra of (a) InP (2.42 nm) and (b) InP (2.64 nm) coated with ZnS (3ML) shells.

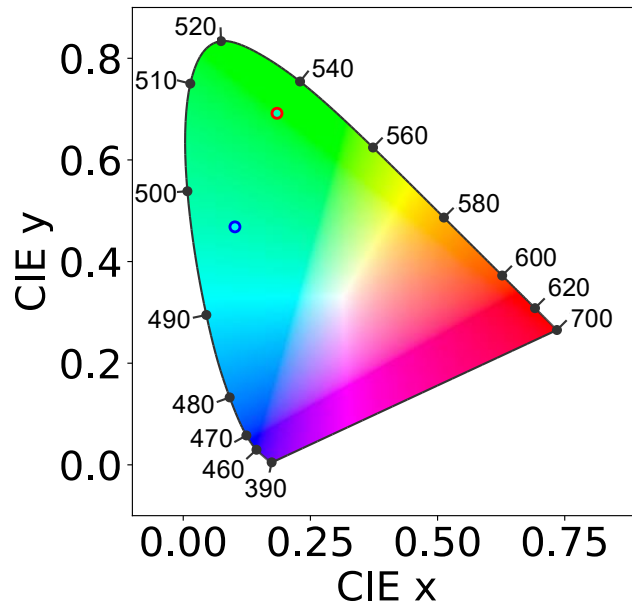


Figure 2.16. CIE diagram showing chromaticity coordinates of PL spectra of Figure 2.15(a) and (b).

Unlike the case of thinner shells (~3ML), the deposition of 4ML or even thicker shells resulted in poor optical performances as shown in **Figure 2.12**. First, the PLQY decreased as the shell thickness increased. Second, the PL-FWHM increases with incremental thickness of the shell and reaches 50 nm (~229 meV) at 6ML. Third, the PL spectrum shifts to longer wavelengths as does the optical absorption spectrum (**Figure 2.10** and **Figure 2.11**).

Since the lattice constants of the QDs covered with ZnS shells (4–6ML) return to the bulk value according to the results of structural analysis mentioned above, it is reasonable to discuss that the isotropic pressure on the core QD is released during the formation of the 4ML-shell. In this situation, a lattice structure with a constant of 0.563 nm is no longer thermodynamically favored for the core InP QDs and the bulky configuration is recovered.

The resultant heterostructure introduces a lattice mismatch ($\sim 7.8\%$) between the core and shell materials, leading to a defective interface to minimize the lattice strain energy. It is reported that Stranski–Krastanov (S–K) shell film growth roughens the QD surface as strain is released.^{54,55} In this study, similar island-like shapes were observed by HAADF-STEM as evidenced in **Figure 2.4c** and **Figure 2.5**. The emerging defects at the heterogeneous interface might act as electron–hole recombination centers, resulting in the decreasing trend of PLQY as shown in **Figure 2.12**.

Now, the PL peaks for the 5ML- and 6ML-coated QD samples shift to longer wavelengths than that of the core-only QD (**Figure 2.11**). The recovery in the lattice constant of the core QD resulting from releasing the strain energy is not enough to explain the redshift amount. One possible reason is the growing emission tails with incremental shell-thickness (**Figure 2.17**). The spectrum of the 4ML-coated QD has a tiny emission tail at a longer wavelength. As is predicted, we see the growing emission tails after coating with 5ML and 6ML shells. The PL spectral peaks of the 5ML and 6ML-coated QDs are pulled to long wavelengths due to contribution of the emission tails, resulting in a PL peak shift to longer wavelengths as shown in **Figure 2.11**. The appearance of those tails suggests the formation of defective interfaces, consistent with the dropping trend of PLQY with shell thickness. PLE spectra were recorded for the PL peaks at 520 nm and the tail-emission peak at 580 nm for the QDs covered with ZnS shells (3ML) and (6ML), respectively (**Figure 2.13**).

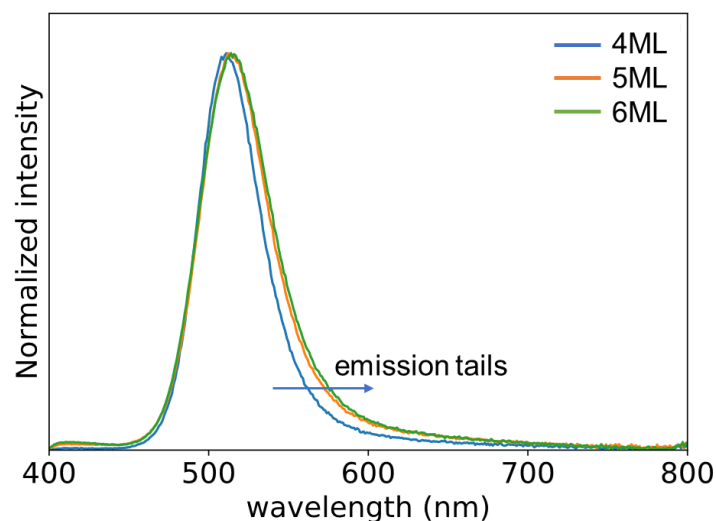


Figure 2.17. PL spectra of InP QDs coated with ZnS shells of 4ML, 5ML and 6ML.

For the 3ML-shelled sample, the PLE spectrum (Figure 2.13) of the higher energy peak is similar to that of the lower energy peak in terms of the spectral shape and position, suggesting the same PL origin each other. For the 6ML-shelled sample, the higher energy peak locates at ~ 320 nm that differs from the lower energy peak position. Although the PL mechanism is unknown at present, the thicker-shelled QDs might have a different PL origin for tail emission. Thus, PL peak positions are influenced by the contribution of the growing emission tail, resulting in a small redshift. For the thicker-shelled QDs, the PL-FWHM increases as the shell is thickened as clearly seen in **Figure 2.12**. A similar trend has been observed for the alloyed In(Zn)P QDs.^{22,23} According to those papers, the inhomogeneous incorporation of Zn ions into a core InP lattice occurs to form the alloy structure during the formation of the shell. The resultant inhomogeneous areas distributed in the core QD results in lessened crystal symmetry and enhanced geometrical distortion, causing an enhanced electron–phonon coupling.⁵⁶ On the other hand, there are a few papers reporting the shell-thickness

dependence of PL-FWHM of the unalloyed InP QD. For example, Tessier and co-workers reported an increasing trend of PL-FWHM with incremental shell-thickness while the PLQY also increases,³³ inconsistent with our case.

We next discuss the possible reason for the increasing trend of PL-FWHM as the shell is thickened in the absence of alloyed QD. The Stokes shift, ΔE , which is defined as the difference in photon energy between the first exciton peak of absorption and emission peak maxima, is plotted in **Figure 2.18**. The ΔE drop-off increases by ZnS (3ML) and decreases in the 4–6ML range. If the spectral peak position depends exclusively on core QD size, the ΔE should be a constant. Hence, another parameter is necessary to explain the decreasing trend of ΔE for particularly the thinner shell QDs. Here, the Stokes shift is expressed as $\Delta E = 2S\hbar\omega_p$, where S is the Huang–Rhys factor and $\hbar\omega_p$ is the energy of phonons coupled to electrons.⁵⁷ As discussed above, the decreasing trends in ΔE and PL-FWHM for the QDs with thinner shells (~3ML) appear due to the lessened defects in the interface between the shell and core. The Huang–Rhys factor refers to phonons emitted as the excited electrons return to the ground state. It is known that the shell thickness is one of the physical parameters to influence the electron–phonon interaction. Actually, Lange and co-workers revealed that coating a CdSe core QD with a ZnS shell causes the decrease of the Huang–Rhys factor.⁵⁸ The decrease of the Huang–Rhys factor appears due to the weakened exciton–LO-phonon interaction, leading to the strengthened confinement which is observed for the core/shell QDs of type-I structure.⁵⁹

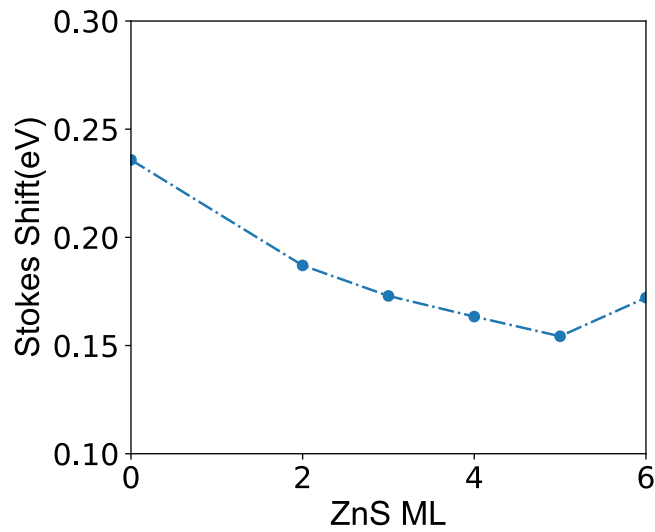


Figure 2.18. Changes in magnitude of Stoke shift between the first exciton absorption peaks and PL peaks plotted as a function of ZnS ML.

2.4 Conclusions

In conclusion, this study investigated the influence of shell thickness on the optical properties to realize the heavy-metal-free QDs emitting light in a deep-green wavelength range. Adopting InP and ZnS as the core and shell materials, respectively, optimized the conditions to create a core/shell coherency, which was retained throughout the core/shell QD. Under these conditions, the lattice contrast of the InP core QD was reduced to 0.563 nm, which corresponds with that of the ZnS shell. Hence, the emerging defect-less core/shell interface dramatically improves the PLQY up to 70% and narrows the PL bandwidth of 36 nm. This work also demonstrates the successful synthesis of core/shell coherent QDs even from the material with a higher bulk modulus value, affecting others for a new class of strained materials.

References

- (1) Yoo, J. J.; Seo, G.; Chua, M. R.; Park, T. G.; Lu, Y.; Rotermund, F.; Kim, Y.-K.; Moon, C. S.; Jeon, N. J.; Correa-Baena, J.-P.; Bulović, V.; Shin, S. S.; Bawendi, M. G.; Seo, J. Efficient Perovskite Solar Cells via Improved Carrier Management. *Nature* **2021**, *590* (7847), 587–593. <https://doi.org/10.1038/s41586-021-03285-w>.
- (2) Zhou, W.; Shang, Y.; García de Arquer, F. P.; Xu, K.; Wang, R.; Luo, S.; Xiao, X.; Zhou, X.; Huang, R.; Sargent, E. H.; Ning, Z. Solution-Processed Upconversion Photodetectors Based on Quantum Dots. *Nat Electron* **2020**, *3* (5), 251–258. <https://doi.org/10.1038/s41928-020-0388-x>.
- (3) Hanifi, D. A.; Bronstein, N. D.; Koscher, B. A.; Nett, Z.; Swabeck, J. K.; Takano, K.; Schwartzberg, A. M.; Maserati, L.; Vandewal, K.; van de Burgt, Y.; Salleo, A.; Alivisatos, A. P. Redefining Near-Unity Luminescence in Quantum Dots with Photothermal Threshold Quantum Yield. *Science* **2019**, *363* (6432), 1199–1202. <https://doi.org/10.1126/science.aat3803>.
- (4) Jiang, Y.; Weiss, E. A. Colloidal Quantum Dots as Photocatalysts for Triplet Excited State Reactions of Organic Molecules. *J. Am. Chem. Soc.* **2020**, *142* (36), 15219–15229. <https://doi.org/10.1021/jacs.0c07421>.
- (5) Özbilgin, İ. N. G.; Ghosh, B.; Yamada, H.; Shirahata, N. Size-Dependent Photothermal Performance of Silicon Quantum Dots. *J. Phys. Chem. C* **2021**, *125* (6), 3421–3431. <https://doi.org/10.1021/acs.jpcc.0c10027>.
- (6) Liu, Q.; Yin, J.; Zhang, B.-B.; Chen, J.-K.; Zhou, Y.; Zhang, L.-M.; Wang, L.-M.; Zhao, Q.; Hou, J.; Shu, J.; Song, B.; Shirahata, N.; Bakr, O. M.; Mohammed, O. F.; Sun, H.-T. Theory-Guided Synthesis of Highly Luminescent Colloidal Cesium Tin Halide Perovskite Nanocrystals. *J. Am. Chem. Soc.* **2021**, *143* (14), 5470–5480. <https://doi.org/10.1021/jacs.1c01049>.
- (7) Guo, T.; Tang, Q.; Guo, Y.; Qiu, H.; Dai, J.; Xing, C.; Zhuang, S.; Huang, G. Boron Quantum Dots for Photoacoustic Imaging-Guided Photothermal Therapy. *ACS Appl. Mater. Interfaces* **2021**, *13* (1), 306–311. <https://doi.org/10.1021/acsami.0c21198>.
- (8) Jang, E.; Kim, Y.; Won, Y.-H.; Jang, H.; Choi, S.-M. Environmentally Friendly InP-Based Quantum Dots for Efficient Wide Color Gamut Displays. *ACS Energy Lett.* **2020**, *5* (4), 1316–1327. <https://doi.org/10.1021/acsenerylett.9b02851>.
- (9) Ghosh, B.; Hamaoka, T.; Nemoto, Y.; Takeguchi, M.; Shirahata, N. Impact of Anchoring Monolayers on the Enhancement of Radiative Recombination in Light-Emitting Diodes Based on Silicon Nanocrystals. *J. Phys. Chem. C* **2018**, *122* (11), 6422–6430. <https://doi.org/10.1021/acs.jpcc.7b12812>.
- (10) Coughlan, C.; Ibáñez, M.; Dobrozhan, O.; Singh, A.; Cabot, A.; Ryan, K. M. Compound Copper Chalcogenide Nanocrystals. *Chem. Rev.* **2017**, *117* (9), 5865–6109. <https://doi.org/10.1021/acs.chemrev.6b00376>.
- (11) Reiss, P.; Protière, M.; Li, L. Core/Shell Semiconductor Nanocrystals. *Small* **2009**, *5* (2), 154–168. <https://doi.org/10.1002/sml.200800841>.

- (12) Tamang, S.; Lincheneau, C.; Hermans, Y.; Jeong, S.; Reiss, P. Chemistry of InP Nanocrystal Syntheses. *Chemistry of Materials* **2016**, *28* (8), 2491–2506. <https://doi.org/10.1021/acs.chemmater.5b05044>.
- (13) Biadala, L.; Siebers, B.; Beyazit, Y.; Tessier, Mickaël. D.; Dupont, D.; Hens, Z.; Yakovlev, D. R.; Bayer, M. Band-Edge Exciton Fine Structure and Recombination Dynamics in InP/ZnS Colloidal Nanocrystals. *ACS Nano* **2016**, *10* (3), 3356–3364. <https://doi.org/10.1021/acsnano.5b07065>.
- (14) Won, Y.-H.; Cho, O.; Kim, T.; Chung, D.-Y.; Kim, T.; Chung, H.; Jang, H.; Lee, J.; Kim, D.; Jang, E. Highly Efficient and Stable InP/ZnSe/ZnS Quantum Dot Light-Emitting Diodes. *Nature* **2019**, *575* (7784), 634–638. <https://doi.org/10.1038/s41586-019-1771-5>.
- (15) Wu, Z.; Liu, P.; Zhang, W.; Wang, K.; Sun, X. W. Development of InP Quantum Dot-Based Light-Emitting Diodes. *ACS Energy Lett.* **2020**, *5* (4), 1095–1106. <https://doi.org/10.1021/acsenergylett.9b02824>.
- (16) Li, Y.; Hou, X.; Dai, X.; Yao, Z.; Lv, L.; Jin, Y.; Peng, X. Stoichiometry-Controlled InP-Based Quantum Dots: Synthesis, Photoluminescence, and Electroluminescence. *J. Am. Chem. Soc.* **2019**, *141* (16), 6448–6452. <https://doi.org/10.1021/jacs.8b12908>.
- (17) Kim, Y.; Ham, S.; Jang, H.; Min, J. H.; Chung, H.; Lee, J.; Kim, D.; Jang, E. Bright and Uniform Green Light Emitting InP/ZnSe/ZnS Quantum Dots for Wide Color Gamut Displays. *ACS Appl. Nano Mater.* **2019**, *2* (3), 1496–1504. <https://doi.org/10.1021/acsanm.8b02063>.
- (18) Cao, F.; Wang, S.; Wang, F.; Wu, Q.; Zhao, D.; Yang, X. A Layer-by-Layer Growth Strategy for Large-Size InP/ZnSe/ZnS Core-Shell Quantum Dots Enabling High-Efficiency Light-Emitting Diodes. *Chemistry of Materials* **2018**, *30* (21), 8002–8007. <https://doi.org/10.1021/acs.chemmater.8b03671>.
- (19) Jo, J.-H.; Jo, D.-Y.; Lee, S.-H.; Yoon, S.-Y.; Lim, H.-B.; Lee, B.-J.; Do, Y. R.; Yang, H. InP-Based Quantum Dots Having an InP Core, Composition-Gradient ZnSeS Inner Shell, and ZnS Outer Shell with Sharp, Bright Emissivity, and Blue Absorptivity for Display Devices. *ACS Appl. Nano Mater.* **2020**, *3* (2), 1972–1980. <https://doi.org/10.1021/acsanm.0c00008>.
- (20) Zhang, W.; Zhuang, W.; Liu, R.; Xing, X.; Qu, X.; Liu, H.; Xu, B.; Wang, K.; Sun, X. W. Double-Shelled InP/ZnMnS/ZnS Quantum Dots for Light-Emitting Devices. *ACS Omega* **2019**, *4* (21), 18961–18968. <https://doi.org/10.1021/acsomega.9b01471>.
- (21) Cho, E.; Jang, H.; Lee, J.; Jang, E. Modeling on the Size Dependent Properties of InP Quantum Dots: A Hybrid Functional Study. *Nanotechnology* **2013**, *24* (21), 215201. <https://doi.org/10.1088/0957-4484/24/21/215201>.
- (22) Kirkwood, N.; De Backer, A.; Altantzis, T.; Winckelmans, N.; Longo, A.; Antolinez, F. V.; Rabouw, F. T.; De Trizio, L.; Geuchies, J. J.; Mulder, J. T.; Renaud, N.; Bals, S.; Manna, L.; Houtepen, A. J. Locating and Controlling the Zn Content in In(Zn)P Quantum Dots. *Chem. Mater.* **2020**, *32* (1), 557–565. <https://doi.org/10.1021/acs.chemmater.9b04407>.
- (23) Pietra, F.; De Trizio, L.; Hoekstra, A. W.; Renaud, N.; Prato, M.; Grozema, F. C.; Baesjou, P. J.; Koole, R.; Manna, L.; Houtepen, A. J. Tuning the Lattice Parameter of $\text{In}_x\text{Zn}_y\text{P}$ for Highly Luminescent

- Lattice-Matched Core/Shell Quantum Dots. *ACS Nano* **2016**, *10* (4), 4754–4762. <https://doi.org/10.1021/acsnano.6b01266>.
- (24) Lim, J.; Bae, W. K.; Lee, D.; Nam, M. K.; Jung, J.; Lee, C.; Char, K.; Lee, S. InP@ZnSeS, Core@Composition Gradient Shell Quantum Dots with Enhanced Stability. *Chemistry of Materials* **2011**, *23* (20), 4459–4463. <https://doi.org/10.1021/cm201550w>.
- (25) Lim, J.; Park, M.; Bae, W. K.; Lee, D.; Lee, S.; Lee, C.; Char, K. Highly Efficient Cadmium-Free Quantum Dot Light-Emitting Diodes Enabled by the Direct Formation of Excitons within InP@ZnSeS Quantum Dots. *ACS Nano* **2013**, *7* (10), 9019–9026. <https://doi.org/10.1021/nn403594j>.
- (26) Kim, S.; Kim, T.; Kang, M.; Kwak, S. K.; Yoo, T. W.; Park, L. S.; Yang, I.; Hwang, S.; Lee, J. E.; Kim, S. K.; Kim, S.-W. Highly Luminescent InP/GaP/ZnS Nanocrystals and Their Application to White Light-Emitting Diodes. *J. Am. Chem. Soc.* **2012**, *134* (8), 3804–3809. <https://doi.org/10.1021/ja210211z>.
- (27) Srivastava, V.; Kamysbayev, V.; Hong, L.; Dunietz, E.; Klie, R. F.; Talapin, D. V. Colloidal Chemistry in Molten Salts: Synthesis of Luminescent In_{1-x}Ga_xP and In_{1-x}Ga_xAs Quantum Dots. *J. Am. Chem. Soc.* **2018**, *140* (38), 12144–12151. <https://doi.org/10.1021/jacs.8b06971>.
- (28) Smith, A. M.; Mohs, A. M.; Nie, S. Tuning the Optical and Electronic Properties of Colloidal Nanocrystals by Lattice Strain. *Nature Nanotech* **2009**, *4* (1), 56–63. <https://doi.org/10.1038/nnano.2008.360>.
- (29) Gong, K.; Kelley, D. F. Lattice Strain Limit for Uniform Shell Deposition in Zincblende CdSe/CdS Quantum Dots. *J. Phys. Chem. Lett.* **2015**, *6* (9), 1559–1562. <https://doi.org/10.1021/acs.jpcclett.5b00566>.
- (30) Lange, H.; Kelley, D. F. Spectroscopic Effects of Lattice Strain in InP/ZnSe and InP/ZnS Nanocrystals. *J. Phys. Chem. C* **2020**, *124* (41), 22839–22844. <https://doi.org/10.1021/acs.jpcc.0c07145>.
- (31) Liu, H.; Zhao, X.; Yang, X.; Wang, Y.; Wu, M.; Jiang, J.; Wu, G.; Yuan, K.; Sui, L.; Zou, B. Piezochromic Luminescence in All-Inorganic Core–Shell InP/ZnS Nanocrystals *via* Pressure-Modulated Strain Engineering. *Nanoscale Horiz.* **2020**, *5* (8), 1233–1239. <https://doi.org/10.1039/D0NH00145G>.
- (32) Ramasamy, P.; Kim, N.; Kang, Y.-S.; Ramirez, O.; Lee, J.-S. Tunable, Bright, and Narrow-Band Luminescence from Colloidal Indium Phosphide Quantum Dots. *Chemistry of Materials* **2017**, *29* (16), 6893–6899. <https://doi.org/10.1021/acs.chemmater.7b02204>.
- (33) Tessier, M. D.; Dupont, D.; De Nolf, K.; De Roo, J.; Hens, Z. Economic and Size-Tunable Synthesis of InP/ZnE (E = S, Se) Colloidal Quantum Dots. *Chemistry of Materials* **2015**, *27* (13), 4893–4898. <https://doi.org/10.1021/acs.chemmater.5b02138>.
- (34) Li, L.; Reiss, P. One-Pot Synthesis of Highly Luminescent InP/ZnS Nanocrystals without Precursor Injection. *Journal of the American Chemical Society* **2008**, *130* (35), 11588–11589. <https://doi.org/10.1021/ja803687e>.
- (35) Xu, Z.; Li, Y.; Li, J.; Pu, C.; Zhou, J.; Lv, L.; Peng, X. Formation of Size-Tunable and Nearly Monodisperse InP Nanocrystals: Chemical Reactions and Controlled Synthesis. *Chem. Mater.* **2019**, *31*

- (14), 5331–5341. <https://doi.org/10.1021/acs.chemmater.9b02292>.
- (36) Zhang, H.; Tong, J.; Fang, W.; Qian, N.; Zhao, Q. Efficient Flexible Counter Electrode Based on Modified Graphite Paper and in Situ Grown Copper Sulfide for Quantum Dot Sensitized Solar Cells. *ACS Appl. Energy Mater.* **2018**, *1* (3), 1355–1363. <https://doi.org/10.1021/acsaem.8b00075>.
- (37) Patil, R. S.; Lokhande, C. D.; Mane, R. S.; Pathan, H. M.; Joo, O.-S.; Han, S.-H. Successive Ionic Layer Adsorption and Reaction (SILAR) Trend for Nanocrystalline Mercury Sulfide Thin Films Growth. *Materials Science and Engineering: B* **2006**, *129* (1–3), 59–63. <https://doi.org/10.1016/j.mseb.2005.12.027>.
- (38) Sankapal, B. R.; Mane, R. S.; Lokhande, C. D. Successive Ionic Layer Adsorption and Reaction (SILAR) Method for the Deposition of Large Area (J10 Cm²) Tin Disulfide (SnS₂) Thin Films. *Materials Research Bulletin* **2000**, *9*.
- (39) Tschirner, N.; Lange, H.; Schliwa, A.; Biermann, A.; Thomsen, C.; Lambert, K.; Gomes, R.; Hens, Z. Interfacial Alloying in CdSe/CdS Heteronanocrystals: A Raman Spectroscopy Analysis. *Chem. Mater.* **2012**, *24* (2), 311–318. <https://doi.org/10.1021/cm202947n>.
- (40) Hofman, E.; Robinson, R. J.; Li, Z.-J.; Dzikovski, B.; Zheng, W. Controlled Dopant Migration in CdS/ZnS Core/Shell Quantum Dots. *J. Am. Chem. Soc.* **2017**, *139* (26), 8878–8885. <https://doi.org/10.1021/jacs.7b02320>.
- (41) Chern, M.; Nguyen, T. T.; Mahler, A. H.; Dennis, A. M. Shell Thickness Effects on Quantum Dot Brightness and Energy Transfer. *Nanoscale* **2017**, *9* (42), 16446–16458. <https://doi.org/10.1039/C7NR04296E>.
- (42) Zhang, H.; Ma, X.; Lin, Q.; Zeng, Z.; Wang, H.; Li, L. S.; Shen, H.; Jia, Y.; Du, Z. High-Brightness Blue InP Quantum Dot-Based Electroluminescent Devices: The Role of Shell Thickness. *J. Phys. Chem. Lett.* **2020**, *11* (3), 960–967. <https://doi.org/10.1021/acs.jpcclett.9b03567>.
- (43) Virieux, H.; Le Troedec, M.; Cros-Gagneux, A.; Ojo, W.-S.; Delpech, F.; Nayral, C.; Martinez, H.; Chaudret, B. InP/ZnS Nanocrystals: Coupling NMR and XPS for Fine Surface and Interface Description. *J. Am. Chem. Soc.* **2012**, *134* (48), 19701–19708. <https://doi.org/10.1021/ja307124m>.
- (44) Shen, W.; Tang, H.; Yang, X.; Cao, Z.; Cheng, T.; Wang, X.; Tan, Z.; You, J.; Deng, Z. Synthesis of Highly Fluorescent Inp/Zns Small-Core/Thick-Shell Tetrahedral-Shaped Quantum Dots for Blue Light-Emitting Diodes. *Journal of Materials Chemistry C* **2017**, *5* (32), 8243–8249. <https://doi.org/10.1039/C7TC02927F>.
- (45) Huang, K.; Demadrille, R.; Silly, M. G.; Sirotti, F.; Reiss, P.; Renault, O. Internal Structure of InP/ZnS Nanocrystals Unraveled by High-Resolution Soft X-Ray Photoelectron Spectroscopy. *ACS Nano* **2010**, *4* (8), 4799–4805. <https://doi.org/10.1021/nn100581t>.
- (46) Lee, Y. S.; Anderson, W. A. High - barrier Height Metal - insulator - semiconductor Diodes on *n* - InP. *Journal of Applied Physics* **1989**, *65* (10), 4051–4056. <https://doi.org/10.1063/1.343331>.
- (47) Stability of Sulfur-Treated InP Surface Studied by Photoluminescence and x-Ray Photoelectron

Spectroscopy. **1997**.

- (48) Granada-Ramirez, D. A.; Arias-Cerón, J. S.; Gómez-Herrera, M. L.; Luna-Arias, J. P.; Pérez-González, M.; Tomás, S. A.; Rodríguez-Fragoso, P.; Mendoza-Alvarez, J. G. Effect of the Indium Myristate Precursor Concentration on the Structural, Optical, Chemical Surface, and Electronic Properties of InP Quantum Dots Passivated with ZnS. *J Mater Sci: Mater Electron* **2019**, *30* (5), 4885–4894. <https://doi.org/10.1007/s10854-019-00783-6>.
- (49) Taylor, D. A.; Teku, J. A.; Cho, S.; Chae, W.-S.; Jeong, S.-J.; Lee, J.-S. Importance of Surface Functionalization and Purification for Narrow FWHM and Bright Green-Emitting InP Core–Multishell Quantum Dots via a Two-Step Growth Process. *Chem. Mater.* **2021**, *33* (12), 4399–4407. <https://doi.org/10.1021/acs.chemmater.1c00348>.
- (50) Cho, E.; Kim, T.; Choi, S.; Jang, H.; Min, K.; Jang, E. Optical Characteristics of the Surface Defects in InP Colloidal Quantum Dots for Highly Efficient Light-Emitting Applications. *ACS Appl. Nano Mater.* **2018**, *1* (12), 7106–7114. <https://doi.org/10.1021/acsanm.8b01947>.
- (51) Song, W.-S.; Lee, H.-S.; Lee, J. C.; Jang, D. S.; Choi, Y.; Choi, M.; Yang, H. Amine-Derived Synthetic Approach to Color-Tunable InP/ZnS Quantum Dots with High Fluorescent Qualities. *J Nanopart Res* **2013**, *15* (6), 1750. <https://doi.org/10.1007/s11051-013-1750-y>.
- (52) Xi, L.; Cho, D.-Y.; Duchamp, M.; Boothroyd, C. B.; Lek, J. Y.; Besmehn, A.; Waser, R.; Lam, Y. M.; Kardynal, B. Understanding the Role of Single Molecular ZnS Precursors in the Synthesis of In(Zn)P/ZnS Nanocrystals. *ACS Appl. Mater. Interfaces* **2014**, *6* (20), 18233–18242. <https://doi.org/10.1021/am504988j>.
- (53) Mastronardi, M. L.; Maier-Flaig, F.; Faulkner, D.; Henderson, E. J.; Kübel, C.; Lemmer, U.; Ozin, G. A. Size-Dependent Absolute Quantum Yields for Size-Separated Colloidally-Stable Silicon Nanocrystals. *Nano Lett.* **2011**, *12*, 337–342.
- (54) Gong, K.; Kelley, D. F. A Predictive Model of Shell Morphology in CdSe/CdS Core/Shell Quantum Dots. *J. Chem. Phys.* **2014**, *141* (19), 194704. <https://doi.org/10.1063/1.4901428>.
- (55) Daruka, I.; Barabási, A.-L. Dislocation-Free Island Formation in Heteroepitaxial Growth: A Study at Equilibrium. *Phys. Rev. Lett.* **1997**, *79*(19), 3708–3711. <https://doi.org/10.1103/PhysRevLett.79.3708>.
- (56) Janke, E. M.; Williams, N. E.; She, C.; Zhrebetsky, D.; Hudson, M. H.; Wang, L.; Gosztola, D. J.; Schaller, R. D.; Lee, B.; Sun, C.; Engel, G. S.; Talapin, D. V. Origin of Broad Emission Spectra in InP Quantum Dots: Contributions from Structural and Electronic Disorder. *J. Am. Chem. Soc.* **2018**, *140* (46), 15791–15803. <https://doi.org/10.1021/jacs.8b08753>.
- (57) de Jong, M.; Seijo, L.; Meijerink, A.; Rabouw, F. T. Resolving the Ambiguity in the Relation between Stokes Shift and Huang–Rhys Parameter. *Phys. Chem. Chem. Phys.* **2015**, *17* (26), 16959–16969. <https://doi.org/10.1039/C5CP02093J>.
- (58) Lange, H.; Artemyev, M.; Woggon, U.; Niermann, T.; Thomsen, C. Experimental Investigation of Exciton-LO-Phonon Couplings in CdSe/ZnS Core/Shell Nanorods. *Phys. Rev. B* **2008**, *77*(19), 193303.

<https://doi.org/10.1103/PhysRevB.77.193303>.

- (59) Cui, J.; Beyler, A. P.; Coropceanu, I.; Cleary, L.; Avila, T. R.; Chen, Y.; Cordero, J. M.; Heathcote, S. L.; Harris, D. K.; Chen, O.; Cao, J.; Bawendi, M. G. Evolution of the Single-Nanocrystal Photoluminescence Linewidth with Size and Shell: Implications for Exciton–Phonon Coupling and the Optimization of Spectral Linewidths. *Nano Lett.* **2016**, *16* (1), 289–296. <https://doi.org/10.1021/acs.nanolett.5b03790>.

Chapter 3: Low-Temperature PL Measurements of Coherent InP/ZnS Core-Shell QDs

3.1 Introduction

It has been shown that the bandgap and PL full width at half maximum (PL-FWHM) of semiconductor QDs depend on temperature separately from size-dependent characteristics¹. The temperature dependence of the QD is affected by the exciton-phonon interaction^{2,3}. Therefore, low-temperature PL measurements are very important for investigating PL mechanisms. In this session, we investigate the low-temperature PL characteristics of InP/ZnS with ZnS thicknesses of 3 ML and 6 ML. The relationship between the extent of PL-FWHM and the Stokes shift described in Chapter 2 is discussed with the influence of phonons.

3.2 Experimental

PL measurements were performed using a NanoLog Horiba Jovin Yvon spectrofluorometer with a 450 W xenon arc lamp, the same as in Chapter 2. Low-temperature PL measurements were performed using a cryostat, an accessory of a spectrofluorometer. The temperature was controlled in the range of 4 K to 300 K, and PL measurements were performed at each temperature. The QDs used were those of the same lot in Chapter 2, InP/ZnS QDs of 3 ML and 6 ML thickness of ZnS.

3.3 Results and discussion

For the optical properties in Chapter 3, we investigated the temperature dependence of the PL spectra of InP QDs coated with 3ML and 6ML of ZnS shell. In both samples, the PL spectra shifted to longer wavelengths as the temperature increased (Figure 3.1a and b), consistent with the behaviors of other semiconductor QDs³⁻⁵. It is established that the temperature dependence of the PL peak energies of semiconductor QDs follows the empirical Varshni relation^{6,7}. O'Donnell and Chen proposed the modified version, which includes a parameter of electron–phonon coupling and is given as:⁸

$$E_g(T) = E_g(0) - 2S\langle\hbar\omega\rangle\left(\exp\left(\frac{\langle\hbar\omega\rangle}{k_B T}\right) - 1\right)^{-1} \quad (3-1)$$

where $E_g(0)$ represents the bandgap at 0 K, S is the Huang–Rhys factor, $\langle\hbar\omega\rangle$ is the average phonon energy, and k_B is the Boltzmann constant. The decreasing curves of PL peak energies plotted as functions of temperature in Figure 3.2a and b are fitted well with eqn (3-1). Table 3.1 shows the parameters extracted from the fitting curves. The estimated average phonon energies $\langle\hbar\omega\rangle$ were 25.7 meV for the thinner-shelled QD and 24.4 meV for the thicker-shelled QD, respectively. Both values are smaller than the optical phonon energy for bulk InP (~ 42.8 meV),⁹ but nearly correspond with the longitudinal acoustic (LA) phonon energy for bulk InP (23.6 meV).^{1,10} The experimental values of the Huang–Rhys factor for the 6ML-covered QDs were smaller than that of the 3ML-covered QDs, suggesting that the electron–phonon coupling interaction is weakened for thicker shell-coated QDs. This is consistent with the decreasing trend of ΔE .

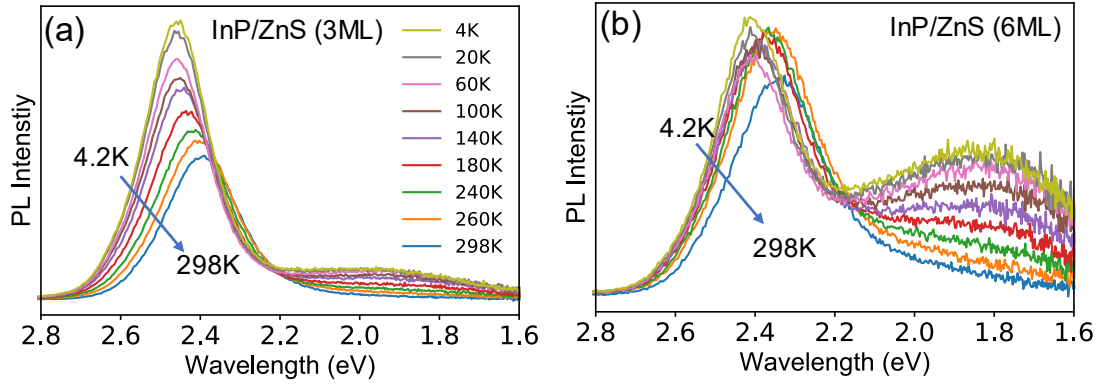


Figure 3.1. PL spectra as a function of temperature in the range from 4.2 to 298 K for the (a) InP/ZnS (3ML) core/shell QD and the (b) InP/ZnS (6ML) core/shell QD samples.

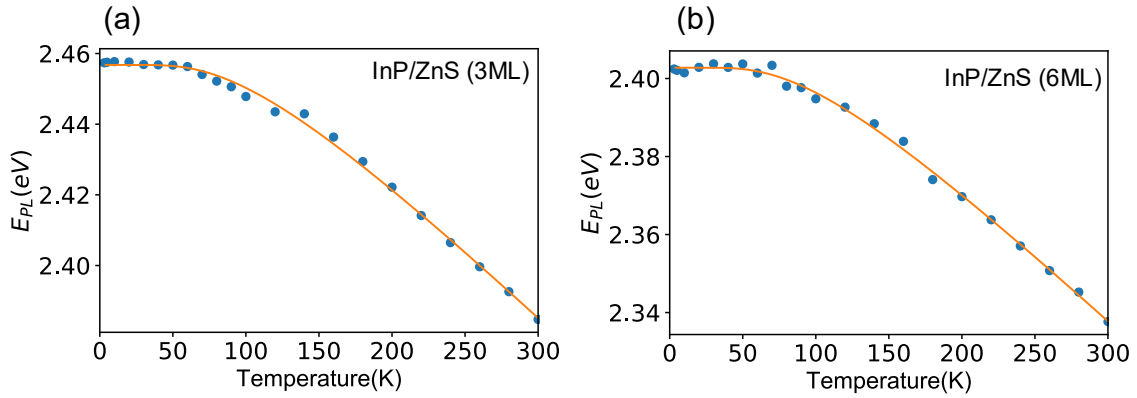


Figure 3.2. Changes of PL peak energies are plotted as a function of temperature for the QD samples, which are reproduced with the modified Varshni relation for the (a) InP/ZnS (3ML) core/shell QD and the (b) InP/ZnS (6ML) core/shell QD samples.

Table 3.1. Parameters obtained by fitting with eqn (3-1)

ZnS thickness (ML)	E_{PL} (eV)	S Huang–Rhys factor	Average phonon energy (meV)
3	2.46 ± 0.004	2.37 ± 0.09	25.7 ± 1.4
6	2.40 ± 0.004	2.09 ± 0.08	24.4 ± 1.4

We then investigated the temperature dependence of the PL bandwidth broadening to reveal the influence of the thick shell on its spectral features. Figure 3.3a and b show the plot of the measured values of the PL-FWHM of 3ML and 6ML-coated QD samples as functions of temperature, respectively. In both cases, the PL bandwidth increased monotonically as the temperature increased. The total bandwidth consisted of three components: inhomogeneous broadening (Γ_{inh}), which is independent of temperature, and two components originating from the acoustic and optical phonon–exciton interactions. The bandwidth is expressed as:²

$$\Gamma(T) = \Gamma_{inh} + \sigma T + \Gamma_{Lo} \left(\exp\left(\frac{E_{Lo}}{k_B T}\right) - 1 \right)^{-1} \quad (3-2)$$

where σ is the acoustic phonon–electron interaction coefficient, Γ_{Lo} represents the exciton–LO phonon coupling coefficient, E_{Lo} is the LO phonon energy, and k_B is the Boltzmann constant. Both curves were nicely fitted with function (3-2). Table 3.2 summarizes the parameters obtained from the best-fitting curves. The values of E_{Lo} nearly correspond with that of bulk InP.

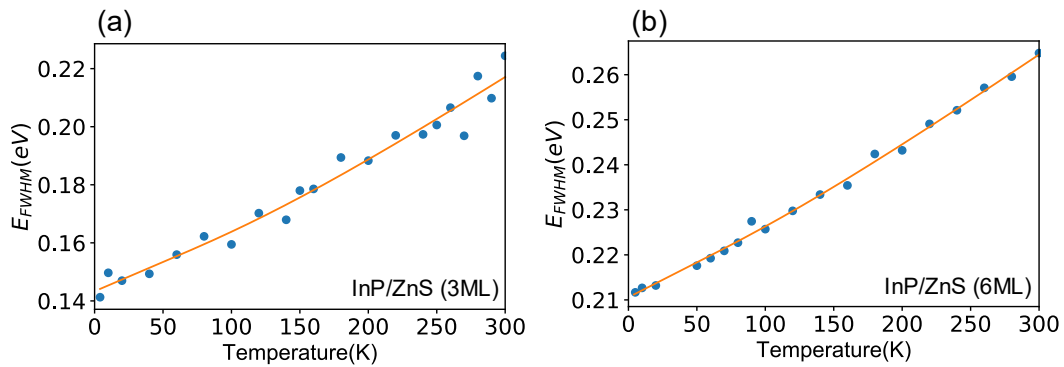


Figure 3.3. Temperature dependence of PL Bandwidth of InP QDs coated with (a) 3 ML- and (b) 6 ML ZnS reproduced by eq. (3 -2)

Table 3.2. Parameters obtained by fitting with eq. (3-2)

ZnS thickness (ML)	σ ($\mu\text{eV K}^{-1}$)	Γ_{Lo} (meV)	E_{Lo} (meV)	Γ_{inh} (meV)
3	200 ± 65	57.3 ± 137	42.8 ± 69	143 ± 0.003
6	154 ± 15	27.2 ± 26	39.4 ± 26	211 ± 0.007

Compared to a thinner shell, the thick shell coated QD had a larger value of Γ_{inh} . Thus, the results indicate that Γ_{inh} represents the inhomogeneous linewidth, which is independent of temperature but is influenced by fluctuations in the structure parameters such as elemental composition, shape, and size distribution¹¹. Indeed, the analysis of HAADF-STEM found that some of the 4ML-coated QDs began an anisotropic growth due to possible growth of a small island-like shape of the ZnS shell. According to the pioneering study reported by Dabbousi and coworkers, such small ZnS-islands coalesce as the thickness of the shell increases to form a continuous film on the core surface with a structure that has relaxed at the outer boundary to that of bulk ZnS (or decrease of the strain energy at the core/shell interface)^{12,13}, consistent with the observation results for the QDs coated with 4ML, 5ML and 6ML shells (**Figure 2.4c**, **Figure 2.5b**). On the assumption that the formation of grain boundaries as the islands coalesce could then be the origin of nonradiative recombination sites,¹² the decreasing trend of PLQY observed for the thicker ZnS shells could be also encouraged by increasing the number of nonradiative channels in the shell. This explanation is consistent with the relation between the decreasing trend of ΔE and the increasing FWHM. Consequently, a ZnS thick shell reduces the electron–phonon coupling strength while inhomogeneous shell growth ascribed to the large lattice mismatch might tune the growing morphology of the shell from flattened to island-like ones, resulting in the inhomogeneous broadening discrepancy.

3.4 Conclusions

The effect of shell thickness on optical properties was investigated in PL low-temperature measurements. Thick shells in ZnS reduce the electron-phonon coupling strength, but non-uniform shell growth changes the morphology in which the shells grow from flat to island-like. This non-uniform shell growth is the reason for the PL-FWHM broadening. Our results demonstrated herein suggest that the suppression of the inhomogeneous ZnS shell growth on monodisperse InP QDs is a key to achieve further narrowing of PL spectral linewidths.

References

- (1) Narayanaswamy, A.; Feiner, L. F.; Meijerink, A.; van der Zaag, P. J. The Effect of Temperature and Dot Size on the Spectral Properties of Colloidal InP/ZnS Core–Shell Quantum Dots. *ACS Nano* **2009**, *3* (9), 2539–2546. <https://doi.org/10.1021/nn9004507>.
- (2) Valerini, D.; Cretí, A.; Lomascolo, M.; Manna, L.; Cingolani, R.; Anni, M. Temperature Dependence of the Photoluminescence Properties of Colloidal CdSe / ZnS Core/Shell Quantum Dots Embedded in a Polystyrene Matrix. *Phys. Rev. B* **2005**, *71* (23), 235409. <https://doi.org/10.1103/PhysRevB.71.235409>.
- (3) Chon, B.; Bang, J.; Park, J.; Jeong, C.; Choi, J. H.; Lee, J.-B.; Joo, T.; Kim, S. Unique Temperature Dependence and Blinking Behavior of CdTe/CdSe (Core/Shell) Type-II Quantum Dots. *J. Phys. Chem. C* **2011**, *115* (2), 436–442. <https://doi.org/10.1021/jp109229u>.
- (4) Shirahata, N.; Nakamura, J.; Inoue, J.; Ghosh, B.; Nemoto, K.; Nemoto, Y.; Takeguchi, M.; Masuda, Y.; Tanaka, M.; Ozin, G. A. Emerging Atomic Energy Levels in Zero-Dimensional Silicon Quantum Dots. *Nano Lett.* **2020**, *20* (3), 1491–1498. <https://doi.org/10.1021/acs.nanolett.9b03157>.
- (5) Ji, C.; Zhang, Y.; Zhang, T.; Liu, W.; Zhang, X.; Shen, H.; Wang, Y.; Gao, W.; Wang, Y.; Zhao, J.; Yu, W. W. Temperature-Dependent Photoluminescence of Ag₂Se Quantum Dots. *J. Phys. Chem. C* **2015**, *119* (24), 13841–13846. <https://doi.org/10.1021/acs.jpcc.5b01030>.
- (6) Varshni, Y. P. TEMPERATURE DEPENDENCE OF THE ENERGY GAP IN SEMICONDUCTORS. *Physica (Amsterdam)* **1967**, *34* (1), 149–154. [https://doi.org/doi.org/10.1016/0031-8914\(67\)90062-6](https://doi.org/doi.org/10.1016/0031-8914(67)90062-6).
- (7) Ghosh, B.; Takeguchi, M.; Nakamura, J.; Nemoto, Y.; Hamaoka, T.; Chandra, S.; Shirahata, N. Origin of the Photoluminescence Quantum Yields Enhanced by Alkane-Termination of Freestanding Silicon Nanocrystals: Temperature-Dependence of Optical Properties. *Sci Rep* **2016**, *6* (1), 36951. <https://doi.org/10.1038/srep36951>.
- (8) O'Donnell, K. P.; Chen, X. Temperature Dependence of Semiconductor Band Gaps. *Appl. Phys. Lett.* **1991**, *58* (25), 2924–2926. <https://doi.org/10.1063/1.104723>.
- (9) Seong, M. J.; Mičić, O. I.; Nozik, A. J.; Mascarenhas, A.; Cheong, H. M. Size-Dependent Raman Study of InP Quantum Dots. *Appl. Phys. Lett.* **2003**, *82* (2), 185–187. <https://doi.org/10.1063/1.1535272>.
- (10) Narayanaswamy, A.; Feiner, L. F.; van der Zaag, P. J. Temperature Dependence of the Photoluminescence of InP/ZnS Quantum Dots. *J. Phys. Chem. C* **2008**, *112* (17), 6775–6780. <https://doi.org/10.1021/jp800339m>.
- (11) Cheng, O. H.-C.; Qiao, T.; Sheldon, M.; Son, D. H. Size- and Temperature-Dependent Photoluminescence Spectra of Strongly Confined CsPbBr₃ Quantum Dots. *Nanoscale* **2020**, *12* (24), 13113–13118. <https://doi.org/10.1039/D0NR02711A>.
- (12) Dabbousi, B. O.; Rodriguez-Viejo, J.; Mikulec, F. V.; Heine, J. R.; Mattoussi, H.; Ober, R.; Jensen, K. F.; Bawendi, M. G. (CdSe)ZnS Core–Shell Quantum Dots: Synthesis and Characterization of a Size Series of Highly Luminescent Nanocrystallites. *J. Phys. Chem. B* **1997**, *101* (46), 9463–9475.

<https://doi.org/10.1021/jp971091y>.

- (13) Ji, B.; Panfil, Y. E.; Waiskopf, N.; Remennik, S.; Popov, I.; Banin, U. Strain-Controlled Shell Morphology on Quantum Rods. *Nat Commun* **2019**, *10* (1), 2. <https://doi.org/10.1038/s41467-018-07837-z>.

Chapter 4: Impact of Coherent Core/Shell Architecture on Fast Response in InP-based Quantum Dot Photodiodes

4.1 Introduction

Colloidal quantum dots (QDs) have tunable excited states depending on their diameters based on the quantum confinement effect, and their excellent optical absorption and emission properties have attracted attention in a wide range of optoelectronic applications, including photodetectors,¹⁻³ solar cells,^{4,5} light-emitting diodes,^{6,7} and lasers.⁸ QD photodetectors have a device structure of primarily photodiodes or phototransistors and can be manufactured at low cost, offering significant advantages in surveying, night vision, optical communications, thermal sensing, and medical diagnostics.⁹ To date, the ultraviolet spectral range are covered by the QDs having central element of ZnO or ZnS,^{10,11} while counterparts of CsPbBr₃ and CdSe have been developed to cover the visible wavelength range.^{12,13} QDs of PbS, PbSe and CdSe_xTe_{1-x} dominate the optically active layers for near-infrared (NIR) light sensing.¹⁴⁻¹⁶ Group III-V compound semiconductors find various applications in optoelectronics for the reasons below.¹⁷⁻¹⁹ First, their high electron mobilities such as 78000 cm²/(V·s) for InSb,²⁰ 34000 cm²/(V·s) for InAs,²¹ 9400 cm²/(V·s) for GaAs,²¹ and 5200 cm²/(V·s) for InP²¹ are beyond the values of other semiconductors including Si (1450 cm²/V s),²² CdTe (804 cm²/V·s),²³ CdSe (642 cm²/V·s),²³ and CdS (642 cm²/V·s).²³ Second, Group III-V compound semiconductors (except for GaN, AlAs, AlSb, GaN and GaP) have low exciton binding energy,²⁴ making it easier to dissociate excitons and extract a net current from the device flow towards the corresponding electrodes for detection of photon. Third, the absorption and emission spectral tunability in a broad wavelength range is realized by controlled energy gap resulting from alloying of central elements of QDs or their size control.^{25,26} Fourth, III-V semiconductors are free of toxic heavy metals such as Cd, Pb, and Hg, making them an

attractive alternative materials platform for optoelectronic device applications.^{27,28} Nevertheless, compared to group II-VI semiconductor QDs, III-V counterparts have a higher ratio of covalent bond character against ionic bond one, making nanoparticle crystallization in the solution phase difficult and leaving challenges in their synthesis. InP QDs are the most well-studied nanocrystals among III-V family, but their application remains limited to the optically active layer of light-emitting diode.^{29,30} There are only a few reports of InP QDs applied to photoelectrodes, and until now, only two reports of phototransistor structures.^{31,32} Possible reasons are difficulty in (i) colloidal synthesis of powder form of InP QDs due to necessity of using highly chemical reactive precursors and unestablished postsynthetic purification and (ii) carrier mobility between InP QDs due to a large interparticle distance caused by the common capping ligand oleic acid (or oleylamine).³²⁻³⁵ Kwak and co-workers reported a hybrid phototransistor where InP QDs used as a light-absorbing layer while black phosphorus (BP) used as a transportation layer.³¹ In their study, the ligand exchange from oleylamine to 1,2ethanedithiol, which has a shorter alkyl length, and annealing at high temperature for InP QDs improved the charge injection of the photogenerated carriers from the QD layer to BP layer, leading to a high responsivity and detectivity, but slow speed with fall time of 120 msec. The slow response speed for fall time is a common problem of entire Cd-free QD photodetectors not limited to III-V counterparts.^{1,3,32}

Here we report, for the first time, a vertical III-V QD photodiode having a high-speed response of rise time of 4 msec and fall time of 9 msec even at a voltage bias of 0 V at room-temperature in ambient air. In this device structure, a coherent InP/ZnS core-shell QD as a light-absorbing layer, having a single lattice parameter was used. The lattice coherency allowed for a high carrier mobility throughout core/shell QD resulting from the emerging defect-less core/shell interface. Ligand-exchange strategy was developed, in which the

palmitic acid on the QD with shorter ligand, i.e., 6-Mercapto-1hexanol, leading to greatly improved quality of QD film by spin coating. Furthermore, the spatial separation of photogenerated excitons was realized by forming a type-II band alignment at the interface between the QD layer and Al-doped ZnO counterpart, resulting in a fast response at a single-digit millisecond scale.

4.2 Experimental

Reagents and Materials: Indium(III) acetate [$\text{In}(\text{Ac})_3$, 99.99%, Aldrich], zinc acetate [$\text{Zn}(\text{Ac})_2$, 99.99%, Aldrich], zinc oxide (ZnO, 99.999%, Aldrich), 1-octadecene (ODE, 90%, Aldrich), sulfur (99.98%, Aldrich), butylamine (99.5%, Aldrich), N,N-dimethylformamide (DMF, anhydrous, 99.8%, Aldrich) oleic acid (OA, 90%, Aldrich), trioctylphosphine (TOP, 97%, Aldrich), 1-dodecanethiol (DDT, >98%, Aldrich), tris (trimethylsilyl)-phosphine [$(\text{TMS})_3\text{P}$, 98% Strem Chemicals], palmitic acid (PA, 98%, Tokyo Chemical Industry), noctylamine (OAm, 98%, Tokyo Chemical Industry), 6-mercapto-1hexanol (MCH, 97%, Aldrich), and aluminium-doped zinc oxide ink (conductivity: 10^{-3} - 10^{-4} S/cm, viscosity <4 mPa.s, Aldrich) were used without further purification. Aluminium (Al) wire was purchased from the Nilaco corporation (Japan). The purity of argon gas was 99.999%. Using an oil rotary vacuum pump, the vacuum conditions of less than 60 Pa was used for degassing and argon gas purge.

Preparation of Zn-oleate: ZnO (2 mmol) and OA (8 mmol) were mixed with 10 mL ODE in a 50 mL three-necked flask. The temperature was measured using a thermocouple inserted directly into the flask from the one branch pipe. The other branch pipe was capped with a silicone rubber septum for injection of stainless-steel syringe needles. The flask was connected to the Schlenk line. At first, the system was purged five times with argon gas. The

mixture was degassed at 120°C for 2 hrs under vacuum conditions, and then the mixture was quickly heated in an argon flow to 290°C and kept for about 1hr until the mixed solution got a transparent for yielding Zn-oleate. The solution was then cooled down to a room temperature and stored in an argon-filled vial until the use.

Preparation of (TMS)₃P-TOP: (TMS)₃P (0.12 mmol) in hexane was dissolved in 1 mL of TOP at room temperature inside an argon-filled glovebox where the oxygen and water levels are continuously monitored to maintain both O₂ ≤ 1 ppm and H₂O ≤ 5 ppm. The mixture was gently stirred until becoming uniform solution. This step was performed in the day before the synthesis of InP QD.

Synthesis of InP QDs: 0.45 mmol of In (Ac)₃, 0.075 mmol of Zn (Ac)₂ and PA (0.5 mmol) were mixed with 6.3 mL of ODE in a 50 ml three-necked flask which is fixed to a Schlenk line with a reflux condenser. Degassing of the mixture was performed at 120°C for 12 hrs under vacuum conditions. The degree of vacuum was controlled at 30 Pa which was measured by the capacitance manometer (ULVAC, Japan). The flask was filled with argon and cooled down to room temperature. The (TMS)₃P-TOP was quickly injected into the flask in an argon flow, heated to 40°C under vacuum and kept for 10 min for evaporation of hexane. Then, the flask was refilled with argon, heated to 130 °C and kept for 15 min as suggested by Taylor et al.,³⁶ heated to 300°C within 7.5 min and kept for 3 min. After then, the flask was cooled down to room temperature, and stored in an argon filled vials.

Synthesis of coherent InP/ZnS core/shell QDs: In a typical synthesis, 8 mL of the InP QD solution, 250 μL DDT and 4 mL Zn oleate (1.6 mmol) were mixed with 2 mL ODE in another 50 mL three-necked flask. The mixture was degassed at room temperature for 30 min under vacuum. After then, the flask was filled with argon, heated in an argon flow to 230 °C and kept for 20 min. By successively repeating the previous step, the shell of ZnS was thickened.

Specifically, one more layer of ZnS shell was coated by injection of a mixture of 250 μ L DDT and 2 mL Zn oleate at 230°C, followed by heating to 240°C and solution was kept for 20 min. The reaction temperature was from 230 to 250 °C, in 10 °C increments. The span of time was commonly 20 min at every reaction temperature. At most we repeated the procedure of injection 2 times. After completing the formation of shell with predefined thickness, the solution was cooled down to 80°C, and then acetone was added for centrifugation for 10 min at 10,000 rpm. The InP/ZnS QDs precipitated was redispersed in acetone by centrifugation for 10 min at 10,000 rpm. The supernatant was discarded to collect the QDs. Finally, the InP/ZnS QDs were redispersed in 8mL ODE and stored in an argon-filled vials.

Ligand exchange: 8 mL ODE of InP/ZnS QDs was mixed with 0.5 mL MCH in another 50 mL three-necked flask. The mixture was purged five times with Ar gas at room temperature. After then, the mixture was heated to 100 °C and kept 1hr. The mixture was cooled down to room temperature. Next, the mixture was transferred to Ar-filled centrifugation tube. After addition of hexane as a poor solvent, the tube was subjected to centrifugation for 10 min at 9,000 rpm. The InP/ZnS QDs precipitated was redispersed in 2 mL ethanol while 4 mL hexane as a poor solvent was added. The mixture was centrifugated for 5 min at 9,000 rpm. This centrifugation process was repeated two times for washing the QDs. The supernatant was discarded to collect MCH-capped InP/ZnS QDs. The QDs were redispersed in DMF and stored in an argon-filled vials.

Fabrication of vertical-type photodiode: A 10×20 mm² rectangle soda-lime glass covered with 150 nm thick indium tin oxide (ITO) with a sheet resistance of 10–14 Ω /sq was used as the substrate. The ITO film was patterned by chemical etching (Zn powder and 37% HCl) into three narrow strips about 2 mm wide and 20 mm long. The patterned ITO substrates were washed in Milli-Q water of 18.2 M Ω ·cm resistivity for 15 min with ultrasonic cleaner,

followed by sonicated for 15 min in acetone, ethanol, isopropyl alcohol in that order. After drying, organic contaminants on the surface were removed by exposure to VUV light (Ushio Inc., Japan, UER20-172V; $\lambda = 172$ nm and 10 mW/cm²) for 30 min under a reduced pressure of 10^3 Pa and a N₂ flow, resulting in a super hydrophilic surface.

Next, the cleaned substrate was moved in a next step for fabrication of vertical-type photodiode with a multilayer device structure. Spin-coating and heating were performed in an Ar filled glove box to fabricate the multilayer films. The sample was then removed from the glove box, mounted in a sample holder, and vacuum evaporated to deposit an aluminum (Al) thin film that would serve as the electrode. Specifically, in first, Al-doped ZnO particle ink of $60 \mu\text{L}$ was spin-coated for 45 sec at 3000 rpm, followed by heating for 30 min at 160°C . Second, a $60 \mu\text{L}$ of the MCH-capped InP/ZnS ink, adjusted to a concentration of 50 mg/mL in DMF + butylamine (11:1, vol/vol) mixed solvent, was spin-coated on the Al: ZnO-coated substrate for 30 sec at 2000 rpm, followed by heating for 30 min at 80°C . Finally, an Al electrode was deposited. Pattern deposition was performed by adhering the stainless-steel mask to the substrate.

Characterization of InP/ZnS QDs: X-ray powder diffraction (XRD) pattern was measured on a MiniFlex 600 (Rigaku Corp., Japan). Samples were measured at an angular step of 0.02° (time per step: 1 s per step) using CuK α ($\lambda = 1.5418 \text{ \AA}$) radiation. The sample was observed on the JEOL JEM-ARM200F with STEM mode operating at 200 kV. The observation with the STEM offers an unprecedented opportunity to probe structures with sub-Angström resolution. The dark-field image was acquired with high-angle annular dark field (HAADF) detector. A low-pass filter was applied to the image for noise reduction. The attenuated total reflection Fourier transform infrared (ATR-FTIR) spectra were acquired using an FT/IR-4100 (JASCO, Japan). Optical absorption and emission properties were measured with

toluene solution of the QDs. Optical absorption spectra were recorded using a UV-vis spectrophotometer (JASCO V-650, Japan). Photoluminescence (PL) measurement was carried out using a modular double grating Czerny–Turner monochromator and an iHR 320 emission monochromator (1200 lines per mm of gratings) coupled to a photomultiplier tube (PMT) on a NanoLog Horiba Jovin Yvon spectrofluorometer with a 450 W xenon arc lamp. The spectral resolution of the system is around 0.3 nm. To avoid scattered excitation lights, a cut filter for 395 nm-light was placed in front of the monochromator-PMT setup. The absolute PL quantum yields (QYs) were measured at room temperature using the QY measurement system C9920-02 from Hamamatsu Photonics Co., Ltd with a 150 W xenon lamp coupled to a monochromator for wavelength discrimination, an integrating sphere as a sample chamber, and a multichannel analyzer for signal detection.

Device Characterization: All device testing was performed at room temperature under ambient conditions. Data for the current density–voltage (I–V) measurements were acquired using a Keithley 2425 source meter. A 300 W xenon lamp was used for illumination, with a bandpass filter passing only visible light at 470 ± 5 nm. In the I-V test, multiple devices on a substrate were measured individually and each device was characterized under 470 nm light irradiation, then under dark conditions (no illumination). No obvious differences were found due to light cycling or repeated measurements on the same device within a few months of the first test. Data for the responsivity measurement was collected on a home-built setup using illumination a same illumination source, modulated with optical chopper (#55-783, Edmund Optics). The anode and cathode of the device were connected to a 1 G Ω load resistor and connected to a DS-5624A oscilloscope (Iwatsu Electric Co., Ltd) to record the modulation changes of the photovoltage under open circuit conditions. The frequency response of the photocurrent was displayed as a fast Fourier transform by the oscilloscope. The response time

was calculated using the rise and fall times between 0.1 and 0.9, with the background of the waveform displayed on the oscilloscope as 0 and the maximum photocurrent as 1.

4.3 Results and discussion

We reported previously a new class of InP/ZnS core/shell QDs, where the lattice of InP QD as a core is compressed by 4.1% compared to the bulk crystal while the lattice of ZnS as a shell is expanded by 4.1% compared to the bulk crystal if the shell thickness is less than 0.81 nm (corresponding to three monolayers (3ML) of cubic ZnS) and the diameter of the core QD is less than 2.64 nm.³⁷ The resulting InP/ZnS core/shell QDs have a single lattice constant of 0.563 nm and provide a coherent and homogeneous interface despite the large lattice distortion between the core and the shell materials. In the present work, the coherent InP/ZnS core/shell QDs were used as a light-absorbing layer of the vertical photodiode. Figure 4.1 shows a summary of the results of structural and optical characterizations of the coherent InP/ZnS (3ML) core/shell QD terminated with PA monolayer. Panel (a) shows a typical XRD of the QD before and after shell formation. The XRD pattern of the InP core QD has peaks indexed to the (111), (220), and (311) planes of zincblende (cubic) bulk crystal of InP, respectively. After the 3ML shell formation, the relative shift of each XRD peak toward a higher diffraction angle side happens to give a lattice constant of 0.563 nm, indicating the successful formation of coherent core/shell structure unlike combined XRD pattern of InP and ZnS.³⁷ The peak at around 20° appears because of a ligand peak such as PA or OA as discussed later. In the post-synthesis of InP core QDs, the product was washed rigorously by ultracentrifugation with a mixture of hexane (i.e., good solvent) and methanol (i.e., poor solvent) as many as 10 times, but the peak was still present, suggesting that the PA adsorbs on the InP QD via ionic bind. As supported by Alivisatos and co-workers, this peak indicates

a bound and ordered capping ligand on the QD.³⁸ Panel (b) shows a typical HAADF-STEM image of InP/ZnS (3ML) QDs. As expected, we see QDs with a round shape unlike island-like shapes and the estimated diameter was $3.2\text{nm} \pm 0.3\text{ nm}$ which satisfies the conditions of core size the coherent core/shell structure forms.³⁷ Panels (c) and (d) show optical absorption and emission spectra of the InP core QD and the coherent core/shell QD, respectively. The first exciton peak in the UV-Vis spectrum was sharp and have a much steeper rise. The estimated value of its valley-depth [VD, defined as $1 - (\text{Abs}_{\text{min}} / \text{Abs}_{\text{max}})$] was 0.55, which is larger than those of the previous InP-based QDs exhibiting the green (VD = 0.51) and red emission (VD = 0.5),^{30,37} suggesting a much narrower size distribution. PL spectrum has two peaks at 517 nm and 680 nm and the former spectral linewidth (full width half maximum, FWHM) was 53 nm. The broad PL peak at 680 nm could be attributed to the emission originating from surface trap of indium dangling bonds.³⁹

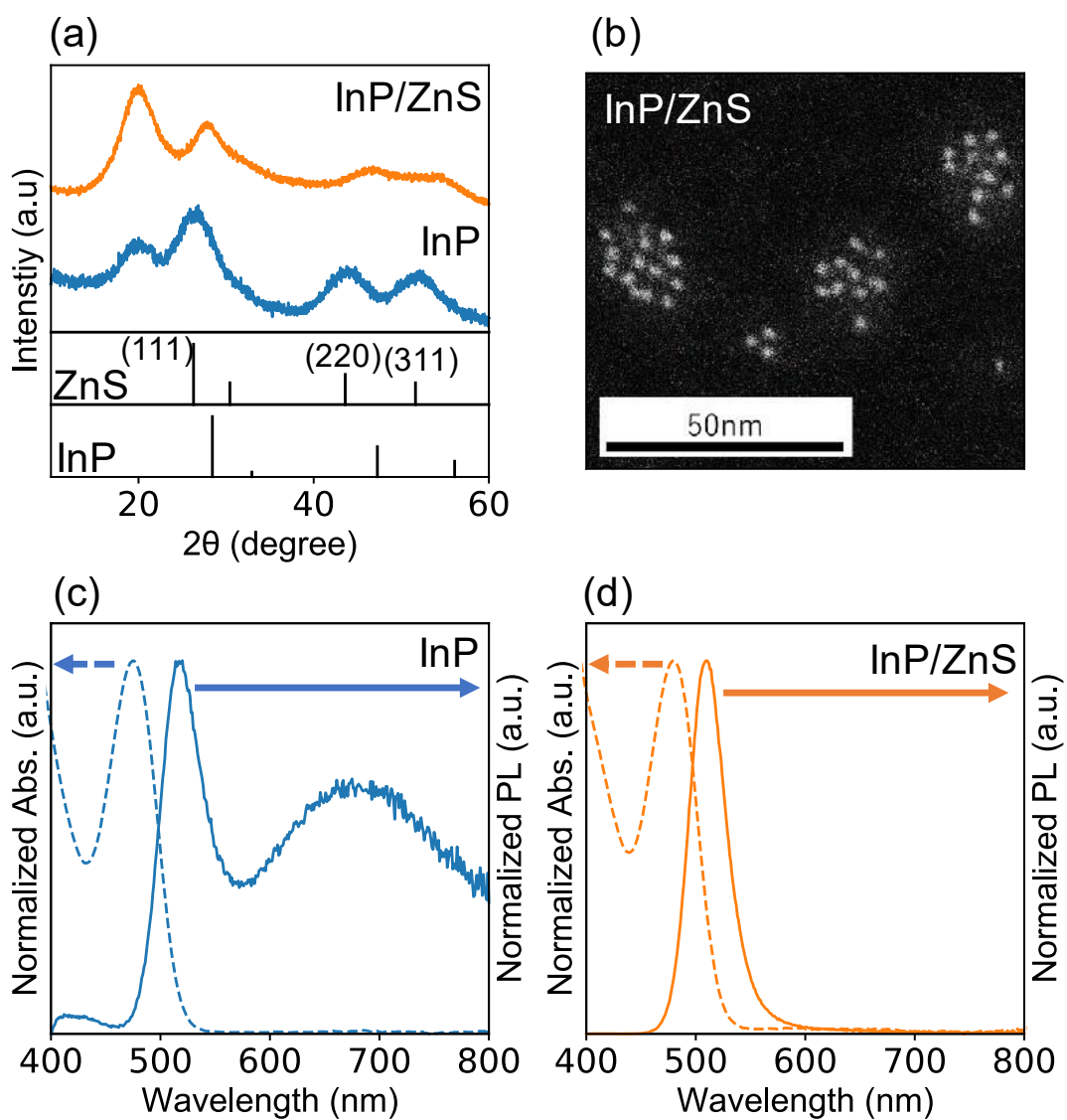


Figure 4.1. (a) XRD patterns of the core InP and the coherent InP/ZnS core/shell QDs capped with PA monolayers. Standard peak positions of InP and ZnS were assigned using ICDD PDF 00-032-0452 and 01-071-5975. (b) HAADF-STEM image of the coherent InP/ZnS core/shell QD capped with PA monolayers. UV-vis and PL spectra of (c) the core InP and (d) the coherent InP/ZnS core/shell QDs capped with PA monolayers.

As evidenced in the Panel (d), the PL peak at 680 nm disappears by encapsulating the core QD with the shell because of the passivation of the core surface, resulting in decrease of the dangling bonds. PL peak positions at 510 nm, and its FWHM is as narrow as 35 nm. PL quantum yield (QY) improved up to 70% due to the formation of defective-less interface between the InP core and the ZnS shell as described above. The value of VD was as high as 0.52 even after the 3ML shell formation, suggesting that the narrow size distribution was maintained.

In general, long-chain fatty acid or amine (i.e., oleylamine or oleic acid) is used in synthesis and works as a compact organic barrier bound to QDs, giving a colloidal stability. However, the long-chain ligands minimize carrier mobility between QDs by increased ligand induced resistance.^{32,35} Therefore, such long-chains are replaced with a short-chain ligand to narrow interparticle distance between neighboring QDs. Short-chain thiol monolayer is a common capping ligand.⁴⁰⁻⁴³ The sulfur head group of thiol ligand bonds to surface cation of QD with ionic strength stronger than the carboxyl head group of fatty acid.^{44,45} Beside, colloidal stability is also maintained.⁴⁶ Bai et al. reported that 6-mercapto-1-hexanol (MCH) as a capping ligand works to enhance device performance.⁴⁷ In this study, the PA ligand bound to the coherent InP/ZnS core/shell QD was replaced by MCH. As shown in Figure 4.2a, the PA-capped QDs dispersed in hexane phase transferred to ethanol phase due to the ligand exchange. The MCH-capped QDs were highly soluble in polar solvents such as DMF, but insoluble in non-polar solvents. The QDs capped with PA were sticky due to the presence of long alkyl chains, but ligand exchange yielded QDs in dry powder form (Figure 4.3). An XRD pattern shown in Figure 4.2b demonstrates that decrease in intensity of peak at $\sim 20^\circ$ due to substitution for the long-chain fatty acid with the short chain thiol. Figure 4.4 shows ATR-FTIR spectra of the QD samples before and after ligand exchange.

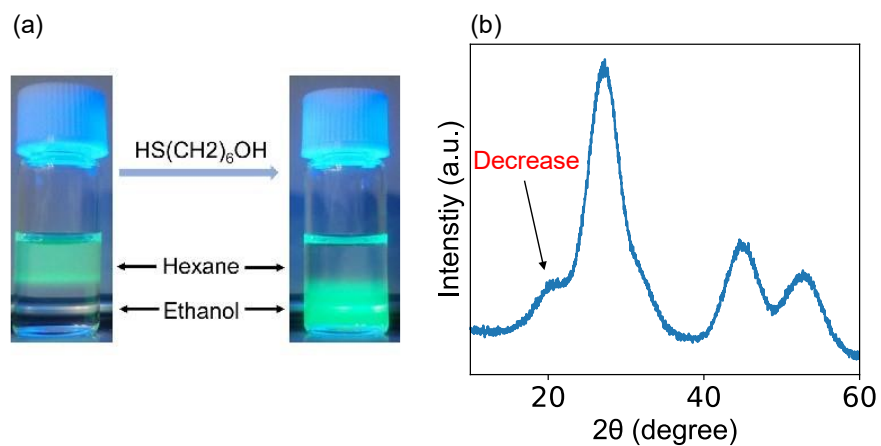


Figure 4.2. (a) Photograph of the colloidal dispersion of InP/ZnS QDs before and after ligand exchange. (b) XRD pattern of the InP/ZnS QD capped with MCH monolayer. The peak intensity at 20° decreased by the ligand exchange.

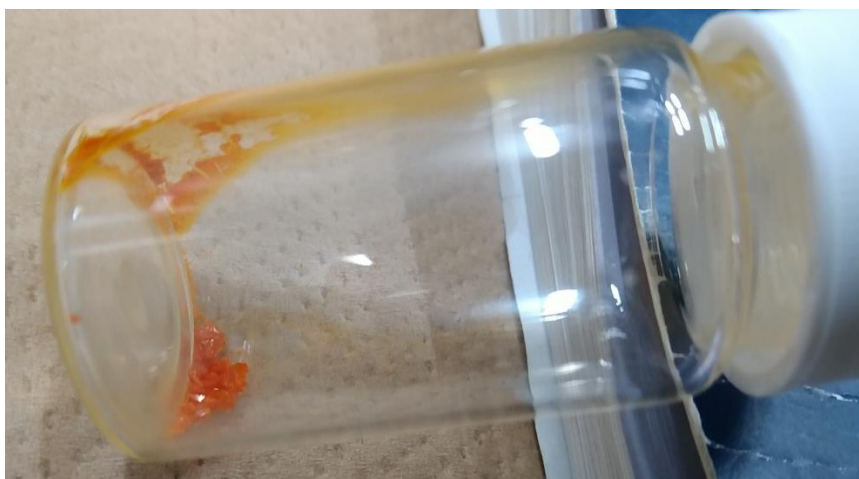


Figure 4.3. A typical digital photograph of the dried powder of the coherent InP/ZnS core/shell QDs capped with MCH monolayers.

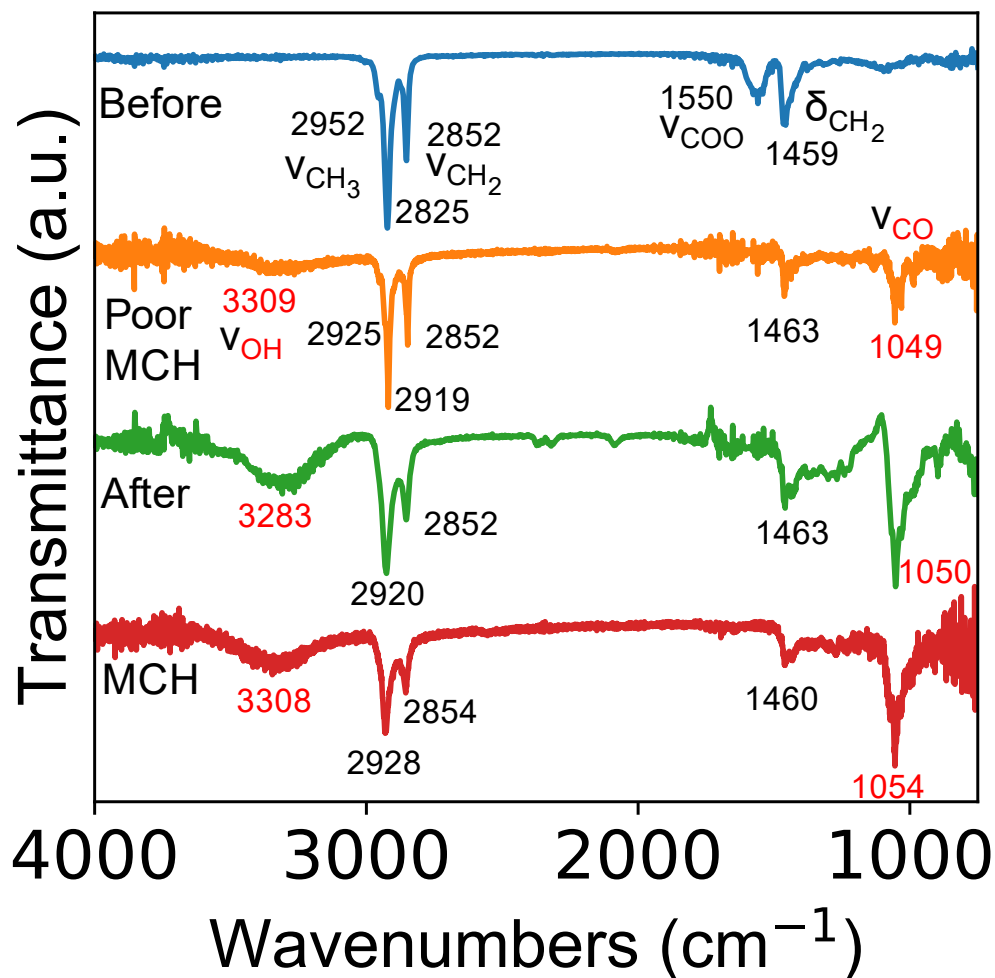


Figure 4.4. ATR-FTIR spectra of the InP/ZnS QD before (blue) and after ligand exchange (Green). Poor MCH means InP/ZnSQD with insufficient ligand (Orange), and MCH means undiluted ligand (Red).

After ligand exchange, a broad band centered at 3283 cm^{-1} , which is attributed to hydroxyl group of MCH ligand, appeared while the peak at 1550 cm^{-1} , which is attributed to the symmetric carboxylate stretching vibration band,⁴⁸ disappeared. The other peaks ($1000\text{-}1500\text{ cm}^{-1}$) of the MCH-capped sample were confirmed to originate from the MCH molecule,⁴⁷ indicating that the PA ligand was completely replaced by the MCH ligand. It is particularly

noted that the insufficient ligand exchange affects film deposition on ITO-covered substrates. As evidenced in Figure 4.5a, we could not obtain a uniform QD film by dropping QD ink with inadequate ligand exchange.

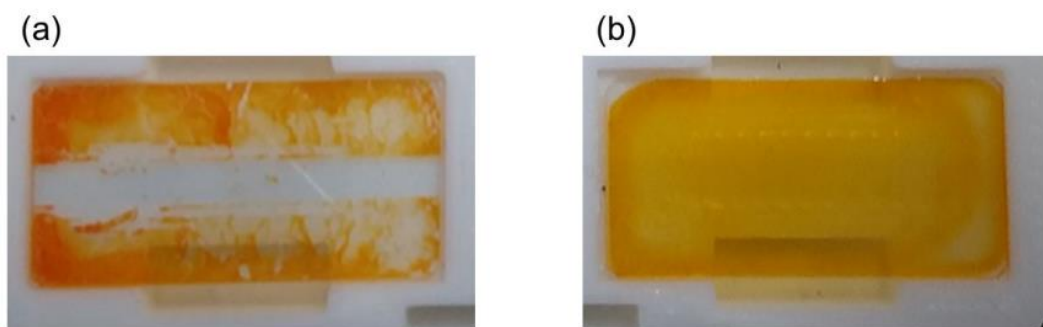


Figure 4.5. The representative digital photographs of the QD films prepared by dropping (a) oleate-capped QD dispersed in toluene and (b) MCH-capped QD dispersed in DMF on ITO-covered glass substrates. Unlike the oleate-capped QDs, the MCH-capped QDs could form a uniform and flat film on the ITO surface.

ATR-FTIR was used to examine whether the ligand exchange is sufficient or inadequate. When the ligand exchange was inadequate (see the orange spectrum, Figure 4.4c), the peak at 3283 cm^{-1} was weak. The decrease in QD film formability might be due to the aggregation of QDs caused by the difference in polarity of the ligands during the time between when the QD solution is dropped onto the substrate and when it completely dries. A similar aggregation was observed when ethanol was used instead of DMF. The results indicate that QD with both PA and MCH ligands causes the decrease in film formability.

As is predicted, the film formation was hindered when this QD ink was used for device fabrication (Figure 4.6). To avoid such a problem from arising, the PA-capped QDs were needed to be ultracentrifugally washed with acetone at least twice. The resultant PA-capped QDs were ligand-exchanged and used as a QD ink capable of uniform film formation for

device fabrication (Figure 4.5b). Hereafter, the coherent InP/ZnS QD capped with MCH is described by MCH-QD.

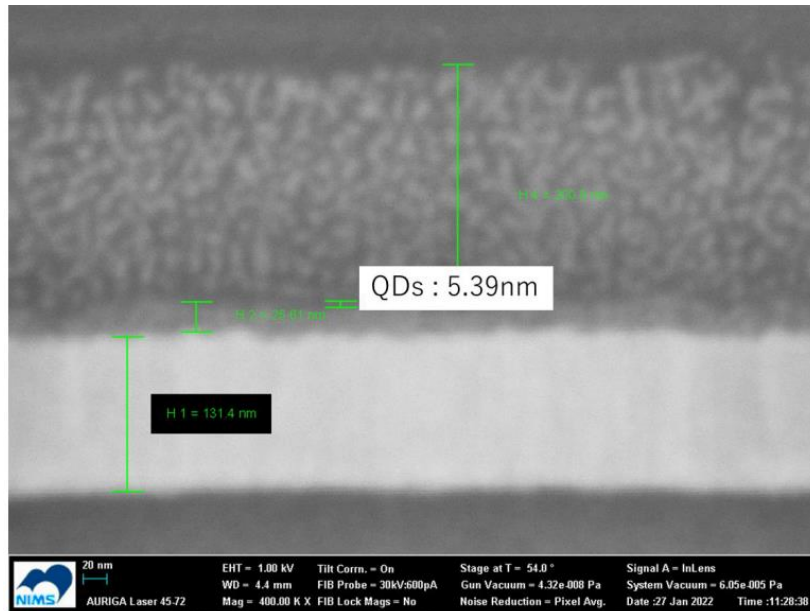


Figure 4.6. Cross-sectional SEM photographs of photodiode device with a multilayer structure of ITO/ZnO(Al)/poor MCH-InP/ZnS QD/Al. For the QD ink, MCH-capped InP/ZnS QD with inadequate ligand exchange was used. As is clearly seen in the image, we could not obtain the uniform film of QDs. Furthermore, it was difficult to obtain the QD film thicker than 5.39nm even by repeating the spin-coating process with the QD ink.

Figure 4.7 shows schematically shows the device architecture of photodiode in which the coherent InP/ZnS core/shell QD terminated with MCH ligand serves as an optically active layer, the energy band diagram in the voltage unbiased conditions and a cross-sectional SEM image. As shown in the Panel (Figure 4.7a), the device has an inorganic multilayer stack (i.e., ITO/Al-doped ZnO/MCH-QDs/Al). A 22.5 nm-thick Al-doped ZnO nanoparticle layer was deposited on ITO-covered soda-lime glass substrate by spin-coating method. Subsequently, a 100-nm thick MCH-QD layer was also formed by spin-coating method. Finally, a 209-nm Al layer was deposited by vacuum evaporation at 2.0×10^{-5} Pa. Panel (Figure 4.7b) shows the

proposed energy level diagram under a zero applied voltage bias. The values of work function of ITO and Al are taken from the literature.⁴⁹

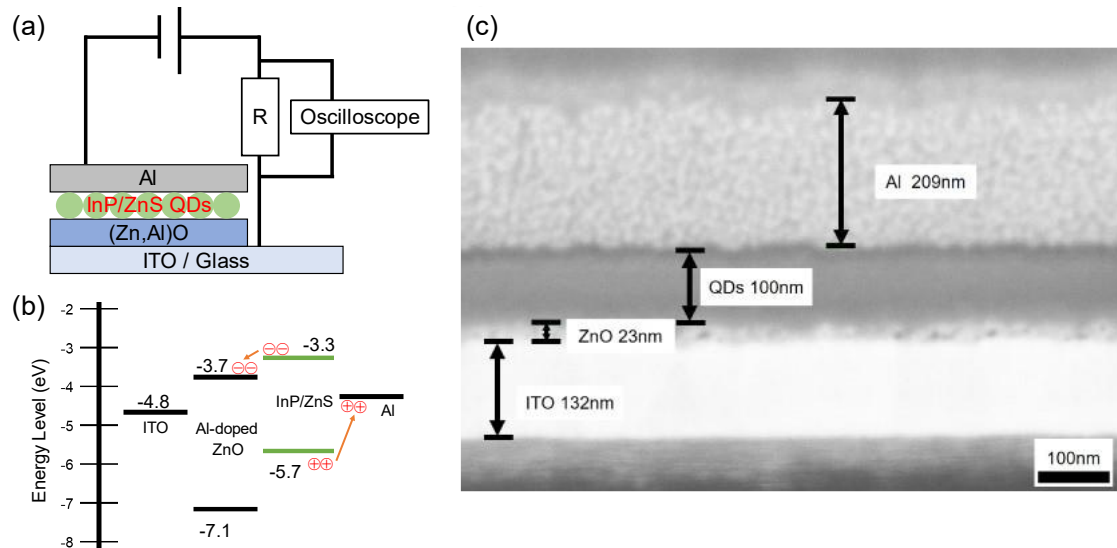


Figure 4.7. Device structure diagram of the MCH-QD film photodetector with an inorganic multi stack. (b) Energy band diagram in the unbiased conditions. (c) Cross-sectional SEM photographs of the multi stack of the device.

Based upon ultraviolet photoelectron spectroscopy (UPS) measurement of the spin-coated layer of Al-doped ZnO nanoparticles, the measured value of ionization energy was -7.12 eV (Figure 4.8a). The value of ionization energy for the MCH-QD layer, which was measured by photoelectron yield spectroscopy (PYS), was -5.7 eV (Figure 4.8b). The calculated value of electron affinity was -3.3 eV, assuming that the green photoemission originates from the fundamental optical gap of MCH-QDs. The Al-doped ZnO was inserted between the MCH-QD layer and the ITO electrode to create a type-II band alignment for exciton dissociation as depicted in the Panel (Figure 4.7b). Panel (Figure 4.7c) shows a cross-sectional SEM photograph of our QD-photodiode with a good device performance. Unlike the device shown

in Figure 4.6, 100-nm thick MCH-QD film is uniform and forms the flat heterogeneous interfaces. In this device structure, we did not use organics to avoid the possibility of holes during device operation which degrade the device performance,⁵⁰ leading to the long-running operation.

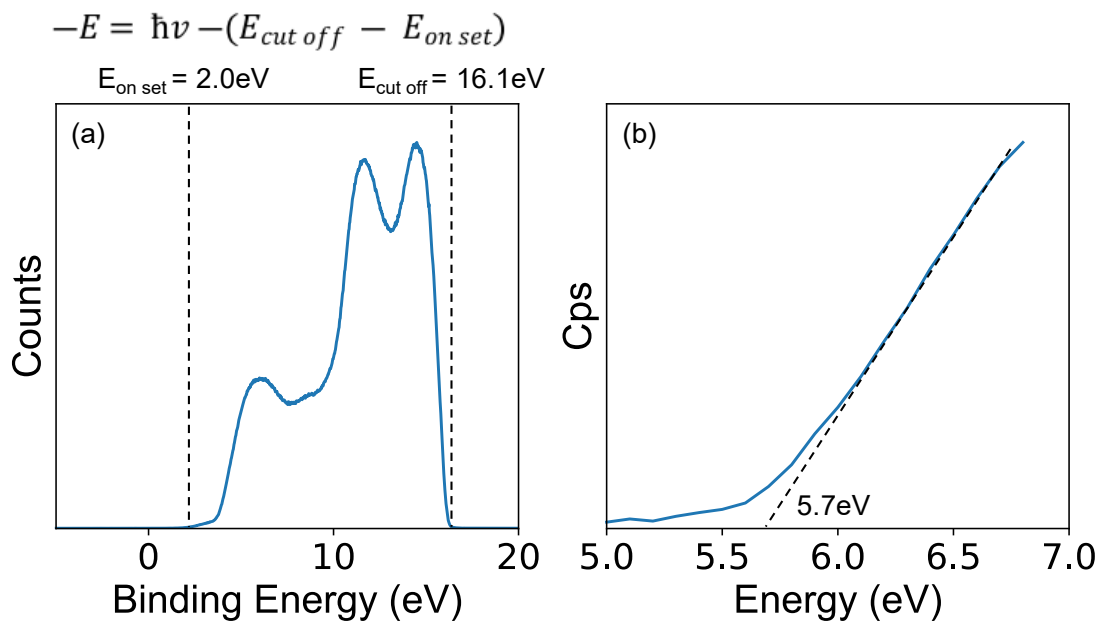


Figure 4.8. (a) Ultraviolet photoelectron spectroscopic (UPS) spectrum of the Al-doped ZnO spin-coated thin film plotted as a function of the energy and (b) Photoelectron yield spectroscopic (PYS) spectrum of a film form of the coherent InP/ZnS core/shell QDs capped with MCH ligands. The value of $\hbar\nu$ is 21.22 eV.

Device performances of the MCH-QD based photodiode measured in ambient air are summarized in Figure 4.9, Figure 4.10, Figure 4.11a and Figure 4.9(a) shows the room-temperature current-voltage curves under 470 ± 5 nm light irradiation. In a narrow measurement voltage ranged from -1.0 to 1.0 V, both forward and reverse scans were applied with steps of 0.02 V and a sweep time of 500 msec. Photocurrent generated was clearly

dependent of photon power of the irradiated light. Surprisingly, the photodiode also responded to even a weak light with photon power equivalent to 0.29 mW/cm^2 . Photocurrent generated under the 470 nm light irradiation at zero voltage bias when the light power density varies from 0 to 11 mW/cm^2 is shown in Figure 4.9(b). The photocurrent increases linearly with power density of the incident light.

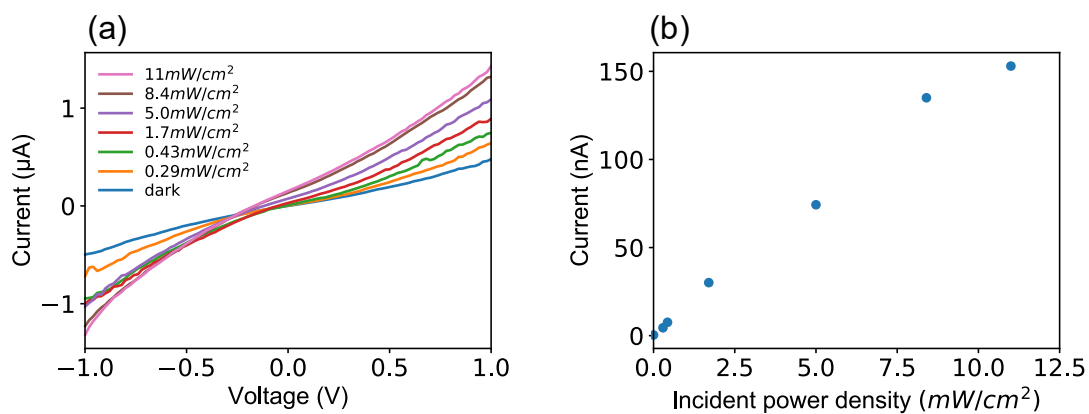


Figure 4.9. Summary of room-temperature device performances for the MCH-QD photodiode measured under $470 \pm 5 \text{ nm}$ light illumination at voltage bias of 0 V (except for (the Panels a and c) in ambient air. (a) Changes in photocurrent at different light power density when the voltage bias varies between -1.0 and 1.0 V . (b) Plots of photocurrent as a function of incident power density.

Figure 4.10(a) shows the responsivity of the device versus bias. Responsivity (R), a measure of the photocurrent generated per unit power of the incident light per unit area, was calculated by the equation: $R = I_p/P$,⁵¹ where I_p is a photocurrent subtracted by dark current, P is the incident light power density.

A trend of decreasing responsivity with increasing irradiation power density was observed, which might be due to saturation of responsivity at high photon power irradiation.⁵² The detectivity, denoted by D^* , was calculated by the equation: $D^* = R / (2 e I_{\text{dark}} / A)^{1/2}$, where e

is the electron charge, A is the effective surface area, the I_{dark} is the dark current, which is the main constituent of the shot noise current, respectively. As shown in Figure 4.10(b), when the incident-light power density varied from 0.1 to 11 mW/cm^2 at a bias of 1 V, the maxima of R and D^* values were 15.6 mA/W and 8×10^9 Jones ($1 \text{ Jones} = \text{cm Hz}^{1/2} \text{ W}^{-1}$) at the incident-light power density of 0.43 mW/cm^2 , respectively.

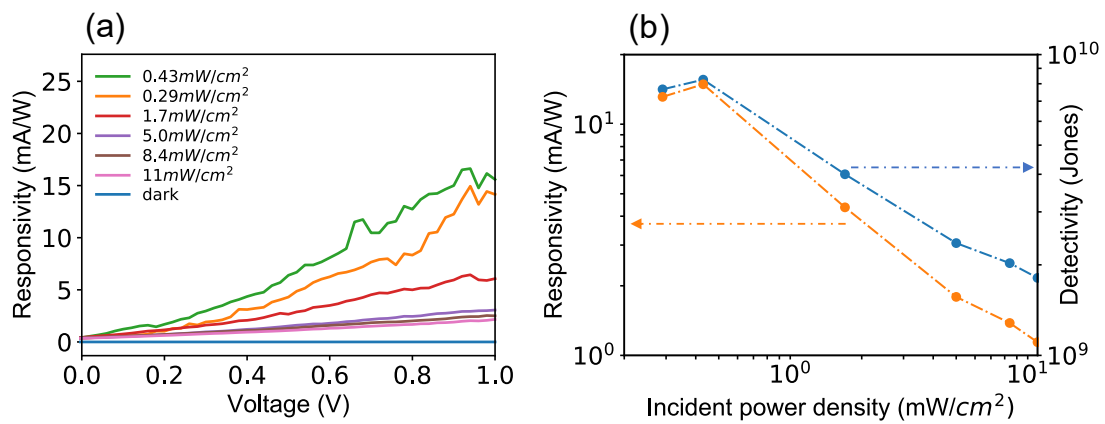


Figure 4.10. (a) Changes in responsivity with increasing light power density when a voltage bias varies between 0 and 1.0 V. (b) The light power density dependence of responsivity and detectivity.

Temporal response is a critical parameter for evaluation of device performance of photodiodes that need the ability to follow fast changing optical signals utilized in optical communications and image processing. In this study, the response speed was measured at a voltage bias of 0V under irradiation of 470-nm light with power density of 11 mW/cm^2 , where the turn on/off time of the incident light was switched using an optical chopper. As schematically illustrated in Figure 4.7(a), the photocurrent signals were recorded using an oscilloscope. A typical result of the time response curve is shown in Figure 4.11(a), where a quick and reproducible

photocurrent response and good cycling stability were observed even at a voltage bias of 0 V. Furthermore, the response profile exhibits that the measured rise time (τ_r : from 10% to 90% of the saturated value) and fall time (τ_f : from 90% to 10% of the peak value) are 4 msec and 9 msec, the fastest among the visible photodetectors based on Cd-free QDs and Pb-free perovskite nanocrystals. In Figure 4.11(b), the measured values of photocurrent are plotted when the incident light wavelength varied between 410 and 530 nm. The measurement was performed at a voltage bias of 0 V and the power density was fixed at 10 mW/cm². A representative optical absorption spectrum of the MCH-QD is superimposed on the plots to assert the incident-light wavelength selectivity of the photodiode. The photocurrent reached a maximum value for light irradiation at 470 nm, decreased at longer wavelengths, and was below the detection limit when the light of 530 nm or longer was irradiated. As expected, the trend of photocurrent generated as a function of irradiation-light wavelength was similar to the UV-vis behavior of the MCH-QD, suggesting that a wavelength selectivity of light detection can be tuned by QD size.

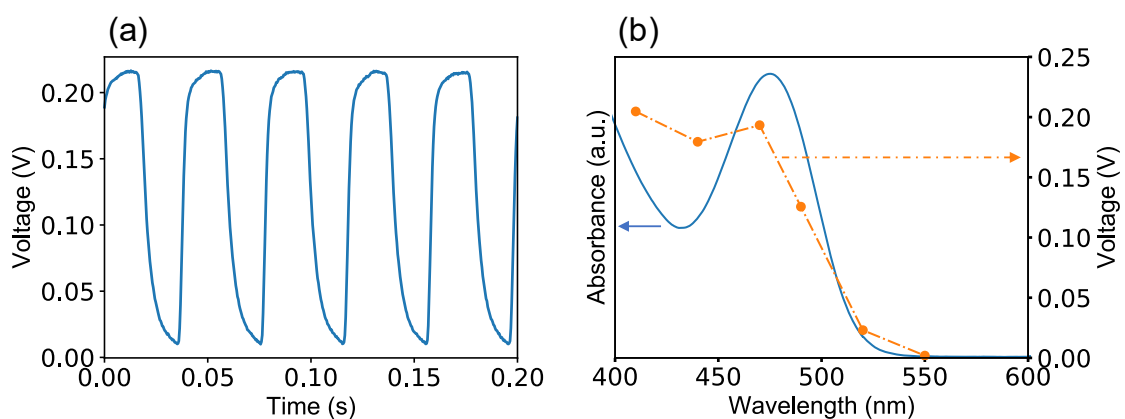


Figure 4.11. (a) A typical time response curve of photocurrent. (b) Plots of photocurrent at different wavelengths of incident light superimposed on the UV-vis spectrum of MCH-QD. The power densities of the incident lights were fixed at 10 mW/cm² for the Panels (a) and (b).

It is known that a good long-term optical switching behavior has still been a challenge for QD photodiodes. In this study, I-V measurements in the bias ranging between -1 and 1 V were repeated 100 times under irradiation of 470-nm light of 10 mW/cm². During this running test, we observed good I-V characteristics for each repeating times as presented in Figure 4.12(a). The I-V measurements were repeated many times with no change in device performance such as responsivity, waveform and response time as evidenced in Figure 4.12(b). Clearly shown in the inset, the current reversibly switches between high and low conductance with high stability and reproducibility even after 100 times as the light is turned on and off, indicating the successful long-term operation due to device stability.

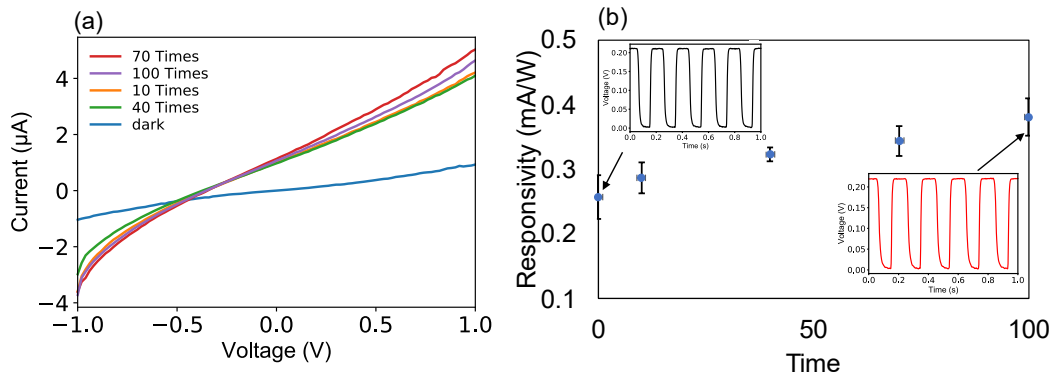


Figure 4.12. Device lifetime of the MCH-QD based photodiode measured at a voltage bias of 0 V at room temperature in ambient air using a 470 ± 5 nm light with power density of 10 mW/cm². Variation of (a) photocurrent and (b) responsivity at different number of measurements. Time response curves as insets were measured at 1st time and 100th times. Error bars were obtained as a standard deviation by measuring 10 samples.

To date, Cd-free QDs and Pb-free perovskite nanocrystals have been developed to serve as light-absorbing layers in photodiodes and phototransistors (see Table 4.1), but they have faced the barrier of slow response time of several hundred milliseconds scale (especially, fall time).^{31,32,53-55} There are two possible reasons for the fast photo responses at a single millisecond level in this work (Figure 4.11a). First, the ligand exchange enabled us to prepare a flat film thicker than 100 nm by repeated spin-coating. Furthermore, the molecular replacement with MCH ligands alters the interparticle dielectric environment as well as tunneling distance, possibly leading to the enhanced carrier mobility. Second, we expected that the coherent core/shell QD structure contributes the efficient dissociation of carriers generated in InP QD. In this core/shell structure, the 3ML shell is thin enough for traversing the charge carriers from the core QD to the ZnS layer through a slope of energy gradient at this junction. In addition, the emergent defect-less interface between the core and the shell allows that the photogenerated carriers could spread over the entire core/shell QD. The reduction of defects at heterogeneous interfaces leads to faster response time.⁹ By utilizing the type-II band alignment between Al-doped ZnO and the ZnS layers, electrons and holes could separate on ultrafast time scales for detections.

There is still room to further optimize the device structure to improve the detectivity or responsivity which were inferior to Cd based photodiodes. To enhance the carrier dissociation at the heterogeneous interfaces, the electron transportation layer should be replaced by a thicker film while blocking the electron leakage from the light-absorbing layer is needed. Further improving the quality of the light-absorbing layer can be realized by atom capping of the core/shell QD surface and such a surface engineering is a worthy challenge for further improving device performance.

Table 4.1. List of device performances of photodiodes (PD), Photoconductor (PC) and phototransistors (PT) reported in literatures to compare our work.

Material	Wavelength (nm)	Structure	Rise (ms)	Fall (ms)	Detectivity (Jones)	Responsivity (A/W)	Ref.
InP QDs / Black Phosphorus	405	PT	5	120	4.5×10^{16}	1×10^9	31
InP QD	650	PT	-	-	-	-	32
SnS ₂ QD / MoS ₂	UV-NIR	PT	100	100	4.75×10^{13}	278	54
ZnO-QDs / MoS ₂	635	PT	1500	1100	1.05×10^{11}	0.084	55
Bi ₂ S ₃ Nanocrystals	UV-NIR	PC	23	23	-	20	56
This work	470	PD	4	9	8.0×10^9	0.016	-

4.4 Conclusions

Bulk crystals of group III-V semiconductors including GaN, InP, InAs and InSb have superior electronic properties such as high electron mobility. Their QDs allow size-dependent tuning of the first exciton peak in the optical absorption spectrum on the basis of the effect of the quantum confinement. Thus, it is expected that the wavelength-selective photodetection is realized using the QDs (as the light absorbing layers) of (i) InAs and InSb for the NIR-SWIR light, (ii) InP for the visible light, and (iii) GaN for the UV light. Nevertheless, few papers have reported photodetectors using their QDs as light absorbing layers. In the previous paper, we reported the colloidal synthetic conditions to create a coherent InP/ZnS core/shell QD structure with a single lattice constant of 0.56 nm. We found in this work that the coherent core/shell QD as a light absorbing layer works to fabricate a good vertical-type photodiode that could be operated at room temperature in ambient air, showing the fast speed response at single-digit millisecond scale (i.e., $\tau_r / \tau_f = 4/9$ msec). Furthermore, this device operated in the photovoltaic mode of the photodiode circuit (i.e., 0 V voltage bias), unlike the phototransistors that requires a power source to operate. 55 The finding of the coherent InP/ZnS core-shell QDs working as a photosensitive layer of the QD photodiode suggests that other combinations of core and shell work giving a fast response speed for photo detection.

References

- (1) Zhao, T.; Oh, N.; Jishkariani, D.; Zhang, M.; Wang, H.; Li, N.; Lee, J. D.; Zeng, C.; Muduli, M.; Choi, H.-J.; Su, D.; Murray, C. B.; Kagan, C. R. General Synthetic Route to High-Quality Colloidal III-V Semiconductor Quantum Dots Based on Pnictogen Chlorides. *J. Am. Chem. Soc.* **2019**, *141* (38), 15145–15152. <https://doi.org/10.1021/jacs.9b06652>.
- (2) Leemans, J.; Pejović, V.; Georgitzikis, E.; Minjauw, M.; Siddik, A. B.; Deng, Y.; Kuang, Y.; Roelkens, G.; Detavernier, C.; Lieberman, I.; Malinowski, P. E.; Cheyuns, D.; Hens, Z. Colloidal III-V Quantum Dot Photodiodes for Short - Wave Infrared Photodetection. *Advanced Science* **2022**, *9* (17), 2200844. <https://doi.org/10.1002/advs.202200844>.
- (3) He, M.; Xu, Z.; Zhang, S.-W.; Zhang, M.; Wu, C.; Li, B.; Li, J.; Wang, L.; Zhao, S.; Kang, F.; Wei, G. Colloidal InSb Quantum Dots/Organic Integrated Bulk Heterojunction for Fast and Sensitive Near-Infrared Photodetectors. *Advanced Photonics Research* **2022**, 2100305. <https://doi.org/10.1002/adpr.202100305>.
- (4) Song, J. H.; Choi, H.; Pham, H. T.; Jeong, S. Energy Level Tuned Indium Arsenide Colloidal Quantum Dot Films for Efficient Photovoltaics. *Nat Commun* **2018**, *9* (1), 4267. <https://doi.org/10.1038/s41467-018-06399-4>.
- (5) Yang, S.; Zhao, P.; Zhao, X.; Qu, L.; Lai, X. InP and Sn:InP Based Quantum Dot Sensitized Solar Cells. *J. Mater. Chem. A* **2015**, *3* (43), 21922–21929. <https://doi.org/10.1039/C5TA04925C>.
- (6) Li, H.; Zhang, W.; Bian, Y.; Ahn, T. K.; Shen, H.; Ji, B. ZnF₂-Assisted Synthesis of Highly Luminescent InP/ZnSe/ZnS Quantum Dots for Efficient and Stable Electroluminescence. *Nano Lett.* **2022**, *22* (10), 4067–4073. <https://doi.org/10.1021/acs.nanolett.2c00763>.
- (7) Ghosh, B.; Yamada, H.; Chinnathambi, S.; Özbilgin, İ. N. G.; Shirahata, N. Inverted Device Architecture for Enhanced Performance of Flexible Silicon Quantum Dot Light-Emitting Diode. *The Journal of Physical Chemistry Letters* **2018**, *9* (18), 5400–5407. <https://doi.org/10.1021/acs.jpcllett.8b02278>.
- (8) Jung, H.; Ahn, N.; Klimov, V. I. Prospects and Challenges of Colloidal Quantum Dot Laser Diodes. *Nat. Photon.* **2021**, *15* (9), 643–655. <https://doi.org/10.1038/s41566-021-00827-6>.
- (9) Guo, R.; Zhang, M.; Ding, J.; Liu, A.; Huang, F.; Sheng, M. Advances in Colloidal Quantum Dot-Based Photodetectors. *J. Mater. Chem. C* **2022**, *10* (19), 7404–7422. <https://doi.org/10.1039/D2TC00219A>.
- (10) Guo, D.-Y.; Shan, C.-X.; Qu, S.-N.; Shen, D.-Z. Highly Sensitive Ultraviolet Photodetectors Fabricated from ZnO Quantum Dots/Carbon Nanodots Hybrid Films. *Sci Rep* **2015**, *4* (1), 7469. <https://doi.org/10.1038/srep07469>.
- (11) Kan, H.; Zheng, W.; Lin, R.; Li, M.; Fu, C.; Sun, H.; Dong, M.; Xu, C.; Luo, J.; Fu, Y.; Huang, F. Ultrafast Photovoltaic-Type Deep Ultraviolet Photodetectors Using Hybrid Zero-/Two-Dimensional Heterojunctions. *ACS Appl. Mater. Interfaces* **2019**, *11* (8), 8412–8418. <https://doi.org/10.1021/acsami.8b20357>.
- (12) Shen, K.; Xu, H.; Li, X.; Guo, J.; Sathasivam, S.; Wang, M.; Ren, A.; Choy, K. L.; Parkin, I. P.; Guo, Z.;

- Wu, J. Flexible and Self - Powered Photodetector Arrays Based on All - Inorganic CsPbBr₃ Quantum Dots. *Adv. Mater.* **2020**, *32* (22), 2000004. <https://doi.org/10.1002/adma.202000004>.
- (13) Kim, J.; Kwon, S.-M.; Kang, Y. K.; Kim, Y.-H.; Lee, M.-J.; Han, K.; Facchetti, A.; Kim, M.-G.; Park, S. K. A Skin-like Two-Dimensionally Pixelized Full-Color Quantum Dot Photodetector. *Sci. Adv.* **2019**, *5* (11), eaax8801. <https://doi.org/10.1126/sciadv.aax8801>.
- (14) Wei, Y.; Ren, Z.; Zhang, A.; Mao, P.; Li, H.; Zhong, X.; Li, W.; Yang, S.; Wang, J. Hybrid Organic/PbS Quantum Dot Bilayer Photodetector with Low Dark Current and High Detectivity. *Adv. Funct. Mater.* **2018**, *28* (11), 1706690. <https://doi.org/10.1002/adfm.201706690>.
- (15) Sarasqueta, G.; Choudhury, K. R.; Subbiah, J.; So, F. Organic and Inorganic Blocking Layers for Solution-Processed Colloidal PbSe Nanocrystal Infrared Photodetectors. *Adv. Funct. Mater.* **2011**, *21* (1), 167–171. <https://doi.org/10.1002/adfm.201001328>.
- (16) Shen, T.; Li, B.; Zheng, K.; Pullerits, T.; Cao, G.; Tian, J. Surface Engineering of Quantum Dots for Remarkably High Detectivity Photodetectors. *J. Phys. Chem. Lett.* **2018**, *9* (12), 3285–3294. <https://doi.org/10.1021/acs.jpcclett.8b01255>.
- (17) Mokkaṡpati, S.; Jagadish, C. III-V Compound SC for Optoelectronic Devices. *Materials Today* **2009**, *12* (4), 22–32. [https://doi.org/10.1016/S1369-7021\(09\)70110-5](https://doi.org/10.1016/S1369-7021(09)70110-5).
- (18) Wen, P.; Tiwari, P.; Mauthe, S.; Schmid, H.; Sousa, M.; Scherrer, M.; Baumann, M.; Bitachon, B. I.; Leuthold, J.; Gotsmann, B.; Moselund, K. E. Waveguide Coupled III-V Photodiodes Monolithically Integrated on Si. *Nat Commun* **2022**, *13* (1), 909. <https://doi.org/10.1038/s41467-022-28502-6>.
- (19) Dai, X.; Zhang, S.; Wang, Z.; Adamo, G.; Liu, H.; Huang, Y.; Couteau, C.; Soci, C. GaAs/AlGaAs Nanowire Photodetector. *Nano Lett.* **2014**, *14* (5), 2688–2693. <https://doi.org/10.1021/nl5006004>.
- (20) Liu, W.; Chang, A. Y.; Schaller, R. D.; Talapin, D. V. Colloidal InSb Nanocrystals. *J. Am. Chem. Soc.* **2012**, *134* (50), 20258–20261. <https://doi.org/10.1021/ja309821j>.
- (21) Sotoodeh, M.; Khalid, A. H.; Rezazadeh, A. A. Empirical Low-Field Mobility Model for III–V Compounds Applicable in Device Simulation Codes. *Journal of Applied Physics* **2000**, *87* (6), 2890–2900. <https://doi.org/10.1063/1.372274>.
- (22) Bandstructure and Related Properties. In *Semiconductors and Semimetals*; Elsevier, 2003; Vol. 74, pp 91–145. [https://doi.org/10.1016/S0080-8784\(03\)80018-2](https://doi.org/10.1016/S0080-8784(03)80018-2).
- (23) Dutta, A.; Mukherjee, M. K.; Mukhopadhyay, D. Some Empirical Relations for Electron Mobility in II–VI Compound Semiconductors. *Czech J Phys* **1991**, *41* (5), 474–483. <https://doi.org/10.1007/BF01597951>.
- (24) Madelung, O.; Rössler, U.; Schulz, M. *Semiconductors · Group IV Elements, IV-IV and III-V Compounds. Part b - Electronic, Transport, Optical and Other Properties*; Springer Materials, 2002; Vol. 41A1 β .
- (25) Kirkwood, N.; De Trizio, L.; Hoekstra, A. W.; Kleibergen, L.; Renaud, N.; Koole, R.; Baesjou, P.; Manna, L.; Houtepen, A. J. Ga for Zn Cation Exchange Allows for Highly Luminescent and Photostable InZnP-

- Based Quantum Dots. *Chemistry of Materials* **2017**, *29* (12), 5192–5199. <https://doi.org/10.1021/acs.chemmater.7b00848>.
- (26) Dong, C.; Liu, S.; Barange, N.; Lee, J.; Pardue, T.; Yi, X.; Yin, S.; So, F. Long-Wavelength Lead Sulfide Quantum Dots Sensing up to 2600 Nm for Short-Wavelength Infrared Photodetectors. *ACS Appl. Mater. Interfaces* **2019**, *11* (47), 44451–44457. <https://doi.org/10.1021/acsami.9b16539>.
- (27) Soenen, S. J.; Manshian, B. B.; Aubert, T.; Himmelreich, U.; Demeester, J.; De Smedt, S. C.; Hens, Z.; Braeckmans, K. Cytotoxicity of Cadmium-Free Quantum Dots and Their Use in Cell Bioimaging. *Chem. Res. Toxicol.* **2014**, *27* (6), 1050–1059. <https://doi.org/10.1021/tx5000975>.
- (28) Yarema, M.; Kovalenko, M. V. Colloidal Synthesis of InSb Nanocrystals with Controlled Polymorphism Using Indium and Antimony Amides. *Chem. Mater.* **2013**, *25* (9), 1788–1792. <https://doi.org/10.1021/cm400320r>.
- (29) Zhang, H.; Ma, X.; Lin, Q.; Zeng, Z.; Wang, H.; Li, L. S.; Shen, H.; Jia, Y.; Du, Z. High-Brightness Blue InP Quantum Dot-Based Electroluminescent Devices: The Role of Shell Thickness. *J. Phys. Chem. Lett.* **2020**, *11* (3), 960–967. <https://doi.org/10.1021/acs.jpcclett.9b03567>.
- (30) Won, Y.-H.; Cho, O.; Kim, T.; Chung, D.-Y.; Kim, T.; Chung, H.; Jang, H.; Lee, J.; Kim, D.; Jang, E. Highly Efficient and Stable InP/ZnSe/ZnS Quantum Dot Light-Emitting Diodes. *Nature* **2019**, *575* (7784), 634–638. <https://doi.org/10.1038/s41586-019-1771-5>.
- (31) Kwak, D.-H.; Ramasamy, P.; Lee, Y.-S.; Jeong, M.-H.; Lee, J.-S. High-Performance Hybrid InP QDs/Black Phosphorus Photodetector. *ACS Appl. Mater. Interfaces* **2019**, *11* (32), 29041–29046. <https://doi.org/10.1021/acsami.9b07910>.
- (32) Liu, W.; Lee, J.-S.; Talapin, D. V. III–V Nanocrystals Capped with Molecular Metal Chalcogenide Ligands: High Electron Mobility and Ambipolar Photoresponse. *J. Am. Chem. Soc.* **2013**, *135* (4), 1349–1357. <https://doi.org/10.1021/ja308200f>.
- (33) Kim, Y.; Ham, S.; Jang, H.; Min, J. H.; Chung, H.; Lee, J.; Kim, D.; Jang, E. Bright and Uniform Green Light Emitting InP/ZnSe/ZnS Quantum Dots for Wide Color Gamut Displays. *ACS Appl. Nano Mater.* **2019**, *2* (3), 1496–1504. <https://doi.org/10.1021/acsanm.8b02063>.
- (34) Jo, J.-H.; Jo, D.-Y.; Lee, S.-H.; Yoon, S.-Y.; Lim, H.-B.; Lee, B.-J.; Do, Y. R.; Yang, H. InP-Based Quantum Dots Having an InP Core, Composition-Gradient ZnSeS Inner Shell, and ZnS Outer Shell with Sharp, Bright Emissivity, and Blue Absorptivity for Display Devices. *ACS Appl. Nano Mater.* **2020**, *3* (2), 1972–1980. <https://doi.org/10.1021/acsanm.0c00008>.
- (35) Hetsch, F.; Zhao, N.; Kershaw, S. V.; Rogach, A. L. Quantum Dot Field Effect Transistors. *Materials Today* **2013**, *16* (9), 312–325. <https://doi.org/10.1016/j.mattod.2013.08.011>.
- (36) Taylor, D. A.; Teku, J. A.; Cho, S.; Chae, W.-S.; Jeong, S.-J.; Lee, J.-S. Importance of Surface Functionalization and Purification for Narrow FWHM and Bright Green-Emitting InP Core–Multishell Quantum Dots via a Two-Step Growth Process. *Chem. Mater.* **2021**, *33* (12), 4399–4407. <https://doi.org/10.1021/acs.chemmater.1c00348>.

- (37) Nemoto, K.; Watanabe, J.; Sun, H.-T.; Shirahata, N. Coherent InP/ZnS Core@shell Quantum Dots with Narrow-Band Green Emissions. *Nanoscale* **2022**, *14* (27), 9900–9909. <https://doi.org/10.1039/D2NR02071H>.
- (38) Calvin, J. J.; Kaufman, T. M.; Sedlak, A. B.; Crook, M. F.; Alivisatos, A. P. Observation of Ordered Organic Capping Ligands on Semiconducting Quantum Dots via Powder X-Ray Diffraction. *Nat Commun* **2021**, *12* (1), 2663. <https://doi.org/10.1038/s41467-021-22947-x>.
- (39) Cho, E.; Kim, T.; Choi, S.; Jang, H.; Min, K.; Jang, E. Optical Characteristics of the Surface Defects in InP Colloidal Quantum Dots for Highly Efficient Light-Emitting Applications. *ACS Appl. Nano Mater.* **2018**, *1* (12), 7106–7114. <https://doi.org/10.1021/acsanm.8b01947>.
- (40) Seo, H.; Bang, M.; Kim, Y.; Son, C.; Jeon, H. B.; Kim, S.-W. Unprecedented Surface Stabilized InP Quantum Dots with Bidentate Ligands. *RSC Adv.* **2020**, *10* (19), 11517–11523. <https://doi.org/10.1039/C9RA10933A>.
- (41) Roy, P.; Devatha, G.; Roy, S.; Rao, A.; Pillai, P. P. Electrostatically Driven Resonance Energy Transfer in an All-Quantum Dot Based Donor–Acceptor System. *J. Phys. Chem. Lett.* **2020**, *11* (13), 5354–5360. <https://doi.org/10.1021/acs.jpcclett.0c01360>.
- (42) Li, Z.; Hu, Y.; Shen, H.; Lin, Q.; Wang, L.; Wang, H.; Zhao, W.; Li, L. S. Efficient and Long-Life Green Light-Emitting Diodes Comprising Tridentate Thiol Capped Quantum Dots: Efficient and Long-Life Green Light-Emitting Diodes... *Laser & Photonics Reviews* **2017**, *11* (1), 1600227. <https://doi.org/10.1002/lpor.201600227>.
- (43) Vasudevan, D.; Gaddam, R. R.; Trinchi, A.; Cole, I. Core–Shell Quantum Dots: Properties and Applications. *Journal of Alloys and Compounds* **2015**, *636*, 395–404. <https://doi.org/10.1016/j.jallcom.2015.02.102>.
- (44) Choi, J.; Choi, W.; Jeon, D. Y. Ligand-Exchange-Ready CuInS₂/ZnS Quantum Dots via Surface-Ligand Composition Control for Film-Type Display Devices. *ACS Appl. Nano Mater.* **2019**, *2* (9), 5504–5511. <https://doi.org/10.1021/acsanm.9b01085>.
- (45) Turo, M. J.; Macdonald, J. E. Crystal-Bound vs Surface-Bound Thiols on Nanocrystals. *ACS Nano* **2014**, *8* (10), 10205–10213. <https://doi.org/10.1021/nn5032164>.
- (46) Lin, W.; Niu, Y.; Meng, R.; Huang, L.; Cao, H.; Zhang, Z.; Qin, H.; Peng, X. Shell-Thickness Dependent Optical Properties of CdSe/CdS Core/Shell Nanocrystals Coated with Thiol Ligands. *Nano Res.* **2016**, *9* (1), 260–271. <https://doi.org/10.1007/s12274-016-1014-0>.
- (47) Bai, Z.; Ji, W.; Han, D.; Chen, L.; Chen, B.; Shen, H.; Zou, B.; Zhong, H. Hydroxyl-Terminated CuInS₂ Based Quantum Dots: Toward Efficient and Bright Light Emitting Diodes. *Chem. Mater.* **2016**, *28* (4), 1085–1091. <https://doi.org/10.1021/acs.chemmater.5b04480>.
- (48) Simon-Kutscher, J.; Gericke, A.; Hühnerfuss, H. Effect of Bivalent Ba, Cu, Ni, and Zn Cations on the Structure of Octadecanoic Acid Monolayers at the Air–Water Interface As Determined by External Infrared Reflection–Absorption Spectroscopy. *Langmuir* **1996**, *12* (4), 1027–1034.

- <https://doi.org/10.1021/la950731q>.
- (49) Watanabe, J.; Yamada, H.; Sun, H.-T.; Moronaga, T.; Ishii, Y.; Shirahata, N. Silicon Quantum Dots for Light-Emitting Diodes Extending to the NIR-II Window. *ACS Appl. Nano Mater.* **2021**, *4* (11), 11651–11660. <https://doi.org/10.1021/acsanm.1c02223>.
- (50) Yamada, H.; Saitoh, N.; Ghosh, B.; Masuda, Y.; Yoshizawa, N.; Shirahata, N. Improved Brightness and Color Tunability of Solution-Processed Silicon Quantum Dot Light-Emitting Diodes. *J. Phys. Chem. C* **2020**, *124* (42), 23333–23342. <https://doi.org/10.1021/acs.jpcc.0c06672>.
- (51) Ahmadi, M.; Wu, T.; Hu, B. A Review on Organic–Inorganic Halide Perovskite Photodetectors: Device Engineering and Fundamental Physics. *Adv. Mater.* **2017**, *29* (41), 1605242. <https://doi.org/10.1002/adma.201605242>.
- (52) Ra, H.-S.; Kwak, D.-H.; Lee, J.-S. A Hybrid MoS₂ Nanosheet–CdSe Nanocrystal Phototransistor with a Fast Photoresponse. *Nanoscale* **2016**, *8* (39), 17223–17230. <https://doi.org/10.1039/C6NR05393A>.
- (53) Kolli, C. S. R.; Selamneni, V.; A. Muñoz Martínez, B.; Fest Carreno, A.; Emanuel Sanchez, D.; Terrones, M.; Strupiechonski, E.; De Luna Bugallo, A.; Sahatiya, P. Broadband, Ultra-High-Responsive Monolayer MoS₂/SnS₂ Quantum-Dot-Based Mixed-Dimensional Photodetector. *ACS Appl. Mater. Interfaces* **2022**, *14* (13), 15415–15425. <https://doi.org/10.1021/acsmi.2c02624>.
- (54) Zhou, Y. H.; Zhang, Z. B.; Xu, P.; Zhang, H.; Wang, B. UV-Visible Photodetector Based on I-Type Heterostructure of ZnO-QDs/Monolayer MoS₂. *Nanoscale Res Lett* **2019**, *14* (1), 364. <https://doi.org/10.1186/s11671-019-3183-8>.
- (55) Konstantatos, G.; Levina, L.; Tang, J.; Sargent, E. H. Sensitive Solution-Processed Bi₂S₃ Nanocrystalline Photodetectors. *Nano Lett.* **2008**, *8* (11), 4002–4006. <https://doi.org/10.1021/nl802600z>.

Chapter 5: Summary and Future Prospects

Summary

The main purpose of this paper is to synthesize coherent core/shell InP/ZnSQD as a new approach of core-shell structure, and to clarify the relation between its optical properties and structure. In addition, the possibility of the coherent core shell structure InP/ZnS was investigated by the application to the device.

In chapter 2, InP core with excellent size distribution was synthesized. It was suggested that it had the narrowest size distribution among InP cores reported until now. The existence of the coherent structure was investigated by investigating the thickness dependence of the shell using this QD. InP/ZnS with a thin shell has a coherent structure in which the core atoms are compressed and the shell is stretched so that the lattice constants of each are the same. Such an elegant core shell structure is reported for the first time in InP/ZnSQD. Furthermore, a PL half-width at half maximum (PL-FWHM 35 nm) PLQY of 70% was achieved, which was the best optical property ever reported for InP/ZnS systems. This excellent optical property appeared in InP/ZnS with coherent structure, and PL-FWHM and PLQY also decreased when the ZnS shell was thickly grown. TEM observation confirmed that the thick-shelled InP/ZnS has heterogeneous shell growth such as the S-K growth mode.

In Chapter 3, optical properties and phonon interactions are investigated. Low-temperature PL measurements were carried out to investigate whether the PL-FWHM expansion of a thick shell is influenced more by the shape of the QD or the strength of the electron-phonon coupling. InP/ZnSQD with thickly grown shell reduces the electron-phonon coupling strength compared with thin QD. On the other hand, it is revealed that the PL-FWHM is enlarged by the growth of inhomogeneous shells due to large lattice mismatch.

In Chapter 4, the device using coherent core/shell structure InP/ZnSQD was produced. In this study, InP/ZnSDQ photodiodes were reported for the first time. By using this coherent core/shell QD as an optical absorption layer, it was found that a good vertical photodiode exhibiting a fast response of a single digit millisecond scale (4/9 msec) could be fabricated. In addition, unlike a phototransistor requiring a power source, it was confirmed that the photodiode circuit operates in the photovoltaic mode (voltage bias 0V). And, the film formation property on the substrate in which ZnO was deposited was improved by exchanging the long chain organic ligand which modified on the InP/ZnS surface with the short chain organic ligand. Since the steric hindrance effect by the ligand is weakened and the density of QD is increased, the responsiveness to light is improved. Therefore, it responded to very weak light of 0.29 mW/cm².

Future Prospects

In this dissertation, a coherent core/shell InP/ZnSQD with excellent optical properties of PLQY 70% and PL-HWHM 35 nm was obtained. The effectiveness of coherent core/shell structure in InP and ZnS with large lattice mismatch was obtained. This indicates the possibility of core-shelling even in other core-shell combinations with large lattice mismatches, making the material selection of the core and shell more flexible. As a future approach, it was clarified that it is important to control the shell shape in order to obtain better optical properties.

The coherent core/shell is capable of high-speed photodetection, and the possibility as a Cd-free photodetector in the next generation was found. In the future, optimization of the device structure (for example, optimization of the thickness of the ZnO layer) will further improve the photodetection capability.

謝辞

本研究は、北海道大学大学院総合化学院後期課程在籍中、連携大学院制度により国立研究開発法人物質・材料研究機構(NIMS)で得られた研究内容をまとめたものです。本博士論文研究の遂行にあたり、北海道大学総合化学院客員教授 兼 NIMS 国際ナノアーキテクトニクス研究拠点 ナノ粒子グループ、グループリーダーの白幡直人教授には研究の方向性、得られたデータの議論、論文投稿、常に研究に集中できる環境に至るまで、多大なるご指導ご鞭撻を賜りました。ここに心より深く感謝を申し上げます。

ご多忙の中、本論文をまとめるにあたり有益なご助言、ご指導賜りました北海道大学総合化学院・村越 敬教授、上野 貢生教授、葉 金花客員教授、打越 哲郎客員教授、島田 敏宏教授に厚く感謝申し上げます。また本研究に関する数々のご教授賜りました物質・材料研究機構・スン ホンタオ教授、鈴木達教授、東京都市大学理工学部・宗像文男教授に深く感謝いたします。

ナノ粒子グループに所属すべての皆様から、研究を進めるにあたっての様々な支援を頂きました。同後期課程在籍・山田 博之氏と研究業務員・高澤 史枝氏には実験的な助言と支援を頂きました。事務業務員・曾我 まさみ氏には NIMS での学生生活を支えていただきました。同後期課程在籍・CHATTERJEE Subhashri 氏、HUANG Xiaoyu 氏、中央大学・渡邊純平氏には実験の手法に関して助言をいただきました。ここに深く感謝いたします。また NIMS 内の石井健斗博士、İrem Nur Gamze ÖZBİLGİN 博士からのご協力賜りましたこと厚く御礼申し上げます。

最後に、本学で学ぶ機会を与えて頂くとともに、常に暖かく励まし応援して下さいました家族にこの場を借りて深謝の意を表します。

2022 年 12 月

根本 一宏